

Charles University

Faculty of Mathematics and Physics

DOCTORAL THESIS

2019

Daniil Nikitin



**FACULTY
OF MATHEMATICS
AND PHYSICS**
Charles University

DOCTORAL THESIS

Daniil Nikitin

**Structuring of plasma polymers: new methods for
fabrication of nano-architected thin films**

Department of Macromolecular Physics

Supervisor of the doctoral thesis: Doc. Ing. Andrey Shukurov, PhD

Study programme: Physics

Specialization: F4 – Biophysics, Chemical and Macromolecular Physics

Prague 2019

I declare that I carried out this doctoral thesis independently, and only with the cited sources, literature and other professional sources.

I understand that my work relates to the rights and obligations under the Act No. 121/2000 Coll., the Copyright Act, as amended, in particular the fact that the Charles University has the right to conclude a license agreement on the use of this work as a school work pursuant to Section 60 paragraph 1 of the Copyright Act.

In, data.....

signature

This thesis summarizes the results of my scientific work during the 4 years of PhD studying. It could not be possible without invaluable help and friendly support of my wonderful colleagues, friends and family members. In this part, I would like to thank all who in one way or another contributed in the preparation of the thesis.

First, I would like to express my deep and sincere gratitude to my supervisor Andrey Choukourov for the opportunity to study and to do research in the Department of Macromolecular Physics in Charles University in Prague. I extremely thank him for sensitive leadership, interesting scientific ideas and helpful practical advices. Moreover, I grateful to him for his friendship and for memorable football matches.

I thank Prof. Hynek Biederman, the head of the Group of Plasma Polymers, and for his invaluable experience and inexhaustible enthusiasm. I am very grateful to my elder colleagues Doc. Ondřej Kylián, Dr. Jan Hanuš, Dr. Jaroslav Kousal, Dr. Pavel Solař, Dr. Anna Kuzminova and Doc. Danka Slavínská for their assistance with experimental set-up construction and with measurements, and for the great atmosphere in our group. I thank our former PhD students Artem Shelemin, Iurii Melnichuk and Ivan Gordeev for their help in acquirement of the experimental methods and characterization techniques. I am grateful to the Head of our Department Doc. Lenka Hanyková for the assistance with NMR measurements and Doc. Ivan Krakovský for the assistance with GPC measurements. Moreover, I am very thankful to my colleagues and good friends Mikhailo Vaidulych, Pavel Pleskunov, Renata Tafiichuk, Suren Ali-Ogly, Zdeněk Krtouš, Radka Štefaníková a Hana Libenská for their kindness, responsiveness and inexhaustible positive.

I would like to thank Dr. Matthias Schwartzkopf and Prof. Stephan V Roth from DESY, Hamburg for the invaluable help with SAXS measurements.

I appreciate Prof. Franz Faupel, Dr. Oleksandr Polonskyi and Jonas Drewes for the organization of my research traineeship in their lab in Christian Albrechts University at Kiel.

I am very grateful to Prof. Andreas Schonhals and Dr. Sherif Madkour from Bundesanstalt für Materialforschung und – prüfung in Berlin for the organization of AC-chip calorimetry measurements.

I am thankful to Prof. Svetlana Ermolaeva, Dr. Elena Sysolyatina and Alexandra Lavrikova from Gamaleya National Research Center of Epidemiology and Microbiology in Moscow for the antibacterial tests.

Finally, I would like to thank my dear Mom, Granny Galya and Uncle Valerii Alexandrovich for wise advices, love and faith in me. Special thank I address to my future wife Svetlana for your support, care, patience and love, which knows no boundaries, no distance.

Název práce: Strukturování plazmových polymerů: nové metody přípravy tenkých vrstev s nano-architekturou

Autor: Daniil Nikitin

Katedra/Ústav: Katedra Makromolekulární Fyziky/Univerzita Karlova

Vedoucí doktorské práce: Doc. Ing. Andrey Shukurov, PhD

Abstrakt: Disertační práce je zaměřena na studium nanostruktur na bázi plazmových polymerů. Hlavní pozornost je věnována přípravě antibakteriálních nanokompozitních vrstev kov/polymer za použití plynového agregačního zdroje nanočástic a plazmatem asistované depozice z plynné fáze. Do biokompatibilní matrice plazmového polymeru poly(ethylen oxidu) (ppPEO) byly začleněny měděné nanočástice. Byla prokázána účinnost těchto nanokompozitů proti multi-rezistentním bakteriím. Pomocí měření dynamické teploty skelného přechodu bylo zjištěno, že se v přítomnosti nanočástic významně změnila segmentová dynamika plazmového polymeru. To zásadně ovlivnilo bio-rezistentní vlastnosti poly(ethylen oxidu).

Samostatná kapitola je věnována studiu vzniku, růstu a transportu nanočástic uvnitř zdroje. Měděné a stříbrné nanočástice byly detekovány *in situ* v plynné fázi buďto pomocí maloúhlového rozptylu rentgenového záření, nebo pomocí UV-Vis spektroskopie. Vůbec poprvé bylo zjištěno zachytávání kovových nanočástic v plazmatu. Navíc byla potvrzena částečná re-depozice nanočástic na terč a stěny zdroje.

Poslední kapitola práce popisuje použitelnost našeho přístupu pro modifikaci polymerních nanostruktur (například nano-ostrůvků) pomocí kovových nanočástic.

Klíčová slova: nanostruktura, plynový agregační zdroj nanočástic, plazmový polymer, nanokompozit, segmentová dynamika.

Title: Structuring of plasma polymers: new methods for fabrication of nano-architected thin films

Author: Daniil Nikitin

Department / Institute: Department of Macromolecular Physics/Charles University

Supervisor of the doctoral thesis: Doc. Ing. Andrey Shukurov, PhD, Department of Macromolecular Physics/Charles University

Abstract: The PhD thesis aims at the investigation of nanostructures based on plasma polymers. The main attention is paid to the combination of a gas aggregation cluster source with plasma-assisted vapor phase deposition for the fabrication of metal-polymer nanocomposites with bactericidal potential. Copper nanoparticles were incorporated into a biocompatible matrix of plasma polymerized poly(ethylene oxide) (ppPEO). The efficiency of such nanocomposite against multi-drug resistant bacteria was demonstrated. It was found that the segmental dynamics of the plasma polymer significantly changed in the presence of nanoparticles as revealed by the measurements of the dynamic glass transition temperature. The nanoscale confinement crucially influences the non-fouling properties of poly(ethylene oxide).

A separate chapter is dedicated to the examination of the nanoparticle formation, growth and transport inside the source. Copper and silver nanoparticles were detected *in situ* in the gas phase by small angle X-ray scattering and UV-Vis spectroscopy. The effect of trapping of metal nanoparticles in the plasma was discovered. Moreover, a partial loss of nanoparticles on the target and on the chamber walls was confirmed.

The last chapter of the thesis describes the applicability of our approach for the decoration of polymer nanostructures (e.g. nanoislands) by metal nanoparticles.

Keywords: nanostructure, gas aggregation cluster source, plasma polymer, nanocomposite, segmental dynamics.

Contents

1. INTRODUCTION	1
1.1. Plasma polymerization process: state-of-art	1
1.2. Nanostructuring of plasma polymers	7
1.3. Gas aggregation cluster source for the deposition of antibacterial nanocomposite films	10
AIMS OF THE DOCTORAL THESIS	12
2. EXPERIMENTAL	13
2.1. Plasma-based equipment for the preparation of samples	13
2.2. <i>In situ</i> nanoparticle diagnostic techniques	16
2.2.1. SAXS measurements	16
2.2.2. Deposition of NPs inside the GAS	17
2.2.3. UV-Vis spectroscopy characterization of NPs in the gas phase	18
2.3. Methods for the sample characterization	20
2.3.1. Spectroscopic techniques	20
2.3.2. Microscopy techniques	24
2.3.3. Water contact angle measurements	25
2.4. Biological tests	25
2.4.1. Protein adsorption	25
2.4.2. Antibacterial tests	26
3. RESULTS AND DISCUSSION	28
3.1. Ag and Cu nanoparticle deposition and characterization	28
3.1.1. <i>Ex-situ</i> characterization of Ag and Cu NPs	28
3.1.2. In-flight diagnostics of the NP growth performed by SAXS	31
3.1.3. <i>In-situ</i> detection of NPs by UV-Vis spectroscopy	35
3.1.4. SEM imaging of Ag NPs collected inside the aggregation chamber	39
3.2. Preparation of composite thin films for bio-applications	49
3.2.1. Deposition of Cu NPs/PEO nanocomposites	49
3.2.2. The segmental dynamics of ppPEO in nanocomposites	57
3.3.3. Biological activity of metal – polymer nanocomposites	63
3.3. Decoration of polymeric nanostructures by Cu NPs	69
3.3.1. The deposition of polystyrene nanoislands	69
3.3.2. The decoration of ppPEO film and PS nanoislands by Cu NPs	72

CONCLUSIONS	76
BIBLIOGRAPHY	77
LIST OF TABLES	90
LIST OF ABBREVIATIONS	91
LIST OF PUBLICATIONS.....	92
AUTHOR'S CONTRIBUTION	97

1. INTRODUCTION

Nowadays, polymers and polymer-based composites play an important role in human life. It is no exaggeration to say that polymers are everywhere. People use polymers in the construction, engineering, electronics, medicine, textile industry etc. It should be clarified that most often it is talked about a large amount of polymeric material (in other words, bulk polymer). Nevertheless, some applications require the miniaturization, such as microelectronic devices, biomedicine or functional coatings. In these cases the nanostructuring of polymers is necessary. Starting in the 2nd half of the 20th century, a variety of polymeric nanostructures has been fabricated, such as thin films, nanoislands, nanofibers, nanowires or micro- and nanoparticles (NPs).[1] Most of these materials were successfully synthesised by the traditional wet chemical methods including spin-coating, inkjet or roll-to-roll printing, electrospinning, laser ablation or Langmuir-Blodgett technique.[2, 3] The traditional techniques are already widely used for the industrial production of polymer nanomaterials now. However, it should be noted that they are the resource intensive and environmentally unfriendly. Thereby, the development of new methods for the fabrication of polymeric nanostructures is a hot topic for the material scientists. In the last decades, the vacuum-based techniques began to gain popularity. The processes occurring under the vacuum conditions satisfies the ecological requirements; moreover, they are relatively easily controlled and environmentally friendly. A special attention is paid to the plasma assisted techniques, which enable to produce a unique class of the materials named plasma polymers.

1.1. Plasma polymerization process: state-of-art

In accordance with the International Union of Pure and Applied Chemistry, a polymer is “A molecule of high relative molecular mass, the structure of which essentially comprises the multiple repetitions of units derived, actually or conceptually, from molecules of low relative molecular mass.” In contrast, plasma polymers represent highly branched and highly cross-linked networks, which form as a result of the fragmentation of gaseous precursor under the low temperature plasma action with subsequent recombination. The hypothetic structure of typical plasma polymer is shown in Figure 1. The first mentioning of plasma polymers dates back to the 1870s when the films of polymerized oil were found on the walls of the discharge tubes.[4]

For a long time, they were considered as an undesirable product. Only in the first half of the 20th century, plasma polymer films were firstly characterized. In the 1960s, the first application of plasma polymerized styrene as a barrier layer was published by Goodman.[5] In the next decades, the interest to plasma polymers in the scientific community rapidly increased. It was found that the increase of pressure in the reactor initiates the formation of micro- and nanosized particles in the plasma zone. This phenomenon was called dusty plasma.

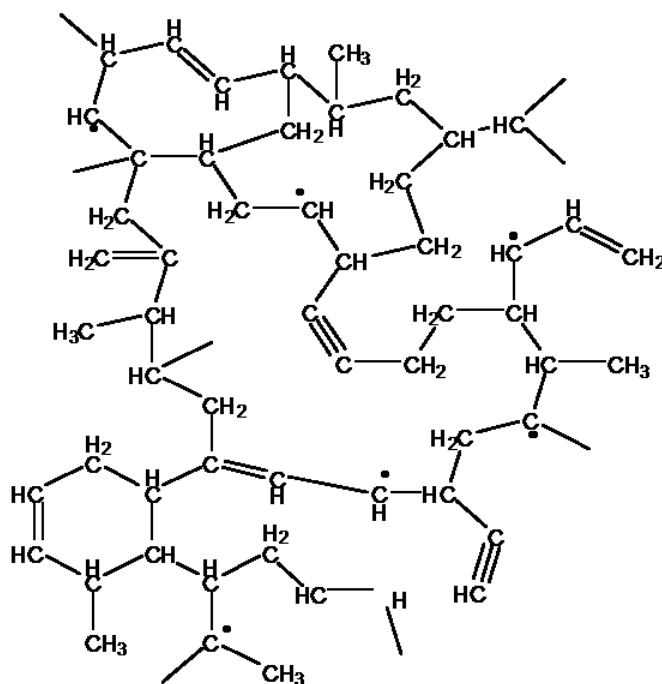
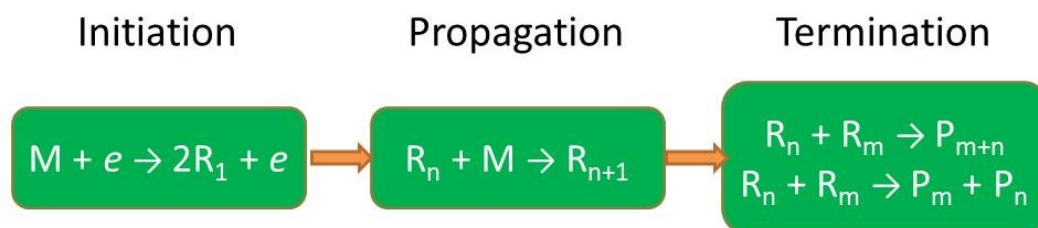


Figure 1. Hypothetical structure of plasma polymer.

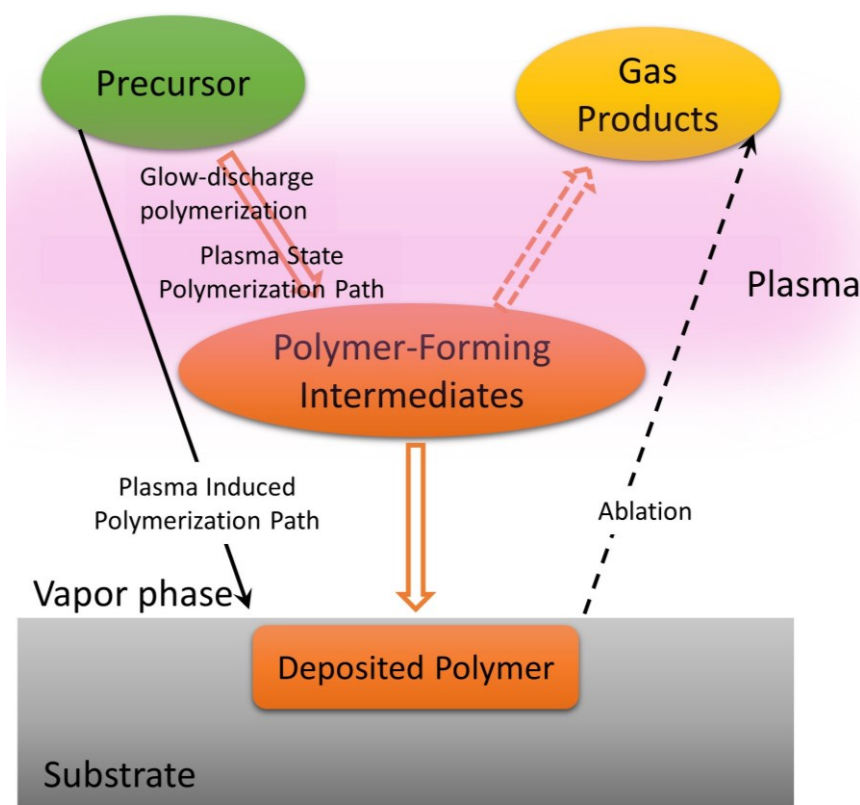
Several mechanisms of polymerization were proposed to describe the process of interaction between the plasma and monomer molecules. The simplest concept was described by Lam and was called free-radical plasma polymerization.[6, 7] It is known that plasma is a quasineutral medium containing neutral species, positive and negative ions, and free electrons. The non-equilibrium electrons interact with precursor molecules inelastically which results in the formation of free radicals (*activation* stage). Radicals then attach to intact precursor molecules by opening of unsaturated carbon bonds and thus the molar mass increases (*propagation* stage). Finally, the *termination* of polymer chains takes place if radicals recombine. For clarity, the free-radical mechanism is drawn in Scheme 1. Lam assumed that the propagation and termination are going simultaneously in a gas phase and on the adjacent surfaces.

Afterwards, the more real scenario was proposed by Pall when the radicals form in a gas phase and subsequently interact with monomer units adsorbed on the substrate.



Scheme 1. Free-radical mechanism of plasma polymerization elaborated by Lam.[7]

Plasma polymerization theory was further developed by Yasuda and Hsu.[8, 9] They introduced the processes of polymer ablation, which were initiated by the bombardment of the growing film by positive ions from plasma (competitive ablation and polymerization mechanism, Scheme 2). The gaseous products of ablation can be reactivated and can participate the polymerization again or can be removed from the reaction volume by pumping. In the case if the rate of ablation exceeds the rate of free-radical polymerization, the polymer film does not form on the substrate.



Scheme 2. Competitive ablation and polymerization mechanism proposed by Yasuda and Hsu.

Moreover, Yasuda introduced more complex mechanism of plasma polymerization (see Figure 2). He assumed the existence of two cycles responsible for plasma polymer growth. The first was similar to the standard free-radical mechanism. The second involved so-called bifunctional species (i.e. the monomer species containing together cationic and radical propagating centers or bi-radicals). Bifunctional species permitted the simultaneous growth of polymeric chain in multiple directions by the multiple pathways. This mechanism was named rapid step-growth polymerization.

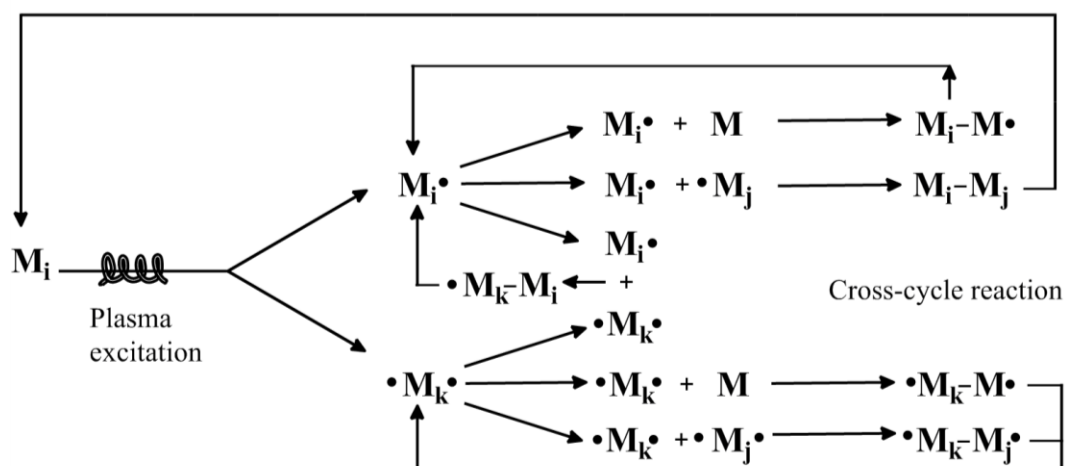


Figure 2. The rapid step-growth polymerization mechanism introduced by Yasuda (adapted from [10]).

Later, d'Agostino developed an activated growth model of plasma polymerization of fluorocarbons. It was described in detail in [11]. According to this model, the processes of electron and ion bombardment of the surface are very important in the plasma polymer growth. They can be responsible for such processes as precursor desorption from the substrate, film sputter erosion and degree of cross-linking. Thereby, the control over the deposition parameters (working gas pressure, discharge power) which influence the energy of bombarding ions is necessary for the control over the final film properties. For example, if it is required to retain the structure close to the initial monomer, the ion energy should be reduced.

Different deposition techniques utilizing low pressure plasma were developed for polymerization. Several variations of the reactors are presented in Figure 3. In Figure 3a, a system with internal parallel-plate electrodes is shown. Two metal electrodes are powered by the AC or RF voltage. The discharge is ignited in the atmosphere of a working gas mixture (typically, inert gas with monomer vapor) and plasma polymerization occurs. The discharge pressure is varied from 1 to 100 Pa. Another approach for deposition of plasma polymer films involves sputtering of polymer targets (Figure 3b). An RF powered planar magnetron is employed as an excitation electrode. A substrate holder can be electrically isolated, grounded or biased. This approach was successfully applied for sputtering of polytetrafluoroethylene (PTFE),[12–14] polypropylene,[15, 16] polyethylene,[17–19] polyimide,[20, 21] amorphous hydrocarbon,[22] polyaniline [23] and nylon.[24] Other very popular deposition reactors include glass tubes with outer-ring capacitively coupled excitation electrodes or an excitation coil (see Figure 3c and Figure 3d). Such systems were widely used for a long time and even were chosen for a round-robin experiment on the deposition of polyacrylic acid thin films.[25] For more energetic excitation, a microwave-powered (2.45 GHz) arrangement is needed. The scheme of the microwave-powered reactor is shown in Figure 3e. Finally, a relatively new method for the deposition of plasma polymer films is presented in Figure 3f. Plasma assisted vacuum evaporation technique represents thermal decomposition of bulk polymer precursor with the subsequent transition of oligomers into the vapor phase. The oligomer flux passes through the plasma and radicals are generated. Afterwards, radicals recombine on the substrate surface forming the plasma polymer film. Thin films of plasma polymerized polyimide and poly(ethylene oxide) (PEO) have been deposited by this method.[26–28]

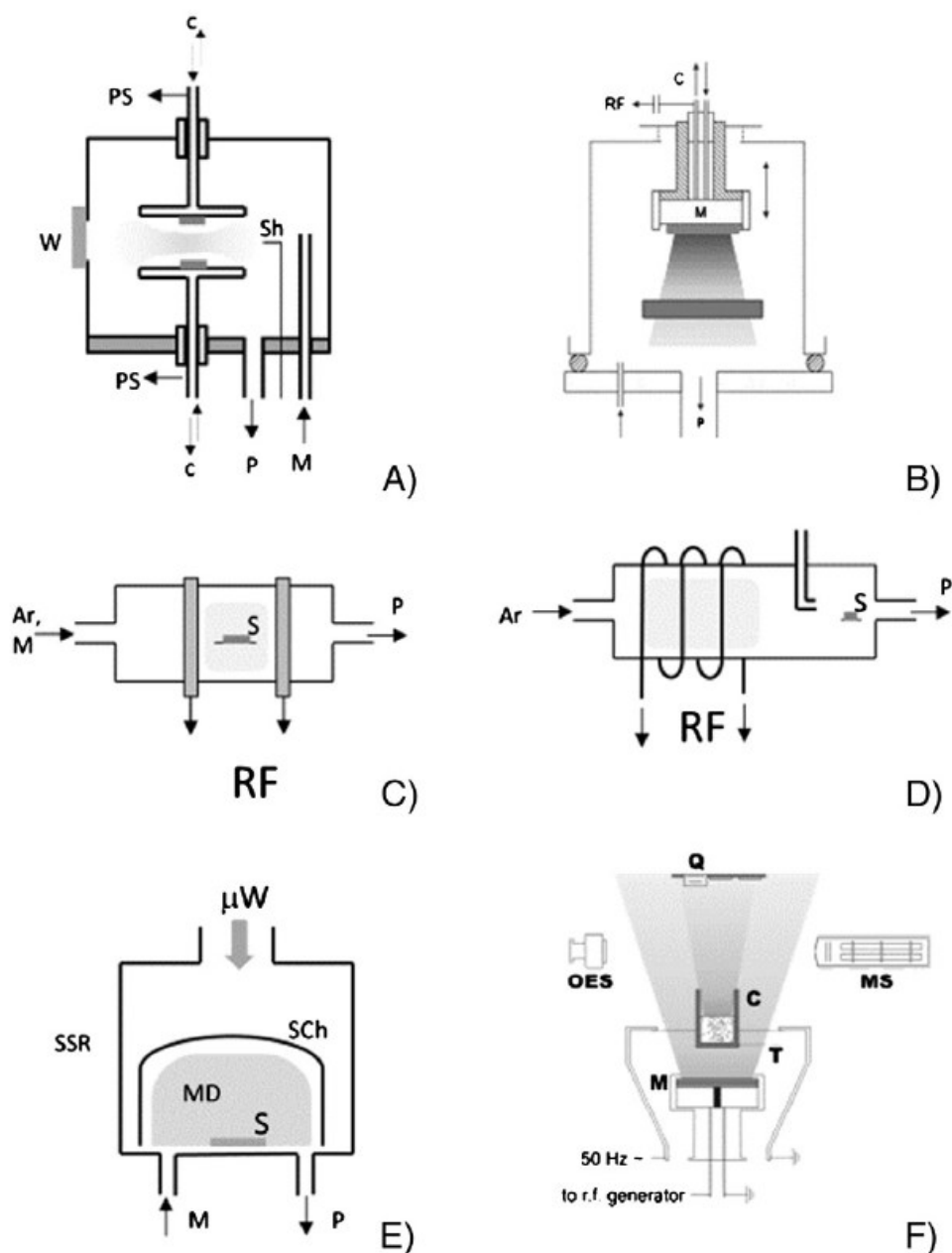


Figure 3. Several deposition systems: a) parallel-plate electrode reactor; b) magnetron sputtering system; c), d) tubular reactors with outer-ring capacitively coupled excitation electrodes or an excitation coil, respectively; e) microwave reactor; f) plasma assisted vapor phase deposition system. Abbreviations: PS – power supply, C – cooling, W – window, P – pumps, M – monomer, Sh – shutter, S – substrate, μW – microwave energy, MD – microwave discharge, SSR – stainless steel resonator, SCh – silica chamber, Q – quartz crystal microbalance, MS – mass spectrometer, T - thermocouple, C –evaporator. (adapted from [25])

In accordance with the aims of the current work, PEO plasma polymer was chosen because of its unique ability to resist against the adsorption of proteins. Such ability is called non-fouling properties. It is assumed that these properties may partially originate from the presence of ether groups in polymer structure.[29] The ether groups interact with water molecules from protein solution by hydrogen bonds and orient them forming a screening layer on the water/polymer interface. This layer prevents the binding of proteins with PEO. On the other hand, a steric repulsive interaction of the macromolecules with proteins may also play a role. The polymer chains in PEO act as macromolecular springs due to the segmental mobility and repulse the protein molecules. It is worth noting that the segmental dynamics may significantly differ in thin films adhering to rigid substrate. Recent studies revealed that a distinctly different adsorbed layer forms at the substrate/polymer interface.[30] This layer is characterized by the constrained segmental dynamics. The same effect was observed for thin films of PEO plasma polymers for which a confinement of segmental mobility was detected by the measurements of the dynamic glass transition temperature T_g^{dyn} using a novel technique of the AC-chip nanocalorimetry.[31]

Improved adhesion to substrates and mechanical stability of plasma polymer thin films in comparison with the conventional ones make them very perspective for the variety of applications. Superhydrophobic and superhydrophilic surfaces, electrically resistant surfaces, materials for drug delivery and non-fouling surfaces can be developed on the base of plasma polymers. Moreover, the application potential of plasma polymers can be improved by their nanostructuring. The Chapter 1.2 describes the methods of nanofabrication, which are successfully implemented now.

1.2. Nanostructuring of plasma polymers

Possible applications of nanostructured plasma polymers strongly influence the choice of the experimental method. For example, the surfaces with tunable wettability have attracted much attention during the last decades. The hydrophilic and hydrophobic surfaces can be easily prepared by the deposition of corresponding plasma polymer films. One of the ways to prepare the polymer (including plasma polymer) surface pattern is plasma etching. Many papers about the plasma treatment of polymers using different systems and different gases were published. In [32–34], processing of plasma polymer films by Ar plasma for the production of nanocolumnar structures is described. The nano-hierarchical surfaces can be prepared also by the direct plasma

polymerization. The developed fluorocarbon coatings were created by plasma polymerization of tetrafluoroethylene or allylpentafluorobenzene and demonstrated superhydrophobicity.[35–37]

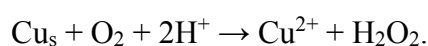
Co-deposition of hydrophilic and hydrophobic polymers allows to form the coatings with tunable wettability. The wettability is regulated by changing of the deposition parameters that influence the component ratio in the final film. Such coatings were produced by co-sputtering of hydrophilic silicon oxide with hydrophobic polytetrafluoroethylene, polyethylene, polypropylene or polyimide.[13, 19, 21] In these works, the deposition rate of the individual components was tuned by the regulation of the power applied to the magnetrons. Nanoporous coatings can be produced by plasma copolymerization of 3,3,4,4,5,5,6,6,7,7,8,8,9,9,10,10,10-heptafluoro-1-decene (HDFD) and poly(ethylene glycol) methacrylate (PEGMA) with subsequent acid treatment.[38] Plasma assisted co-deposition of two immiscible polymers can be performed by means of physical vapor deposition. In [39], the authors evaporated simultaneously hydrophilic poly(ethylene oxide) and hydrophobic polyethylene from 2 independent crucibles with subsequent activation of oligomers by glow discharge. As a result, the bi-component plasma polymer film with nanophase separation was produced. It is worth noting that the regulation of the chemical composition was able to tune the wettability as well as the cell adhesion. On the other hand, the sequential deposition of polyethylene onto the surface of pre-deposited poly(ethylene oxide) by a similar approach also leads to the formation of interesting nanostructures. As was published recently in [40], the fractal structures of different shape can be obtained.

As was mentioned in Chapter 1.1, the increase of the monomer pressure in the deposition chamber initiates the aggregation and growth of plasma polymer NPs. These NPs have been used for the preparation of nanostructured surfaces. For example, the superhydrophobic surfaces can be produced using hydrocarbon or fluorocarbon NPs as was shown in [41, 42]. Moreover, it is possible to reverse the wettability of hydrocarbon surfaces toward the superhydrophilicity by a simple plasma treatment or UV-irradiation. Plasma polymerized hexamethyldisiloxane (HMDSO) NPs were applied for the fabrication of biomimetic surfaces with multiscale roughness.[43] The size of the NPs was regulated by the RF discharge power. The surfaces with multiscale roughness provided very high surface area, which made the surface slippery with small hysteresis of water contact angle.

Glancing angle deposition is a relatively new technique for the fabrication of porous and nanostructured coatings. In this method, the flux of incident particles or polymer fragments is directed at oblique angles toward the substrate. As a result, tilted columns, chevron or zig-zag columns, helical columns and vertical columns can be formed.[44] Plasma polymers have been successfully utilized for the formation of such structures. For example, sputtering of nylon under the glancing angles permits to produce the tilted columns or vertical columns.[45] Moreover, nanocolumnar composite coatings can be formed by the simultaneous glancing angle magnetron sputtering of titanium and plasma enhanced chemical vapor deposition of hydrocarbon plasma polymer.[46] According with previous findings, the Ti/hydrocarbon nanocomposite coatings can be useful for biological applications, for example as supports for the cell growth.[47]

The combination of metals and plasma polymers in nanocomposites has attracted much attention in the past decades due to their numerous potential applications, such as electrically conductive, optically active, catalytic or antibacterial coatings.[48, 49] Metals can be included into the plasma polymer matrix in the form of NPs. In terms of biomedical applications, silver and copper are useful because of their strong antibacterial action. The antibacterial efficiency of these metals has been confirmed by many investigations.[50–58] Moreover, it has been recently revealed, that copper is able to kill the dangerous multi-drug resistant bacterial strains, such as *Methicillin-resistant staphylococcus aureus*.

The antibacterial character of Ag and Cu NPs was discussed mainly in terms of two mechanisms: the ion release and the generation of reactive oxygen species (ROS).[55, 59] The reactions corresponding to the ion release are presented below:



Metal ions may destroy membrane of bacteria, react with DNA and stimulate the death of the microorganism. Note that in the case of Cu, the ion release is accompanied by the formation of hydrogen peroxide, and it was supposed that ROS may also contribute to the antibacterial effects.

The antibacterial properties of plasma polymers loaded with Ag and Cu NPs were reported previously. The NPs produced both by wet chemical and physical methods (vacuum evaporation, magnetron sputtering) were embedded into the plasma polymerized PTFE, acetylene, *n*-heptylamine, HMDSO and ethylenediamine.[60–65]

Nevertheless, the search of new effective and environmentally friendly methods for the metallic NPs fabrication is still in progress. Synthesis of NPs by the aggregation in a cold buffer gas has become one of the most promising techniques in the last 10 years. The basics of gas aggregation source (GAS) technique and its combination with plasma polymerization is described in the next Chapter.

1.3. Gas aggregation cluster source for the deposition of antibacterial nanocomposite films

In recent years, there has been great interest in application of GASEs for the production of different kinds of NPs. The first mentioning of the bismuth cluster formation in the gas phase is dated by 1930.[66] Later in 1971, Broida and co-workers produced sodium clusters for optical applications.[67] The popularity of GAS gradually increased.[68, 69] In all these works, an initial construction based on the evaporation of material was utilized (see Figure 4, left). A crucible with material to be evaporated was installed inside a water cooled vacuum chamber which was ended by a small exit orifice. The evaporation was performed in the atmosphere of inert gas. The further progress is associated with Haberland and co-workers, who offered to use magnetron instead of the evaporation cell as a source of material in GAS.[70] The scheme of such model is drawn in Figure 4, right. The use of magnetrons has evident advantages, such as a stable deposition rate, easier control of NP characteristics and longer operation time of the target. NPs of numerous metals were successfully synthesized by the magnetron-based GAS.[71–79] Furthermore, GAS was successfully applied for the fabrication of semiconductor, insulator and even plasma polymer NPs.[80–83] The magnetron-based GAS can also be utilized for the fabrication of heterogeneous NPs. For example, the combination of two magnetrons with different targets in the same GAS leads to the formation of core-shell bi-metallic NPs.[84] It is also possible to combine magnetron sputtering with plasma polymerization inside the aggregation chamber to obtain metal – plasma polymer core-shell NPs.[85]

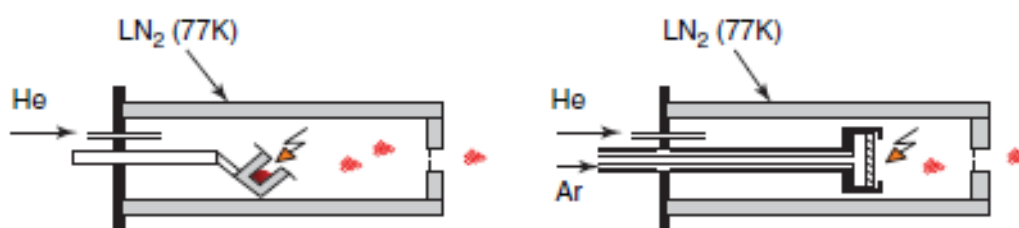


Figure 4. Schematic images of GASEs with the evaporation cell (left) and with magnetron (right) as material sources. (adapted from [86])

GASEs have become widely used for the fabrication of nanocomposite coatings. The compactness and convenience of modern cluster sources allow installing them easily onto vacuum chambers for plasma polymerization. As a result, metal NPs/plasma polymer nanocomposites can be produced both by simultaneous and sequential deposition. For example, coatings with tunable wettability might be prepared by embedding Cu and Ag NPs into matrices of sputtered nylon [87], a-CH [78] and fluorocarbon plasma polymer [88]. Antibacterial coatings were also prepared by mixing of Ag NPs with a-CH and Si-containing plasma polymers.[89, 90] Recently, superwetable textiles with antibacterial properties were developed by mixing of plasma polymer and Cu NPs.[91] The possible application of such textiles as highly-effective water/oil filters was demonstrated.

In spite of a huge number of the studies that dealt with the gas phase preparation of metal NPs and their applications, little concern has been raised with regard to the processes occurring inside the aggregation chamber. Several works dealing with modeling of the NP motion were performed, although the experimental approaches are scarce. [92, 93] Only recently, Langmuir probe and passive thermal probe were applied for the *in-situ* diagnostics of the NP formation.[94, 95] Nevertheless, the search of experimental method for the *in-situ* characterization of NPs inside the cluster source is still actual.

AIMS OF THE DOCTORAL THESIS

The thesis is focused on the development of novel nanostructured materials based on plasma polymers. In particular, the gas aggregation source of nanoparticles is to be combined with plasma polymerization to fabricate the nanocomposite materials for the potential biomedical applications. For the realization of this goal the following aims were formulated:

- *In-situ* investigation of the processes of metal NPs formation, growth and transport inside the GAS.
- The development and characterization of nanostructured films based on PEO plasma polymer with inclusion of Ag and Cu NPs. The evaluation of their antibacterial activity.
- The investigation of the influence of metal NP on the chemical composition and segmental dynamics in thin plasma polymer layers.
- The fabrication and characterization of polystyrene-like nanostructured coatings. The decoration of PEO-like and PS-like coatings by Cu NPs and characterization of their wetting behavior.

2. EXPERIMENTAL

In this work, two independent plasma-based steps were used for the fabrication of the samples. Chapter 2.1 represents the experimental equipment in detail. Silver and copper NPs were produced using GAS mounted in vertical configuration onto a stainless steel main chamber. The main chamber was equipped with a system for Plasma-Assisted Vapor Phase Deposition of plasma polymers, e.g. PEO thin films, PS nanoislands. All the experiments were performed under vacuum conditions. The vacuum system was initially pumped using rotary and diffusion pumps to the pressure of 1×10^{-4} Pa. The combination of both processes in one equipment allowed to produce the nanostructured materials based on metal NPs and plasma polymers without breaking vacuum. This part of the thesis was realized at the Department of Macromolecular Physics of the Faculty of Mathematics and Physics in Charles University.

The investigation of the NP formation and growth inside the GAS was performed at DESY synchrotrone, Hamburg, Germany. The *in situ* small angle X-ray scattering (SAXS) experiments were carried out using a special model of the GAS with diagnostics windows. The same GAS was utilized for the *in situ* UV-Vis spectroscopy measurements and depositions inside the aggregation zone to characterize the NP distribution and transport. These experiments were realized at the Chair of Multicomponent Materials of the Institute for Material Science in Christian-Albrechts University at Kiel. In both cases, the experimental equipment was pumped by scroll and turbomolecular pumps to obtain the base pressure of 3×10^{-5} Pa. The schemes of both experiments are presented in Chapter 2.2.

The diagnostic equipment used for the detailed characterization of the samples is described in Chapter 2.3.

Finally, the Chapter 2.4 is dedicated to the presentation of the experiments that took place at the Gamaleya National Research Center of Epidemiology and Microbiology, Moscow, Russia and involved the research on bactericidal effects of nanostructured samples against multidrug-resistant pathogens. The in-house tests of protein adsorption are also presented here.

2.1. Plasma-based equipment for the preparation of samples

Figure 5 shows the scheme of the experimental equipment utilized for the preparation of samples. The GAS was used for the production of Cu and Ag NPs. It consisted of a

cylindrical chamber of 10 cm in diameter. The walls of the chamber were cooled by water. A planar magnetron with diameter of 81 mm was used for the direct current sputtering of Cu or Ag targets (3 mm thick, 99.99 % purity). The magnetron was connected to a power supply (DC01 BP, Kurt J. Lesker). The chamber was ended by a cone with an exit orifice. The diameter of the orifice was 2 mm. The distance between the target surface and the aperture (a so-called aggregation length) was set at 8.5 cm. The pressure inside the source was controlled using pressure gauge with range 1×10^{-2} – 133 Pa (Pfeiffer Vacuum). Sputtering of metals was performed in the atmosphere of Ar (Linde, purity 99.996%) supplied to the GAS through a nozzle behind the magnetron. The Ar flow was regulated using a flow controller MKS MF-1. The flow rate was optimized for Cu NPs at 5 sccm that corresponded to the pressure of 75 Pa in the source. The discharge current was 130 mA. In the case of Ag NPs, the Ar flow rate was 8.5 sccm corresponding to the pressure of 100 Pa in the GAS whereas plasma was ignited at the current of 150 mA.

The GAS was connected to a main deposition chamber. The equipment for Plasma Assisted Vapor Phase Deposition consisted of a copper crucible that was filled with polymer granules (PEO, $M_n = 1500$ g/mol, Sigma-Aldrich; PS, $M_n = 192000$ g/mol, Sigma-Aldrich). The crucible was mounted onto molybdenum wires serving as electric heaters. The temperature of the crucible was increased up to 300 °C to begin the evaporation of polymeric melt. A planar electrode with diameter of 81 mm was situated under the crucible and used for the generation of Ar plasma. Ar was supplied through the GAS to achieve the working pressure of 1 Pa in the main chamber. The planar electrode was powered by an RF power supply (Dressler Ceasar 13.56 MHz) using a matching unit. The discharge power was kept constant at 5 W during all the depositions.

Substrates (Si wafers 1×1 cm, laboratory and quartz glasses with diameter of 1 cm) were glued by carbon tape onto a manually rotated sample holder, which was located in the main chamber at the distance of 10 cm above the crucible and 12 cm below the GAS orifice. The deposition rate of the metallic NPs and plasma polymers was controlled by quartz crystal microbalance (QCM) mounted in plane with the substrates.

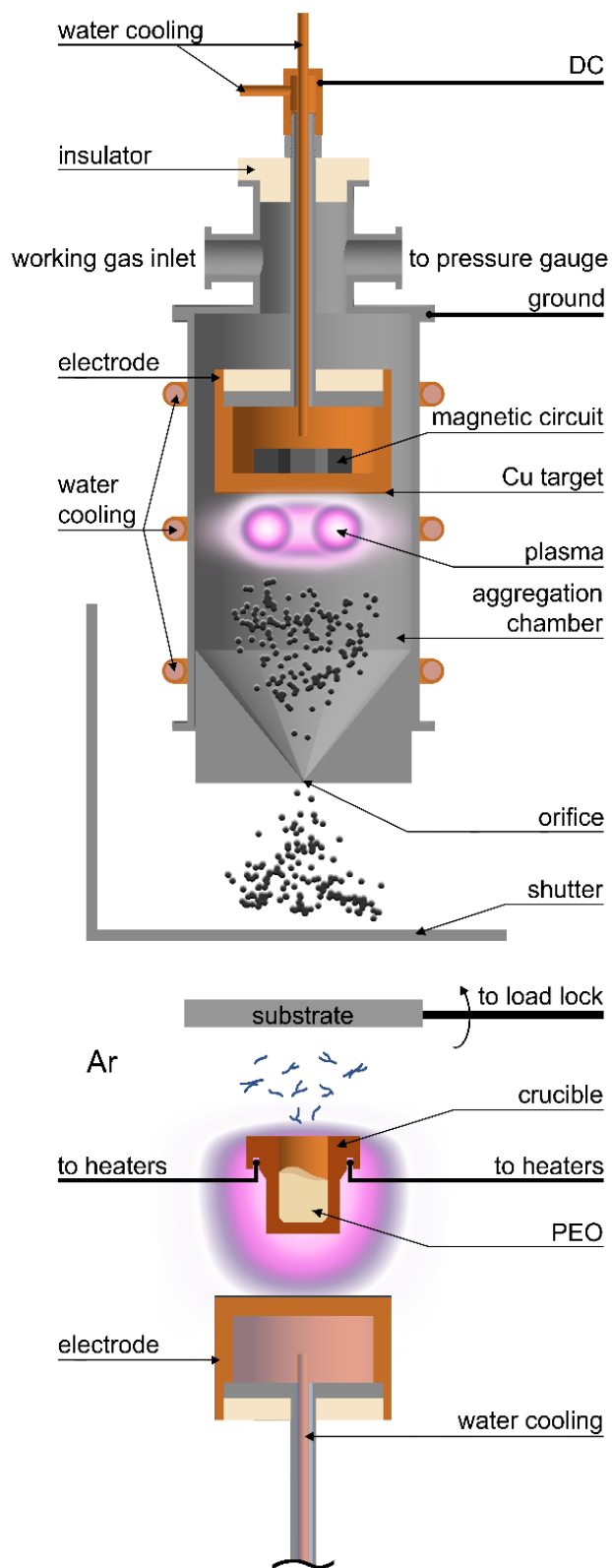


Figure 5. The scheme of the deposition equipment.

2.2. *In situ* nanoparticle diagnostic techniques

2.2.1. SAXS measurements

A special model of the GAS was constructed for the *in situ* SAXS investigation of the formation and growth of metallic NP inside the aggregation zone. It is presented in Figure 6. For these experiments, the cylindrical body of the source was equipped with kapton windows of 40 mm in diameter located opposite to each other. The full system was mounted at the P03 beamline of PETRA III, DESY, Hamburg, Germany. An elliptically microfocused X-ray beam ($22.0 \times 32.0 \pm 0.5 \mu\text{m}$, $V \times H$ axes) was directed through the windows in the GAS toward a detector (Pilatus 1M, Dectris Ltd.; pixel size $172 \mu\text{m}$). The detector was located at the distance of $5696 \pm 0.5 \text{ mm}$ from the GAS axis. The energy of photons was 13.01 keV. Such equipment made it possible to perform the measurements from 0 to 40 mm across the x axis and radially at the distance from 0 to 12 mm from the magnetron axis. Cu NPs were fabricated at pressure 86 Pa and flow 25 sccm. The discharge was ignited using current 500 mA and voltage 320 V. Ag NPs were produced at pressure 125 Pa and flow 18 sccm. The magnetron was operated at current 600 mA and voltage 300 V.

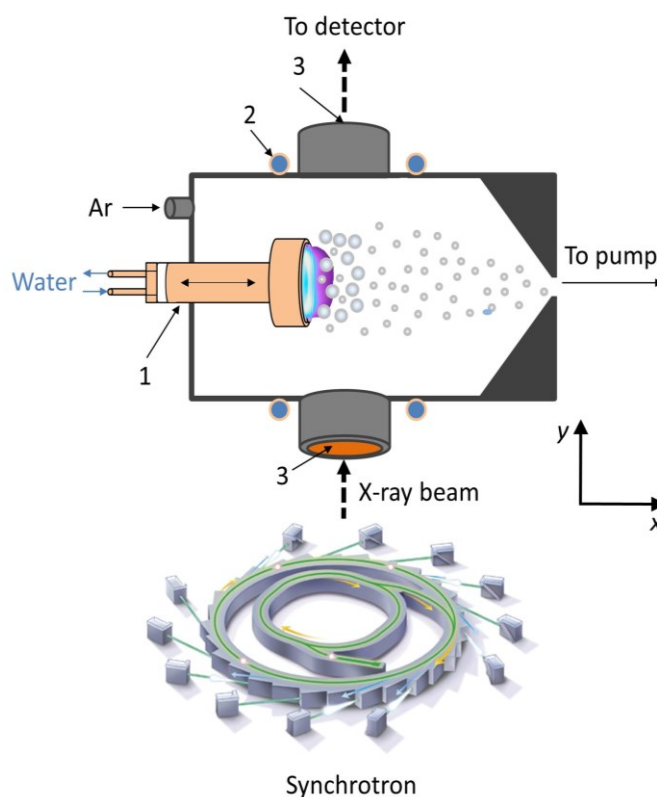


Figure 6. Schematic image of the equipment applied for SAXS measurements in DESY: 1 – adjustable magnetron, 2 – water cooling, 3 – KaptonTM windows.

The scattering curves were measured at different positions inside the aggregation zone. The software DPDAK was utilized for post-processing of the raw data.[96] Figure 7 demonstrates the examples of the scattering curves. The scattering patterns are presented as the dependencies of average integrated scattered intensity I on scattering wave vector q . The measurements were done inside the aggregation zone at different points on the magnetron axis and at different radial distances with the x position fixed at 5 mm.

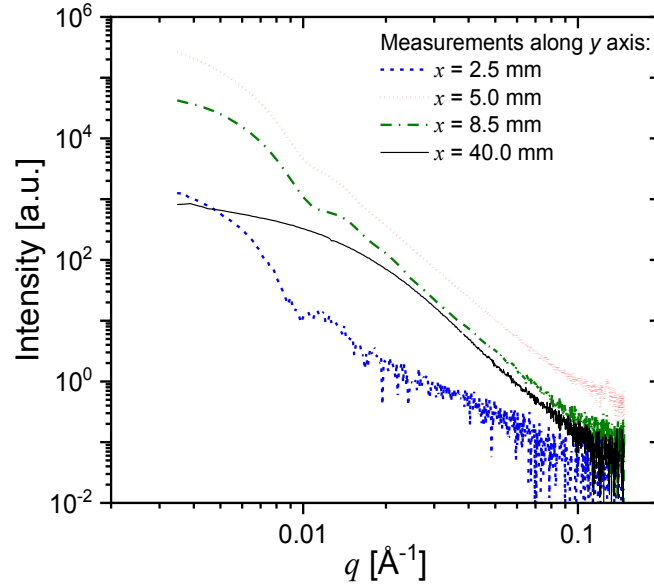


Figure 7. SAXS scattering curves measured at different positions on the GAS axis (the background was previously subtracted).

For the fitting of the experimentally measured scattering curves, the SASView software package was used with a full sphere model and lognormal size distribution.[97] This approach allowed to determine the average NP size and the relative volume fraction (i.e. the part of the volume occupied by all the NPs to the sampled volume defined by the X-ray beam size).

2.2.2. Deposition of NPs inside the GAS

A special construction of the sample holder was developed to characterize the morphology and the size of Ag NPs formed and deposited inside the aggregation zone. The scheme of the experiment is presented in Figure 8. The sample holder consisted of a stainless steel base with perpendicularly mounted stainless steel wires. The wires were located at different distances from each other. Si substrates with the size of 1.0×0.5 cm were fixed on the wires. Such design allowed locating the substrates close to

the GAS axis and to collect the NPs travelling through the aggregation zone. An additional substrate was placed on another holder behind the orifice at the distance of 20 cm. The deposition time was 10 s. The morphology of Ag NPs was determined using scanning electron microscopy (SEM, Supra55VP-Carl Zeiss). The NP size was determined using the Solarius Particles software developed at our department. For each sample, at least 150 NPs were processed to obtain the size distribution and to calculate the mean diameter.

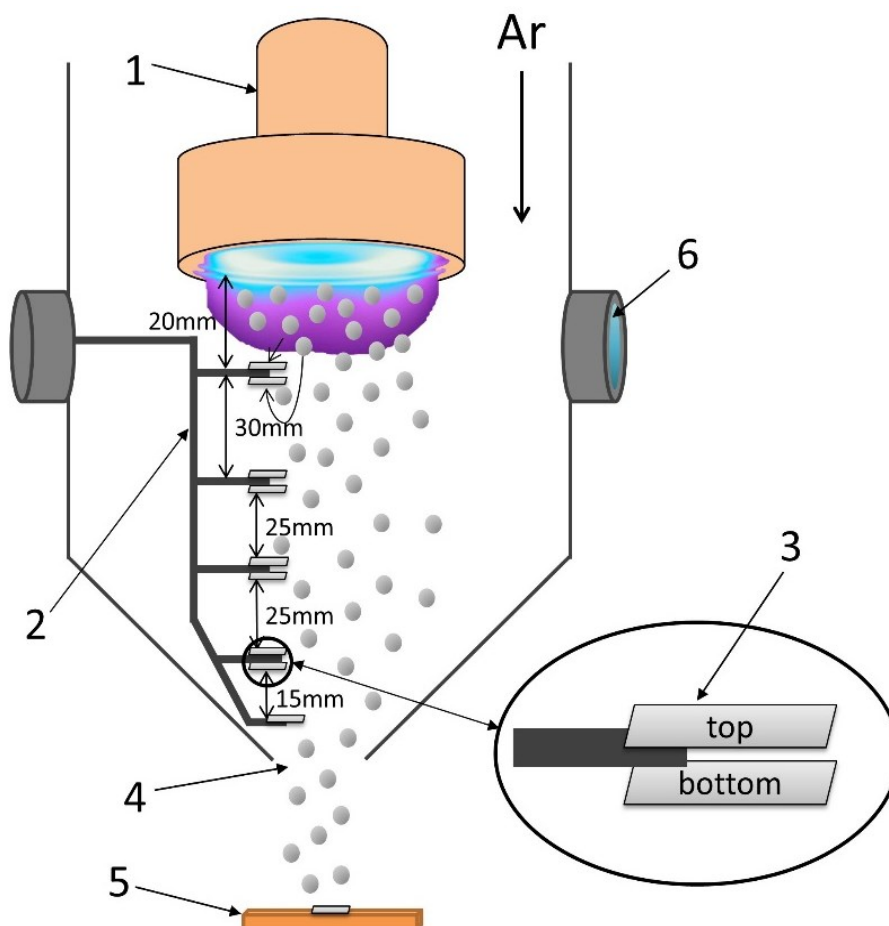


Figure 8. The equipment applied for the deposition of Ag NPs inside the aggregation zone: 1 – magnetron with Ag target; 2 – sample holder; 3 – Si substrates; 4 – orifice; 5 – sample holder behind the orifice; 6 – glass window.

2.2.3. UV-Vis spectroscopy characterization of NPs in the gas phase

UV-vis spectroscopy is a promising technique for *in situ* studying of the formation and growth of metallic NP in the GAS. It allows to detect and to monitor the peak of Localized Surface Plasmon Resonance (LSPR). It is possible to discuss about the number and size transformation of NPs based on the intensity, position and shape of

the peak. The main disadvantage of this approach is associated with limitations of the material to be detected: only plasmonic materials can be analyzed. Figure 9 demonstrates the experimental set-up used for the *in situ* UV-Vis measurements inside the aggregation zone. The construction of the GAS described in detail previously was utilized. Ag was chosen because it typically exhibits a sharp and intensive LSPR peak with the maximum around 360 nm. A source (Ocean Optics DH2000 BAL) was used to obtain a beam of light perpendicular to the GAS axis. An Ocean Optics STS Microspectrometer, 190-600 nm was utilized to collect the spectra. Both the light source and the detector were equipped with fiber optic cables which were mounted on quartz windows. A special optical system was used to produce the parallel light beam with diameter of 1 cm. The background was recorded without plasma. The integration time was varied from 0.01 s to 1 s depending on the experiments. The experimental parameters were completely the same as in the SAXS experiments. The construction of the moveable magnetron allowed to measure spectra at different distances from the target surface. Therefore, it was possible to perform mapping along the GAS axis.

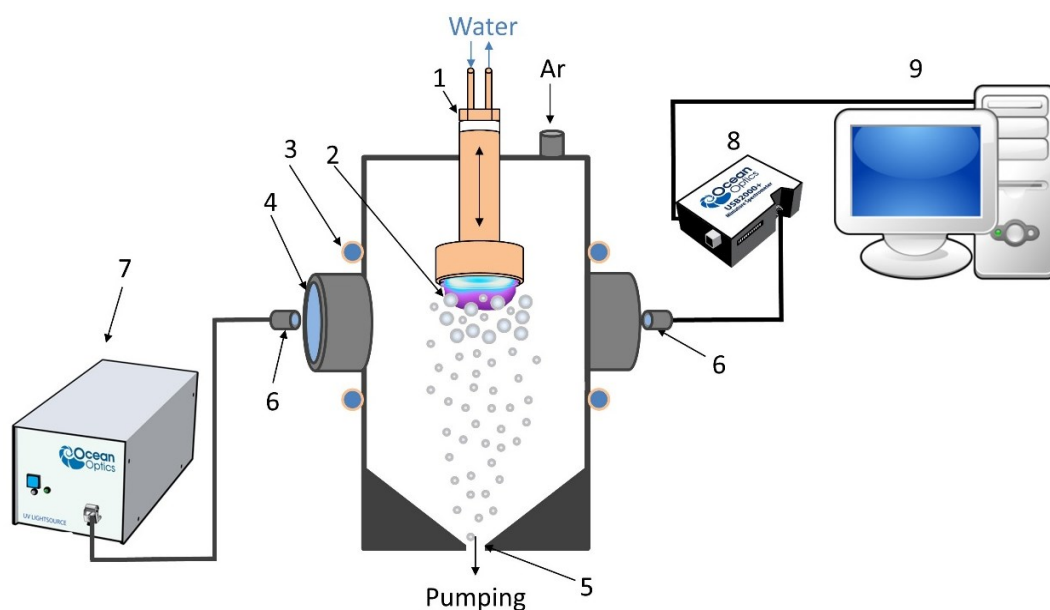


Figure 9. The scheme of the experimental equipment utilized for the in-situ UV-Vis spectroscopy measurements: 1 – moveable magnetron; 2 – plasma; 3 – water cooling; 4 – quartz window; 5 – orifice; 6 – fiber optic cables; 7 – light source; 8 – UV-Vis spectrometer; 9 – computer.

2.3. Methods for the sample characterization

2.3.1. Spectroscopic techniques

UV-Vis spectrophotometry

For the *ex situ* characterization of Cu and Ag NPs deposited on the substrates, UV-Vis spectrometry was applied. This technique allows the investigation of LSPR peak of plasmonic NPs deposited onto quartz substrates. Here, a spectrophotometer Hitachi U-2900 was used. The light source was equipped with deuterium and tungsten lamps for ultraviolet and visible spectral regions, respectively. The measurements were performed in the wavelength region of 200 – 1100 nm.

X-ray photoelectron spectroscopy

The X-ray photoelectron spectroscopy (XPS) was employed to determine the chemical composition of NPs, plasma polymer coatings and composites. The majority of the measurements were performed using an XPS spectrometer at the Department of Macromolecular Physics. It was equipped with an Al K α X-Ray source, which produced the photons with energy of 1486.6 eV, and with a hemispherical analyser (Phoibos 100, Specs, Germany). An anode was operated at the power of 200 W. Wide spectra were measured in the energy region of 0 – 1100 eV using the pass energy value of 40 eV. High resolution spectra were collected using 10 eV pass energy and 10 scans for each spectrum. All the measurements were performed under the ultra-high vacuum conditions ($5 \times 10^{-8} - 5 \times 10^{-10}$ torr). For the processing of the data, the Casa XPS software was utilized. All the spectra were calibrated with respect to the position of ether groups of C1s peak, which is located at 286.5 eV. Linear background was applied for the fitting of spectra.

Additionally, the measurements were performed using another spectrometer (Kratos Axis, Supra). It was equipped with a hemispherical analyzer and a monochromatic Al K α X-ray source (1486.6 eV). The XPS spectra were acquired from the area of $700 \times 300 \mu\text{m}^2$ with the take-off angle of 90° . Wide spectra were recorded with the pass energy of 80 eV, whereas the high resolution spectra - with the pass energy of 10 eV. The quantitative analysis of the C1s high resolution spectra were performed using the ESCApe (Kratos Analytical Ltd.) software after Shirley background subtraction. The best peak fits were obtained using a Gaussian-Lorentzian (70/30) algorithm.

Fourier-transform infrared spectroscopy

The Fourier-transform infrared spectroscopy (FTIR) measurements were performed using a spectrometer (Bruker Equinox 55) in a reflectance-absorbance mode. The spectra were recorded in the region of 4000 – 400 cm^{-1} . For these measurements, samples were deposited onto silicon substrates coated by a thin gold film. The resolution was set at 2 cm^{-1} . Processing of the spectra was performed using the software OPUS (BRUKER Optics).

Ellipsometry

Ellipsometry was applied to measure the thickness of thin polymer films. An ellipsometer (Woollam M-2000 DI) was used in this study. The measurements were realized at the angles varied from 55° to 75° . The results were fitted using a Cauchy model to determine the thickness of the coating.

Specific heat spectroscopy

An advanced technique of specific heat spectroscopy (SHS) in the configuration of AC-chip calorimetry was employed for the investigation of glass transition temperature of ppPEO matrix in nanocomposite Cu NPs/ppPEO coatings. Calorimetric sensors (XEN 39390, Xensor Integration, NI) were used (Figure 10). Every sensor was equipped with 6-couple thermopiles and two four-wire heaters (bias and guard heater). All the components were protected by a layer of SiO_2 with a thickness of 0.5 – 1 μm . Thin composite coatings were deposited directly over the entire surface of sensors.

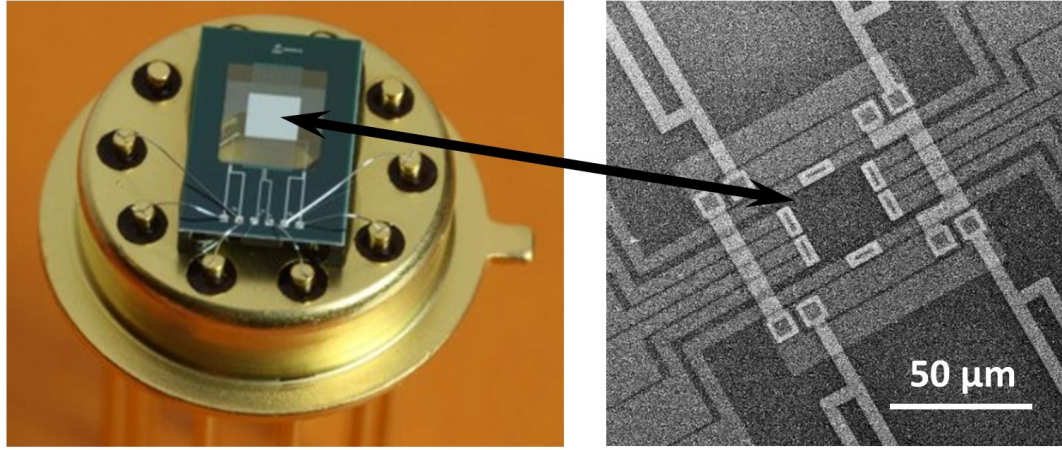


Figure 10. Photo of the sensor XEN 39390 (Xensor Integration, NI) (left) and SEM image of the hot spot (right).

The calorimetric investigations were performed in a temperature scan mode. The rate of heating/cooling was 2 K/min at a fixed frequency. The frequency was changed after every scan in the range of 1 Hz – 10⁴ Hz. The power of heating was constant at 25 μW. This value corresponds to the situation when the amplitude of the temperature modulation is less than 0.5 K. Thereby, the measurements were performed in a linear regime.

The differential approach was applied to minimize the heat capacitance of a blank sensor. According to this approach, the heat capacitance of the film may be determined as follows:

$$C_{film} = i\omega \bar{C}^2 (\Delta U - \Delta U_0) / SP_0 \quad (1)$$

where, ω – angular frequency ($\omega = 2\pi f$, f - frequency), $i = (-1)^{1/2}$. $C \equiv C_0 + G/i\omega$ characterizes the effective heat capacity of the blank sensor (C_0 – heat capacity of the sensor; $G/i\omega$ is the heat loss through the ambient atmosphere), S is the sensitivity of the thermocouple and P_0 is the applied power consumed for heating. ΔU means the complex differential signal of thermocouple for a blank reference chip and a chip with deposited film. ΔU_0 is the complex differential voltage recorded for two blank chips. ΔU means the complex heat capacity of the sample.

The AC-chip calorimetry principle consists in the measurement of complex differential voltage (ΔU) at different temperature and frequency. As follows from the equation 1, ΔU is related to the complex heat capacity and consists of the real part U_R and imaginary part corresponding to the phase angle ϕ . Therefore, the dynamic T_g can be determined as the temperature at half the step-height of the stepwise function of the

U_R and/or the temperature at which the peak function of the ϕ is maximum. The examples of both dependencies are presented in Figure 11.

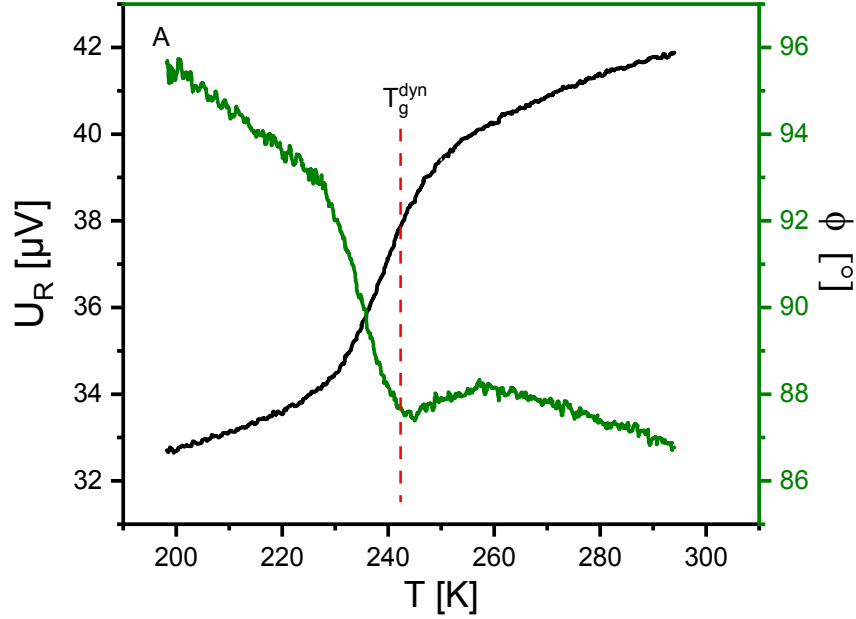


Figure 11. Raw data of the complex differential voltage with the real part (black) and the phase angle (green) for the ppPEO film without NPs, measured at a frequency of 160 Hz.

For the accurate and convenient determination of T_g from the temperature dependence of the real part U_R the approach described in Reference [30] was employed. Here, the first derivative of the U_R function with respect to temperature is taken. As a result, a function with maximum is obtained. This function can be fitted by a Gaussian curve and the dynamic T_g is determined as the position of the function maximum.

The thermal stability of the composite film is also an important factor for the calorimetric measurements. The preliminary experiments found that the calorimetric curves deviated significantly upon cycling heating up to the temperature 338 K whereas heating to 300 K did not lead to any change of the signal. This result allowed setting up the maximal temperature for the AC-chip measurements at 300 K.

2.3.2. Microscopy techniques

Scanning Electron Microscopy

Scanning Electron Microscopy (SEM) was used for the analysis of the NP morphology and for the calculation of the NP size distribution. A SEM (Tescan Mira III, at Charles University, Prague, Czech Republic) and a SEM (Supra55VP-Carl Zeiss, at Kiel University, Kiel, Germany) with in-lens detectors were operated in a secondary electron mode for the topography measurements. The acceleration voltage of 5 kV was employed during the measurements. The diameter of NPs was determined using the Solarius Particles software developed at the Department of Macromolecular Physics. The data for at least 150 NPs were taken into account for each sample. Moreover, the cross-section SEM measurements were performed in secondary electron and backscattered electron modes to characterize the interior structure of bi-layered Cu NPs/PEOpp composites. For these measurements, the hybrid films deposited on Si wafers were frozen in liquid nitrogen for 10 minutes and then were mechanically cleaved.

Transmission Electron Microscopy

Transmission Electron Microscopy (TEM) was utilized for deeper characterization of NP morphology and structure as well as for the investigation of the structure of the Cu NPs/PEOpp nanocomposite. A TEM (Jeol 2200FS) was used. The samples were deposited onto the carbon coated copper TEM grids (300 Mesh, Agar Scientific).

Atomic force microscopy

The topography of plasma polymer and composite samples was studied using atomic force microscopy (AFM). The measurements were performed by an AFM (Ntegra Prima, NT-MDT) in a semi-contact regime under the ambient atmosphere. Silicon AFM probes were used (Multi75Al-G with aluminum reflective coating, BudgetSensors[®], force constant = 3 N/m, resonance frequency = 75 Hz, typical radius of curvature < 10 nm). Every sample was measured at 5 different points. Processing of the images was done using the software Image Analysis (NT-MDT).

2.3.3. Water contact angle measurements

The surface wettability of the coatings with nanoarchitecture was measured using a self-developed goniometer based on a sessil water drop principle. The goniometer was equipped with a high-resolution camera and was controlled by the Solarius Wettability software (Department of Macromolecular Physics). Water drops of 20 μl volume were placed at 5 different places of a sample for better statistics.

2.4. Biological tests

2.4.1. Protein adsorption

The important characteristic of PEO is a non-fouling activity, i.e. the ability to stand against the adsorption of biomolecules. In this research, the non-fouling properties of Cu NPs/ppPEO films were tested in terms of the adsorption of proteins. Bovine serum albumin (BSA, Sigma-Aldrich, Inc.) was chosen as a model protein. The experimental protocol is schematically drawn in Figure 12. First, the solution of the protein was prepared such that BSA was dissolved in the phosphate buffered saline (PBS, Sigma-Aldrich, Inc.) to obtain the concentrated solution of 5 mg/ml. The working solutions were prepared by diluting the stock solution to the final concentration of 50 $\mu\text{g/ml}$. Silicon wafers (1 cm \times 1 cm) covered by the studied films were placed into standard well-plates. 2 ml of BSA solution was added to every sample. The incubation time was 20 min. After the incubation, the samples were rinsed by de-ionized water twice to remove physically sorbed BSA and were dried under the ambient conditions. The XPS measurements were performed to detect the signal from nitrogen which is present in BSA but absent in the films.

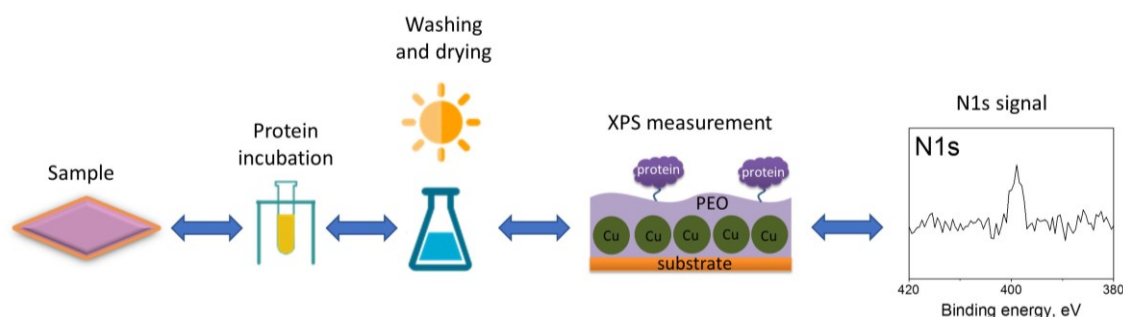


Figure 12. The scheme of protein adsorption test.

2.4.2. Antibacterial tests

One of the aims of current research was to obtain the Cu NPs/PEOpp composites with bactericidal properties. The control of the antibacterial activity of the composites was performed at the Gamaleya National Research Centre in Moscow (Russia). The Gram-positive bacterium *Staphylococcus aureus* (methicillin-resistant strain SA180-F) and the Gram-negative bacterium *P. aeruginosa* (strain PA21) were used as multidrug-resistant bacteria. Table 1 describes the characteristics of the bacterial strains, where AMC – amoxicillin, AMP – ampicillin, CTX – cephalexim, CN – gentamicin, F – nitrofurantoin, IPM- imipenem, M – methicillin, MEM- meropenem, SXT-trimetoprim/sulfamethoxazol, SCF- sulbactam/cephoperason.

Table 1. The main characteristics of the bacterial strains used in the research.

Species	Strain	Genotype	Resistance	Source
<i>Staphylococcus aureus</i>	SA180-F	Wild type	M	Clinical isolate
<i>Pseudomonas aeruginosa</i>	PA21	Wild type	AMC, AMP, CTX, CN, F, IPM, MEM, SXT, SCF	Clinical isolate

To evaluate the bactericidal activity against planktonic bacteria, the nanocomposite films were prepared by depositing two layers of Cu NPs onto glass substrates followed by overcoating them with 10 nm of ppPEO. The samples were placed into 12-well plates with the active surface facing upward. Overnight *S. aureus* SA180-F culture was diluted in PBS up to 1×10^6 CFU/ml. Each well was filled with 3 ml of the bacterial suspension and the samples were incubated at constant temperature of 37 °C and constant shaking (150 rpm) for 3 hours. Decimal dilutions of the bacterial suspension were seeded onto nutrition agar (BHI agar, Difco) and incubated at 37 °C for 24 h, then the bacterial colonies were counted and the concentration in CFU/ml was calculated.

The antibacterial activity against bacteria in biofilms was tested on the *P. aeruginosa* strain 21. The samples were placed into 24-well plates with the active surface facing upward and 1 ml of the bacterial suspension was added to each of the

wells with the initial concentration of 1×10^7 CFU/ml. The samples were incubated for 24h at 37 °C without shaking. After the incubation, the samples were taken out from the solutions and flushed with the culture medium to remove weakly-adhering bacteria. The bacteria remaining on the surface were stained by a LIVE/DEAD kit (Invitrogen, USA) to distinguish the living bacteria (green) from the dead (red) by fluorescence microscopy. The staining was produced according to the instructions of the manufacturer.

3. RESULTS AND DISCUSSION

3.1. Ag and Cu nanoparticle deposition and characterization

3.1.1. *Ex-situ* characterization of Ag and Cu NPs

The construction of GAS described in Section 2.1 was utilized for the fabrication of Ag and Cu NPs used afterwards in the preparation of antibacterial coatings. The experimental parameters for both metals were optimized to achieve the highest deposition rate which was monitored using QCM. First of all, the NPs were deposited onto the Si substrates and TEM grids to characterize their morphology and size. Figure 13a and Figure 13b show the shape of Cu NPs and Ag NPs, respectively. The high resolution TEM images of NPs are presented as incuts. Well dispersed and polydisperse NPs of both metals are shown. TEM images successfully confirmed the crystalline nature of NPs. Moreover, the NPs of size > 20 nm are polycrystalline. Size distributions were calculated from these images. The size histogram for Cu NPs is shown in Figure 13c and for Ag NPs in Figure 13d. The mean diameters estimated for Cu and Ag NPs were 22 ± 5 nm and 25 ± 6 nm, respectively.

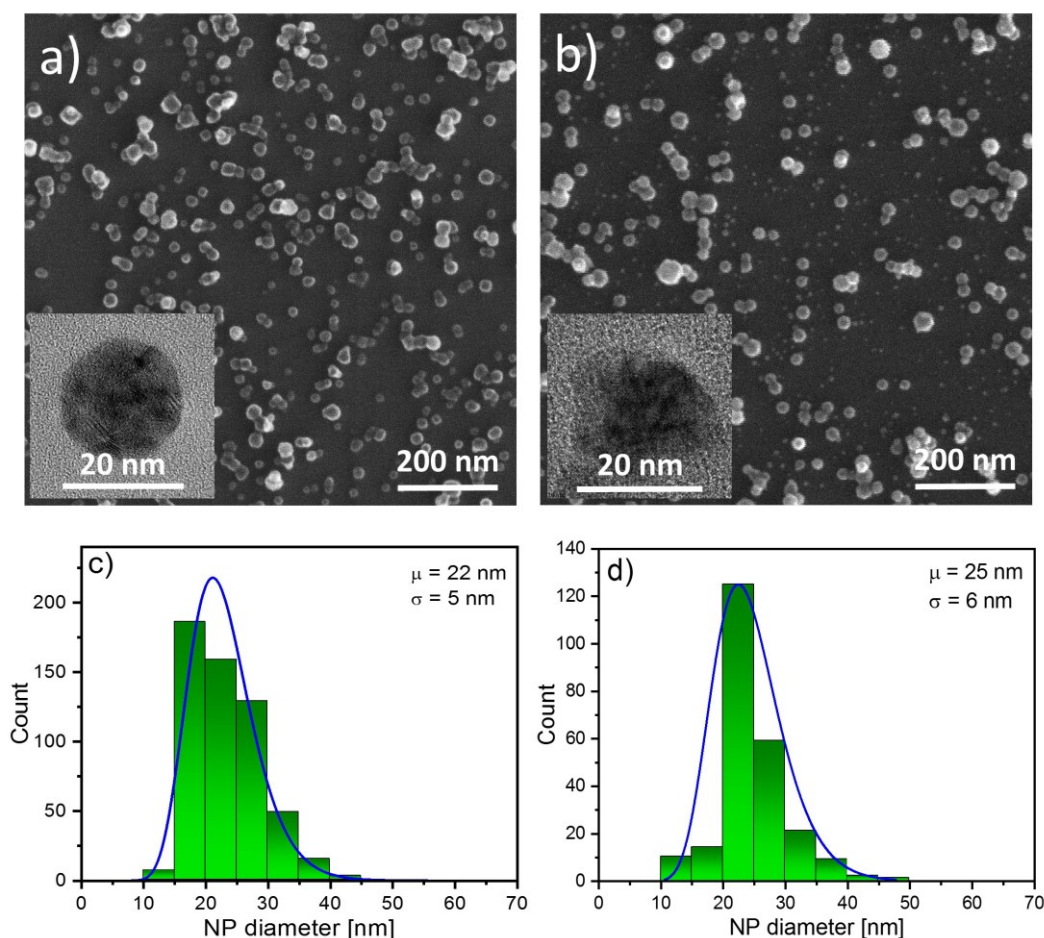


Figure 13. The SEM and TEM micrographs of (a) Cu NPs and (b) Ag NPs. Images (c) and (d) demonstrate corresponding size distributions (μ – mean diameter, σ – standard deviation).

It is known that Cu and Ag NPs are useful for optical applications. Both types of NPs demonstrate pronounced LSPR peak in the visible spectral region [98, 99]. The UV-Vis spectra of the NPs deposited on glass microscope slides are shown in Figure 14. The absorbance maximum of Cu NPs is situated at 745 nm (see Figure 14a). Moreover, the peak is relatively broad that also indicates polydispersity of NPs. The opposite situation was observed in case of Ag NPs. The sharp and narrow LSPR peak with maximum at 365 nm was found (see Figure 14b). The presence of LSPR peaks in UV-Vis spectra indirectly confirms the absence of strong oxidation of NPs after their extraction from vacuum to the ambient atmosphere.

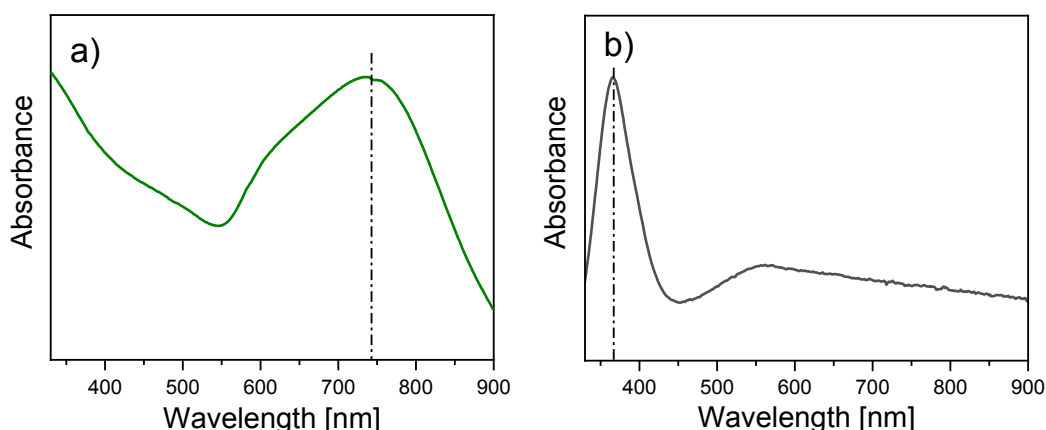


Figure 14. UV-Vis spectra of (a) Cu NPs and (b) Ag NPs.

For direct confirmation of the oxidation state of NPs the XPS spectra were measured. For these measurements several layers of NPs were deposited onto the PTFE foil to exclude the oxygen contribution from the substrate. High-resolution spectra of Cu 2p and Ag 3d peaks are presented in Figure 15. Unfortunately, it is challenge to differentiate metallic Cu and Cu (I) oxide. However, the Cu (II) oxide has obvious satellites in the spectrum that help to identify it. In case of our NPs, no satellites were observed in Figure 15a. Silver differs from silver oxide by small binding energy shift toward higher values. This shift was not seen in Figure 15b. Therefore it was confirmed by UV-Vis and XPS that after the exclusion from vacuum Cu NPs did not oxidize very fast and keep their metallic state. This result is important for later experiments with nanocomposites.

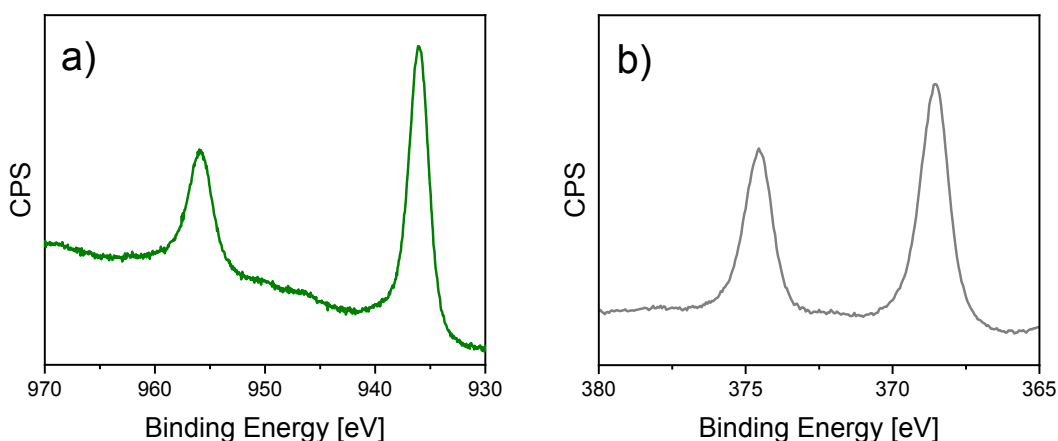


Figure 15. High-resolution XPS spectra of (a) Cu 2p peak and (b) Ag 3f peak.

3.1.2. In-flight diagnostics of the NP growth performed by SAXS

The variety of methods, such as SEM, TEM, UV-Vis spectroscopy, XPS etc., are used for thorough characterization of NPs deposited onto substrates. However, characterization of NPs during their formation and growth in GAS has not been realized. The original model of GAS with several ports for the *in-situ* diagnostics was designed in our department.

The SAXS measurements using the synchrotron radiation is a powerful source of information sensitive at nano-scale. Therefore, our prototype of GAS was installed at the P03 beamline of PETRA III, DESY. The SAXS measurements were performed using Cu and Ag targets and a part of results will be described below.

One of the advantages of our GAS was the possibility to realize spatial measurements in axial and radial directions. Minimally 16 scattering curves were fitted with a full sphere model with lognormal size distribution to calculate the NP mean diameter and error bar at every spatial point. Moreover, the relative volume fraction, which describes the ratio of the volume occupied by all the NPs to the sampled volume defined by the beam size, was determined. The axial distributions obtained for Cu NPs and Ag NPs are presented in Figure 16. The position $x = 0$ mm corresponds to the surface of the target. In both cases, the first NPs were found already at 1 mm from the target. The diameter of Cu NPs was around 30 nm. Then the NP diameter increased and reached maximal value around 90 nm at 3 mm from the target. It should be noted that we observed occasionally such big NPs on the substrates positioned outside the GAS, but their number was negligible in comparison with the number of < 30 nm NPs. At the same time, the relative volume fraction also increased by a three-order magnitude. We concluded that in first 3 mm from the target, the nucleation and growth of NPs took place. However, the mean diameter and the relative volume fraction kept approximately constant in the region from 3 to 9 mm away from the target. In the next region, both parameters abruptly decreased and also remained approximately constant up to the deposition on the substrate placed behind the orifice. The mean diameter of NPs in this region reached 15 nm. NPs of the similar size were found behind the exit of the GAS.

The same tendency was found during the experiments with Ag NPs. Trapping region rich in big NPs was observed in a few nm from the target. Further, the NP

diameter and the relative volume fractions smoothly decreased with the distance from the magnetron.

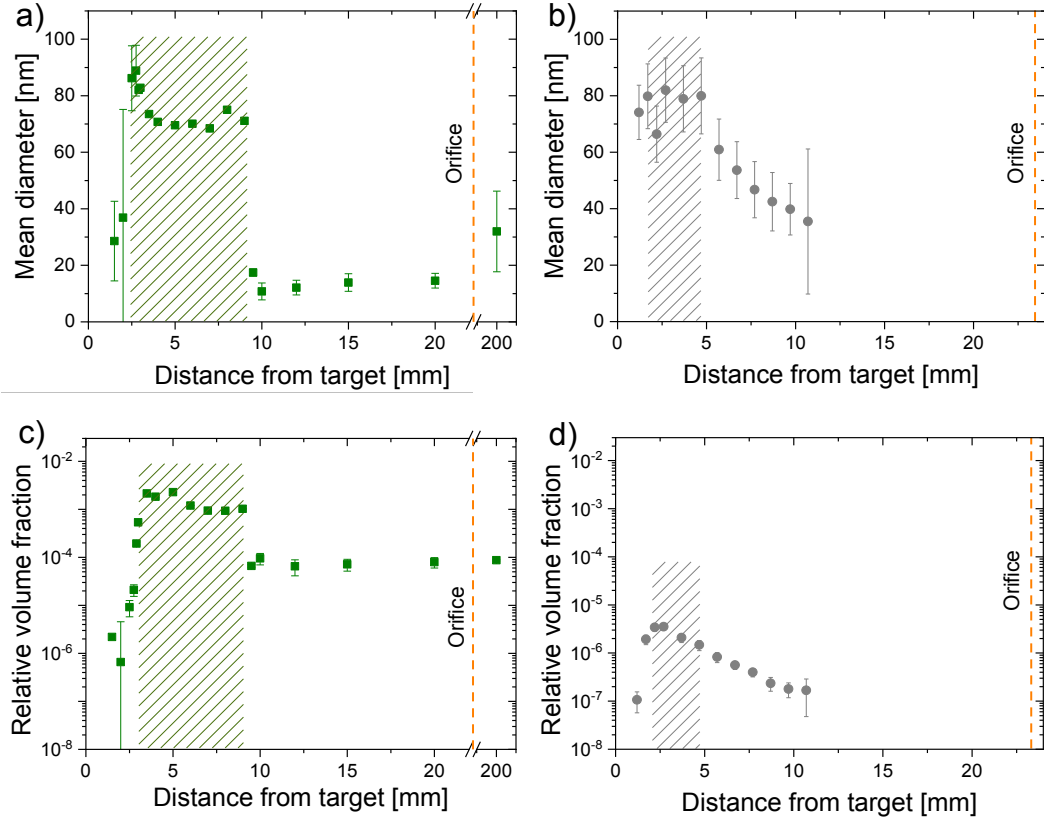


Figure 16. The distributions of mean diameter and relative volume fraction along GAS axis calculated for (a, c) Cu NPs and Ag NPs (b, d).

The determination of radial distributions of the NP size and the relative volume fraction was another important part of the research. The measurements were performed for Cu NPs at the x distance of 5 mm from the target in the radial direction. This position was chosen due to the good intensity of the scattering signal. The radial distributions are presented in Figure 17. It is seen that the NP size kept constant above the center of the target. Nevertheless, it slightly decreased in the direction toward the erosion track. The similar tendency was found for the relative volume fraction. The scattering intensity was obviously lower at 12 mm from the magnetron than on the axis, regardless the higher concentration of sputtered atoms here. The characteristics of the experimental equipment did not allow for the measurements directly above the erosion track.

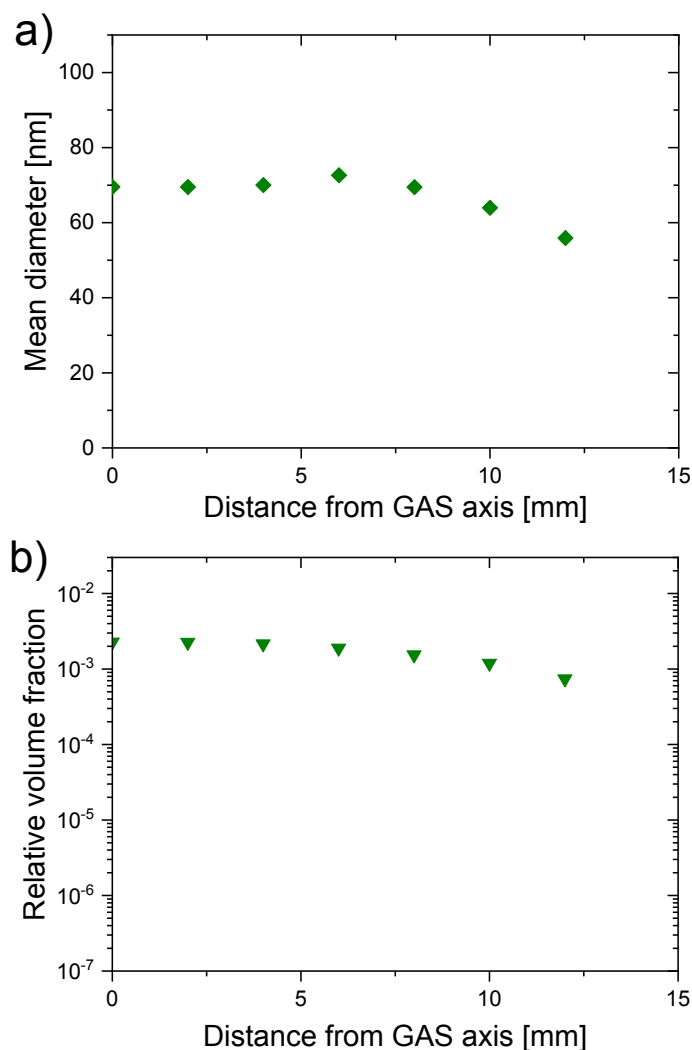


Figure 17. Radial distributions of (a) Cu NP mean diameter and (b) relative volume fraction at the axial distance of $x = 5$ mm.

For the confirmation of the SAXS results, Cu NPs were collected on the Si substrate placed at the distance of $x = 200$ mm behind the orifice and SEM analysis was performed. The NP top view and the size distribution calculated from the SEM image are shown in Figure 18. The NP spot had a circular shape on the substrate and the number of NPs decreased from the center toward the edge of the spot. The SEM images were measured at the edge for more precise calculation of the NP size. It is worth noting that the mean diameter of 32 ± 14 nm obtained from the SAXS data is in good agreement with 27 ± 8 nm determined by SEM.

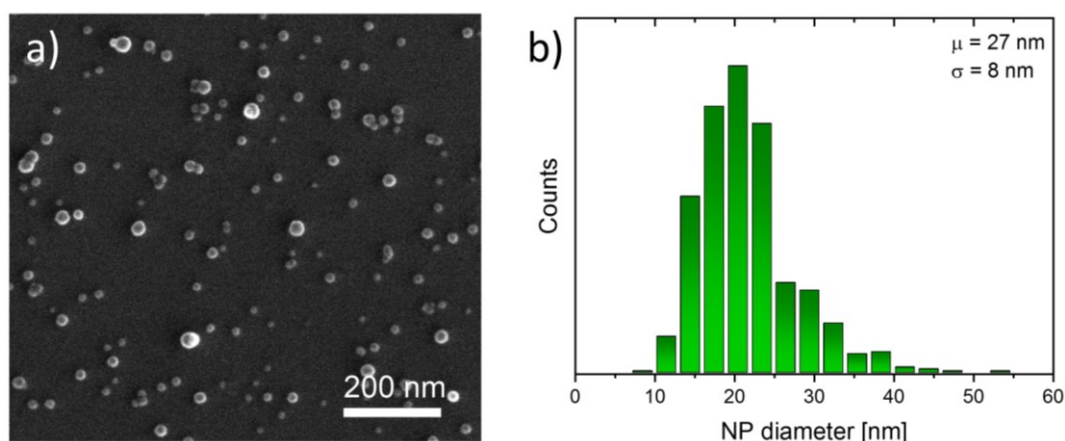


Figure 18. (a) SEM image of Cu NPs deposited during the SAXS measurements and (b) corresponding size distribution.

Thereby, it can be concluded that Cu and Ag NPs are formed in the vicinity of the target. Moreover, big NPs with the mean diameter $> 80 \text{ nm}$ were observed by SAXS in the region at $3.0 - 10.0 \text{ mm}$ from the target. Radial measurements revealed that big NPs were mostly trapped above the center of the target while small NPs were distributed also in the direction of the erosion track. Nevertheless, we assume that the trapping region is restricted in the lateral plane by the plasma ring. It was also found that a certain amount of small NPs was not captured in the close-to-magnetron region and travelled with the flow of the carrier gas out of the source. It was successfully confirmed by SEM measurements of NPs deposited on the substrates placed behind the orifice. In our opinion, the trapping effect is caused by the action of different forces including electrostatic, gravitation, the ion drag, the neutral drag and the thermophoretic force. The force equilibrium may induce the formation of the NP cloud above the target. It is known that particles acquire the electric charge in plasma. Therefore, the electric field may strongly affect their behavior. It was published previously that NPs of the size of $70 - 90 \text{ nm}$ possess the negative charge of about 10^2 elementary charges per particle.[100] Probably, the forces induced by the electric field of these charges are able to balance another forces acting on NPs. The hypothesis of the electrostatic origin of trapping is supported by the effect observed by QCM. The temporal dependence of the deposition rate during the Ag NP deposition is presented in Figure 19. The significant increase of the deposition rate at 66 s corresponds to the moment when the discharge was switched off. At this moment, electrostatic force

obviously stopped acting and the NP cloud was blown out of the aggregation zone with the Ar flow.

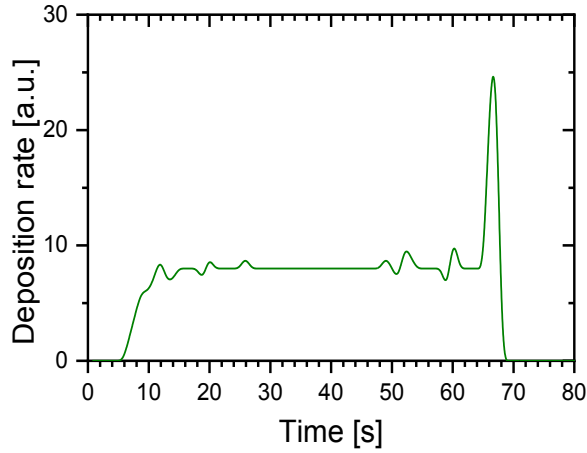


Figure 19. The temporal dependence of the deposition rate measured by QCM outside the GAS at $x = 200.0$ mm.

3.1.3. *In-situ* detection of NPs by UV-Vis spectroscopy

SAXS provides a wealth of information about the NP size distribution and their number density inside the GAS. However, it should be noted that synchrotron experiments are very complicated, time consuming and expensive. Therefore, the search for relatively simple and cheap route for the in-flight control under the NP formation is an actual problem. The preliminary experiments demonstrated that UV-Vis spectroscopy could be applicable for the detection of Ag NPs inside the GAS.[101] In such approach, the UV-Vis light beam meets the Ag NP beam and plasmon resonance signal appears on the detector. It is known that the position of the plasmon peak is related to particle size, the parameter of full width of half maximum (FWHM) characterizes the dispersity and the peak intensity is associated with the NP number density. Therefore, the analysis of UV-Vis spectra measured *in-situ* in GAS may be useful for the investigation of the formation and growth of metal NPs exhibiting the plasmon resonance.

Firstly, in-flight UV-Vis detection of the Ag NPs was tested in the main chamber (outside the cluster source). Figure 20 shows the UV-Vis spectra measured during the GAS operation and in 1.5 seconds after the discharge shutdown. Here, the obvious band appears in the visible region of spectrum. The position of this band at $\lambda = 365$ nm fits with the position of LSPR of Ag NPs.[102] It is worth mentioning that

the abrupt increase of the transmittance was detected in a few seconds after the discharge shutdown. This observation can be assigned to the movement of the NP cloud, which was trapped in near-to-electrode region under the simultaneous action of the electrostatic and aerodynamic forces, across the light beam. Indeed, such effect directly confirms the findings obtained earlier by SAXS and QCM. When the discharge was switched off, the equilibrium of the forces was violated and NPs were swept out of the aggregation zone. Noteworthy, the 7 nm blueshift of the peak maximum was revealed. The origin of such shift is not evident; however, it can be attributed to the increase of the number of small particles in the NP beam which were also captured in the aggregation zone and then released after plasma shutdown.

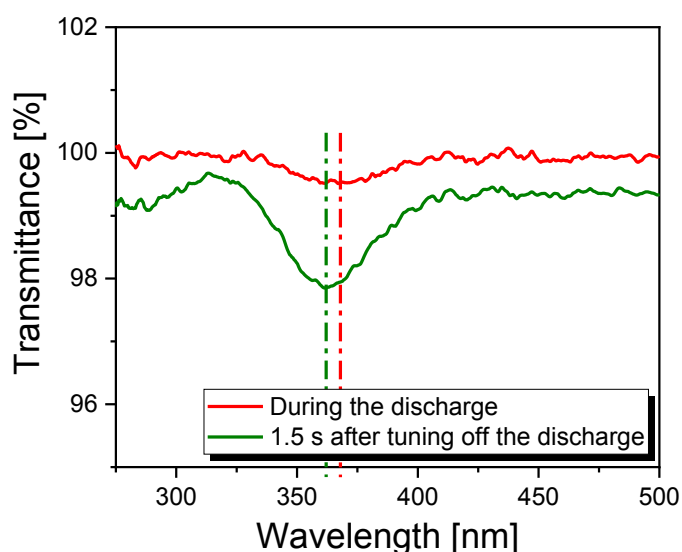


Figure 20. UV-Vis spectra measured outside the GAS.

When the feasibility of UV-Vis spectroscopy measurement for the NP detection was verified, the measurements inside the GAS were performed. The optical waveguides from the light source and to the detector were mounted onto the quartz windows in the configuration shown in Figure 9. The UV-Vis spectrum was acquired when the discharge was off and it is shown as the background levelled at 100 % of transmittance (Figure 21). A distinct absorption band appears in the spectrum when the discharge is turned on. The strongest LSPR is observed in the closest position of 5 mm between the light beam axis and the target plane (here, the light beam with a diameter of 10 mm is just about to touch the target by its lateral side, see also Figure 21). Even a small shift of the magnetron to the position of 10 mm leads to a significant decrease, yet to a detectable level, of the absorption intensity, which remains approximately constant at farther distances from the magnetron. The results indicate

that the concentration of Ag NPs does not change significantly along the GAS, except for the region nearest to the magnetron target where the amount of NPs is substantially higher. This finding agrees with a concept of the ‘trapping region’ that exists at the several mm distance from the target and where NPs become ‘trapped’, as discovered by our recent *in situ* SAXS measurements on Cu NPs.[103]

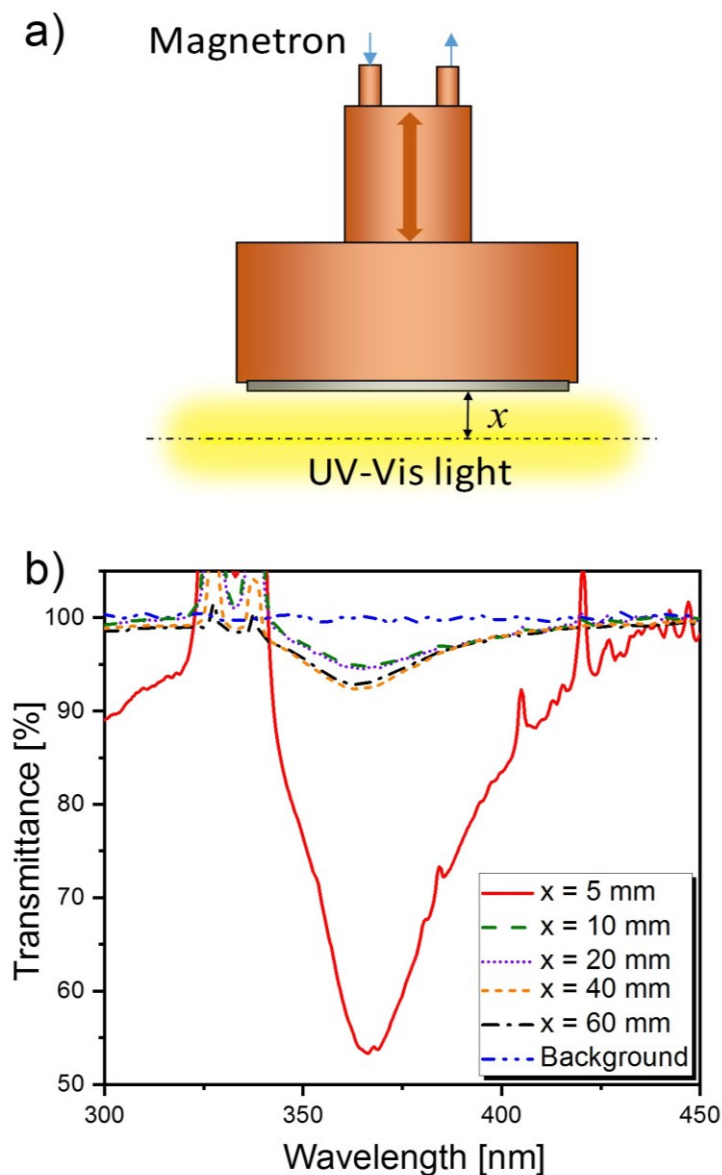


Figure 21. a) Scheme of the light beam probing the space in the vicinity of the magnetron; b) UV-Vis spectra measured at different distances from the target. The distance is taken from the light beam axis to the target plane.

Further evidence about the existence of the trapping region can be obtained from the time-resolved UV-Vis measurements performed after switching off the

discharge. In this experiment, the magnetron was positioned at 20 mm from the light beam axis, leaving a 15 mm gap between the target plane and the lateral side of the light beam. The discharge was turned on and the acquisition of the spectra was started with periodicity of 0.1 s and the acquisition time of 100 ms. After the stabilization of the parameters, the discharge was turned off, but the acquisition of the spectra proceeded. Figure 22. Optical transmission spectra acquired at $x = 15$ mm when the discharge is on (time 12.3 s) and after turning off the discharge (time > 12.3 s). shows the spectrum acquired just before and after the discharge was turned off. The plasma-on spectrum is distinct from the other spectra by the presence of Ag atomic emission lines. After the extinction of the discharge, the Ag lines immediately disappear but the LSPR band demonstrates a noteworthy evolution. Not only does it remain detectable, but it even increases in intensity for about 0.5 s, abruptly disappearing afterwards.

The phenomenon can be also related to the existence of high amount of NPs trapped in the capture zone which exists at the distance < 15 mm from the magnetron target. The trapped Ag NPs become released after the extinction of the discharge and start travelling with the gas flow along the aggregation chamber to the exit orifice. Under the chosen Ar flow rate, a fraction of a second is required for the gas to bring the cloud of the NPs from the trapping region to the light beam axis and this agrees with the 0.5 s time lag at which the intensification of the LSPR band was observed. At later time, the NP cloud leaves the space probed by the light beam and travels towards the orifice. This leads to a decrease of the LSPR band intensity to the background level.

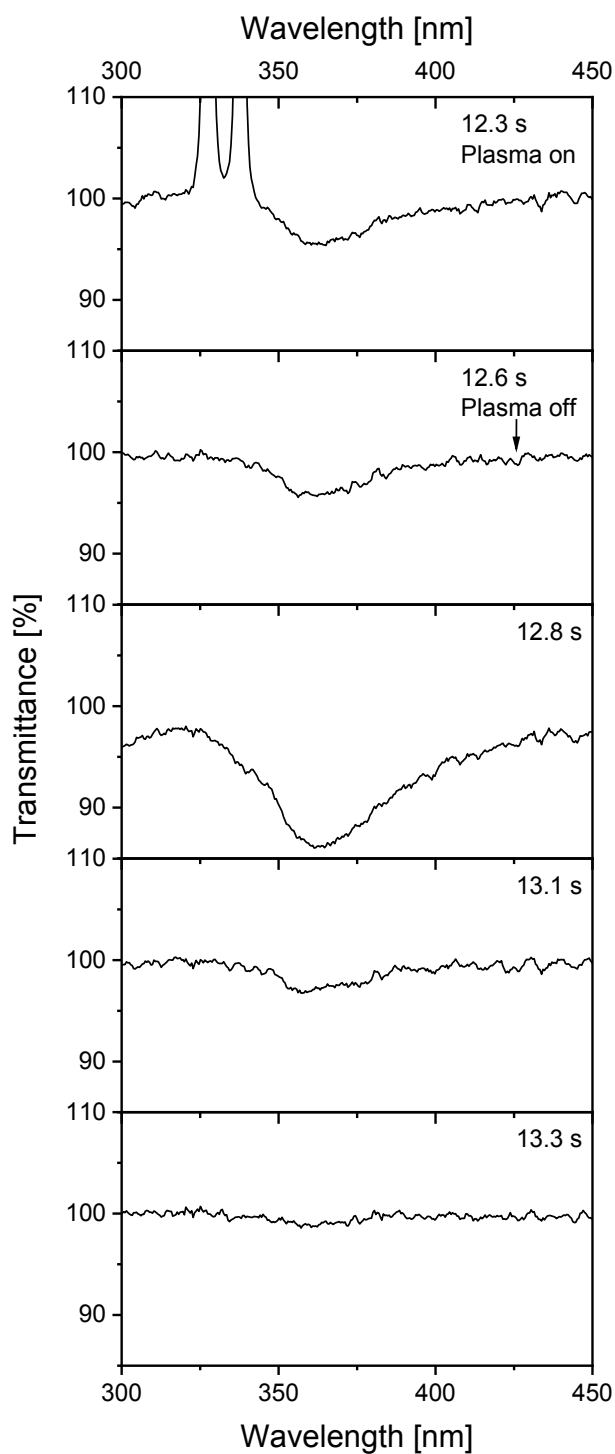


Figure 22. Optical transmission spectra acquired at $x = 15$ mm when the discharge is on (time 12.3 s) and after turning off the discharge (time > 12.3 s).

3.1.4. SEM imaging of Ag NPs collected inside the aggregation chamber

In previous chapters, the successful application of SAXS and UV-Vis spectroscopy for the *in-situ* detection of NPs in the aggregation zone was demonstrated. At the same time, the prediction of the NP morphology by these techniques is a challenge due to

the complicated fitting of scattering curves and ambiguous data interpretation. Nevertheless, the scientific community utilizing GASEs is highly interested in unveiling the kinds of NPs that exist in the aggregation chamber. One of the possibilities is to collect the NPs inside the aggregation chamber and to characterize them *ex-situ*. As was previously mentioned, our design of the cluster source was equipped with a window for the discharge observation. Surprisingly, a huge dark spot appeared in the center of the silver target after 20 hours of the operation under the conditions similar to the DESY experiment (current – 600 mA, gas – Ar, flow – 18 sccm and pressure – 126 Pa). This target was immediately uninstalled from the magnetron for the subsequent characterization. The top view of the target and side view of the spot are shown in Figure 23a and Figure 23b. It is seen that the diameter of the spot is larger than 1 cm. The profilogram, which was measured across the central part of the target, is presented in Figure 23c. The height of the „hill“ formed by the NPs was estimated to be ~ 800 μm . It was also found that the depth of the erosion track was ~ 300 μm . We assume that this spot consists of the NPs redeposited onto the target after the discharge shutdown.

In order to analyze the structure of the deposit, we used a fresh Ag target and sputtered it only for 10 sec. The SEM analysis was performed outside the erosion track corresponding to point 2 (Figure 23d) and at the target center corresponding to point 1 (Figure 23e). The central spot is characterized by the presence of agglomerates of NPs, with the mean size of individual NPs reaching 89 nm. Markedly, the 10 second sputtering is sufficiently long for the deposition of the amount of the NPs which exceeds the monolayer coverage in the central area. A smaller amount of NPs is detected outside the erosion track.

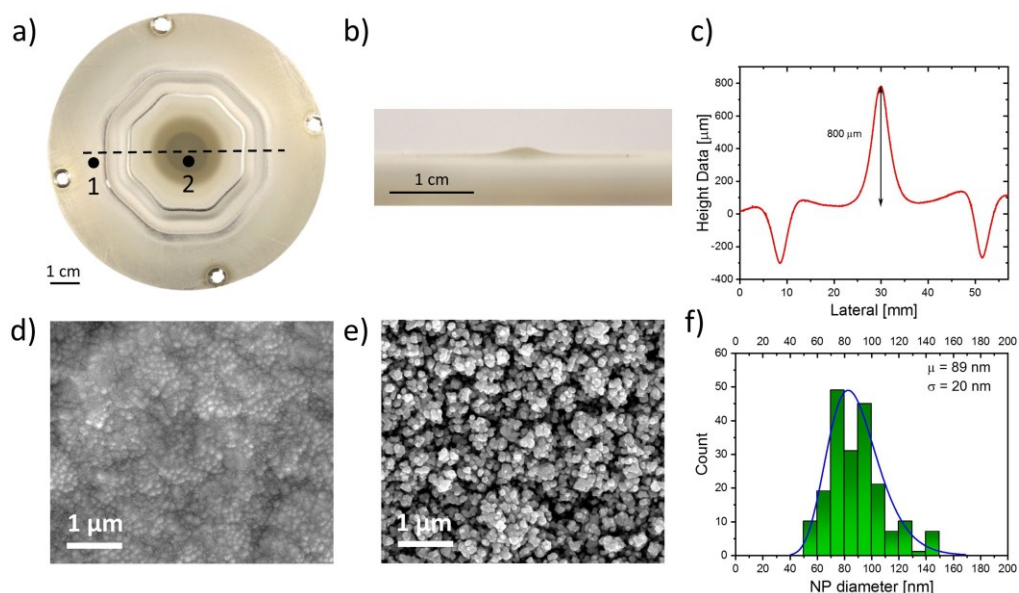
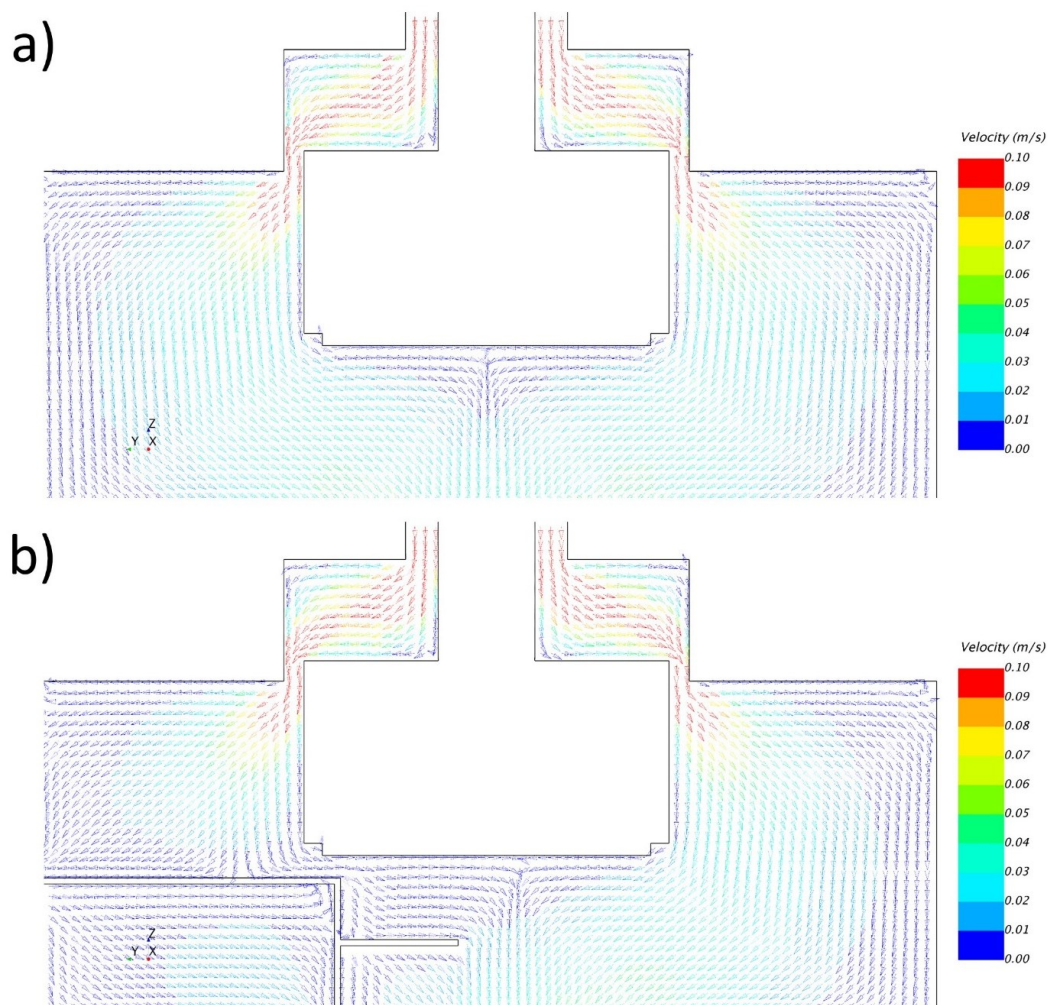


Figure 23. Characterization of the target surface: a), b) top view and side view photos of the target showing the macroscopic re-deposit of Ag NPs in the central area (taken after 1 week of the experimental campaign); c) profilometry height profile of the re-deposit of NPs corresponding to the dotted line on the top view image; d) and e) SEM images of the target surface acquired at the periphery (spot 1) and in the center (spot 2) after 10 s of sputtering of fresh target; f) size distribution of the NPs redeposited in the central area of target, the curve corresponds to the lognormal fit to the data.

The observed effect of the backward deposition of the NPs onto the target surface is quite remarkable, especially taking into account that NPs have to overcome the neutral drag force (i.e. the force produced by the momentum transfer from the neutral atoms of the flowing gas onto the NPs) and the gravity force to reach the target. For example, the simulations of the Ar flow (Figure 24a) indicate that the gas velocity vectors have a strong co-axial component directed downward to the exit orifice, except for the space closest to the target, where the radial component dominates and is directed from the target edges towards the center. In the region of interest (several mm from the target), the gas flow therefore tends to push the NPs radially from the periphery towards the center and then axially downward towards the orifice. This contributes to the localization of the NPs in the central part below the target. Nevertheless, there is no velocity component that would drag the NPs from the trapping region in the upward direction. It has been already discussed that NPs become

electrically charged when formed in the plasma. Our earlier *in situ* SAXS measurements confirmed that charged Cu NPs can be held close to the magnetron by electrostatic interactions.[103] These may force part of the NPs to travel against the gas flow and the gravity and reach the target. Therefore, we believe that electrostatic interactions are also responsible for the phenomena observed here for Ag NPs, although the detailed mechanisms are yet to be discovered.



+

Figure 24. Simulation of the Ar flow in the vicinity of magnetron a) without sample holder; b) with sample holder inside.

The redeposition of big NPs onto the target was successfully confirmed above; however, there are other possible ways of the NP loss in the aggregation chamber, for example, the deposition on the walls. This idea is indirectly supported by the SAXS results obtained for Ag NPs (see Figure 16b) where the average size of NPs gradually decreased in the direction of orifice. Therefore, the next step was to investigate the

changes of the NP size along the GAS axis. For this aim, the self-constructed cascade sample holder was mounted onto the diagnostic port. The main advantage of this holder was the possibility to place Si substrates close to the magnetron axis (20 mm radially shifted) at different distances from the target plane (as shown in Figure 8 in Experimental). The simulations of the gas flow confirmed that the gas velocity map changes in the proximity of the substrates but remains qualitatively similar close to the target (Figure 24b). Hence, we believe that the introduction of the substrates does not change significantly the phenomena related to sputtering itself as well as to nucleation and growth of the NPs. In the first attempt, the NPs were collected by the side facing the plasma. The distance between the target and the substrates was 2.0, 5.0, 7.5, 10.0 and 11.5 cm, respectively. After loading, the system was evacuated and 10 s deposition was performed. Then the holder was extracted from the GAS and the samples were analyzed by SEM.

The SEM micrographs of the NPs found at distances 2.0, 7.5 and 11.5 cm from the target are presented in Figure 25. Huge amount of Ag NPs was collected on the substrate closest to plasma. These NPs were mostly coagulated and constituted the mesoporous pattern. Such effect may be associated with relatively high temperature of the NPs during the first seconds after their formation, which triggers the coagulation after the deposition on the substrate. Average diameter estimated using just isolated NPs was 46 nm that is twice less than the size of the NPs redeposited onto the target. At the distance of 7.5 cm, the number of the NPs as well as their average size evidently decrease (32.7 nm) and the NPs were not coagulated. However, the growth of Ag nanoislands was detected on Si surface in between the NPs. It can be concluded that even at the distance of 7.5 cm the concentration of Ag atoms in the gas phase is high enough to initiate the Volmer-Weber growth of Ag film. Finally, only isolated NPs were found near the orifice.

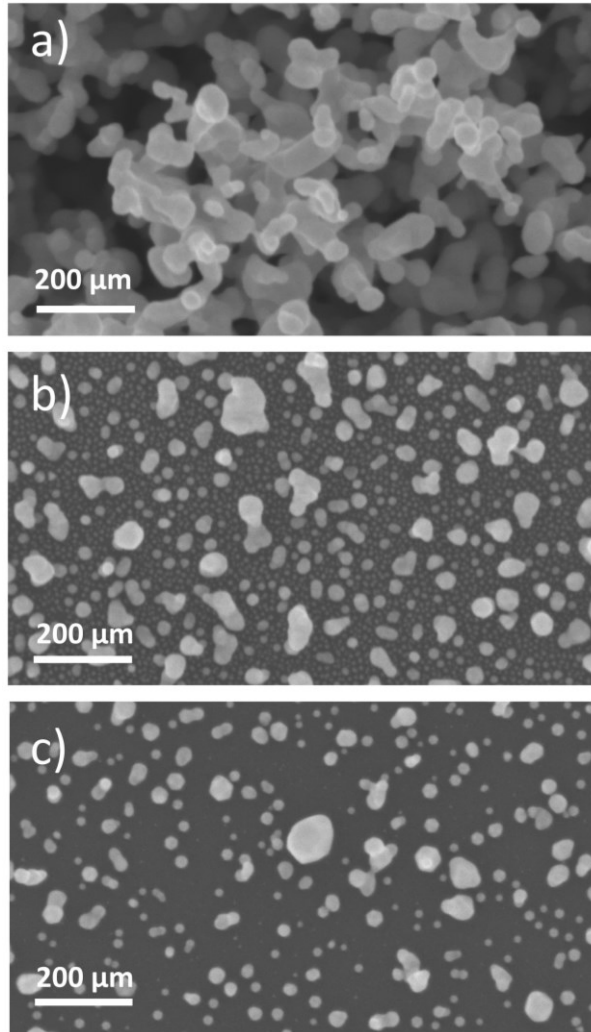


Figure 25. SEM images of Ag NPs collected inside the GAS at different distances from the target: a – 2.0 cm; b – 7.5 cm; E – 11.5 cm.

Figure 26 a-f) shows the size distributions calculated for each position of the substrate including NPs collected behind the orifice. All distributions were approximated by the lognormal function and the average diameters were determined. The axial distribution of the NP size is presented in Figure 26g. The NP average diameter in the GAS gradually decreases in the direction of the exit orifice. It should be noted that the diameters measured in the last two positions well correlate with the mean diameter of the NPs collected behind the orifice. This observation is in good accordance with the results obtained by SAXS which revealed the particle size of about 40 nm at the distance of 1 cm from the magnetron. Moreover, the size distribution demonstrates a progressive decrease of the number of big NPs with the average size > 40 nm in the direction of the orifice. It can be concluded that bigger NPs become

captured in the plasma and lost afterwards on the target as well as inside the aggregation chamber. On the contrary, small NPs continue their movement toward the orifice where they are accelerated by the gas expanding to the deposition chamber.

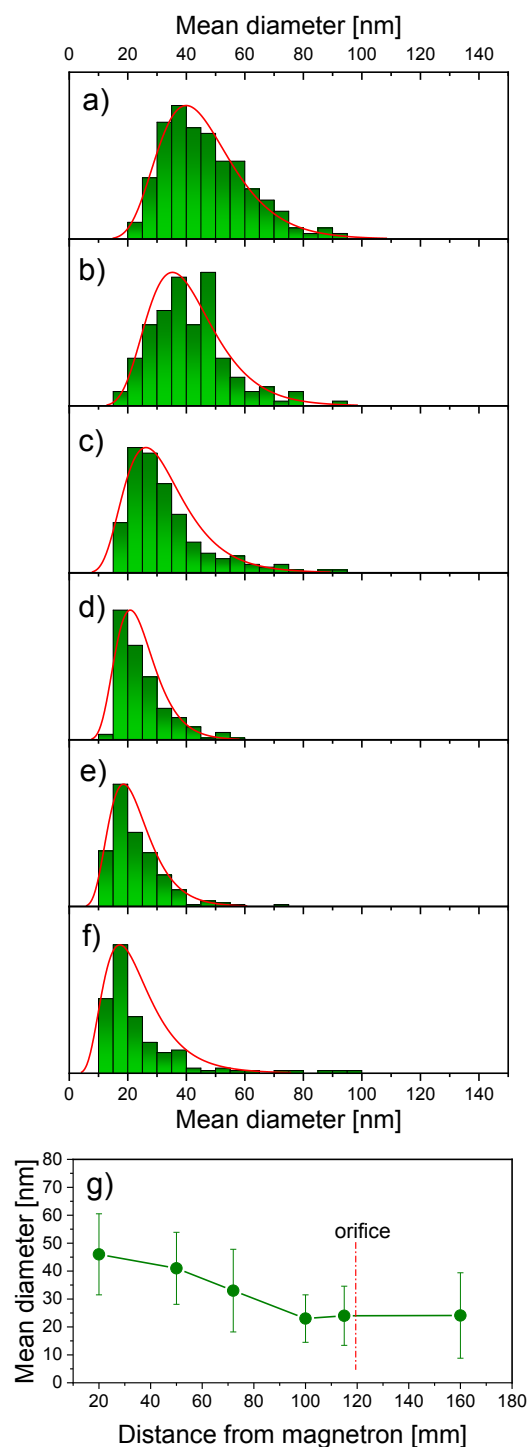


Figure 26. NP size distributions calculated for the samples placed at different distances from the target: a) 2 cm; b) 5 cm; c) 7.5 cm; d) 10 cm; e) 11.5 cm; f) 16 cm (behind the orifice) and g) axial distribution of average size.

The SEM images of the deposited samples are shown in Figure 27, where the NPs collected on the substrates facing the target (top – a, b, c) are compared with those collected on the substrates facing the orifice (rear – d, e) as well as with those deposited outside the GAS (f). The reason for the observations from the rear side was to limit the deposition of Ag atoms and minimize the formation of nanoislands from them. Indeed, the sample deposited at the closest distance of 2.0 cm and facing the target is characterized by a complex structure. It consists of a discontinuous film (most probably grown as a result of atomic sputter-deposition) and individual spherical NPs incorporated into it. The rear side sample is characterized by the absence of the film and by the presence of the NPs of a spherical as well as of an irregular shape. The formation of the irregularly-shaped NPs is probably given by the coalescence of smaller NPs which did not suffice to thermalize and remained at the temperature close to the melting point.

At farther distances, the formation of the film is not observed anymore for either of the samples, pointing to a decrease of the atomic metal flux to negligible values. Coalesced NPs can be occasionally observed; however, individual spherical NPs dominate in the samples. This finding agrees with an idea that NPs are born in a liquid state close to the magnetron target but then undergo phase transition and thermalization via the collisions with atoms of the cold buffer gas.

The size distribution histograms were calculated (Figure 28) and they show that the mean NP diameter decreases from 33 nm to 18 nm with the distance from the target (Figure 29). It should be noted that the NP diameter stops changing at distances closer to the exit orifice. The phenomenon supports the idea that part of the NPs grow in the trapping region to a larger size but become lost on the walls and on the target surface after reaching the critical size.

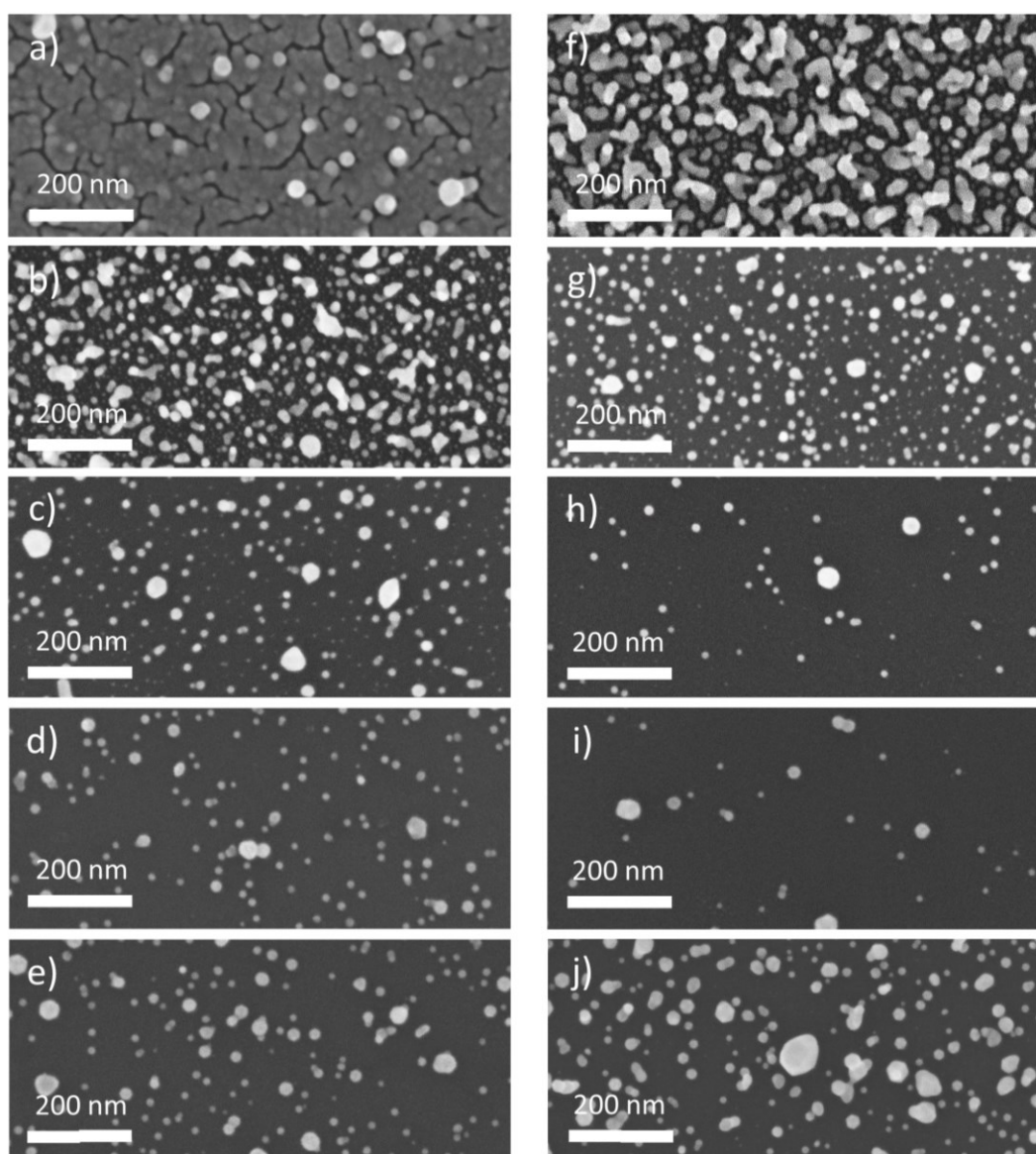


Figure 27. SEM images of Ag NPs deposited inside the GAS at different distances from the target in configuration with 2 substrates at every position (a, b – 2.0 cm top and bottom; c, d – 5.0 cm top and bottom; e, f – 7.5 cm top and bottom; g, h – 10.0 cm top and bottom; i – 11.5 cm top) and (j) axial distribution of the average NP size.

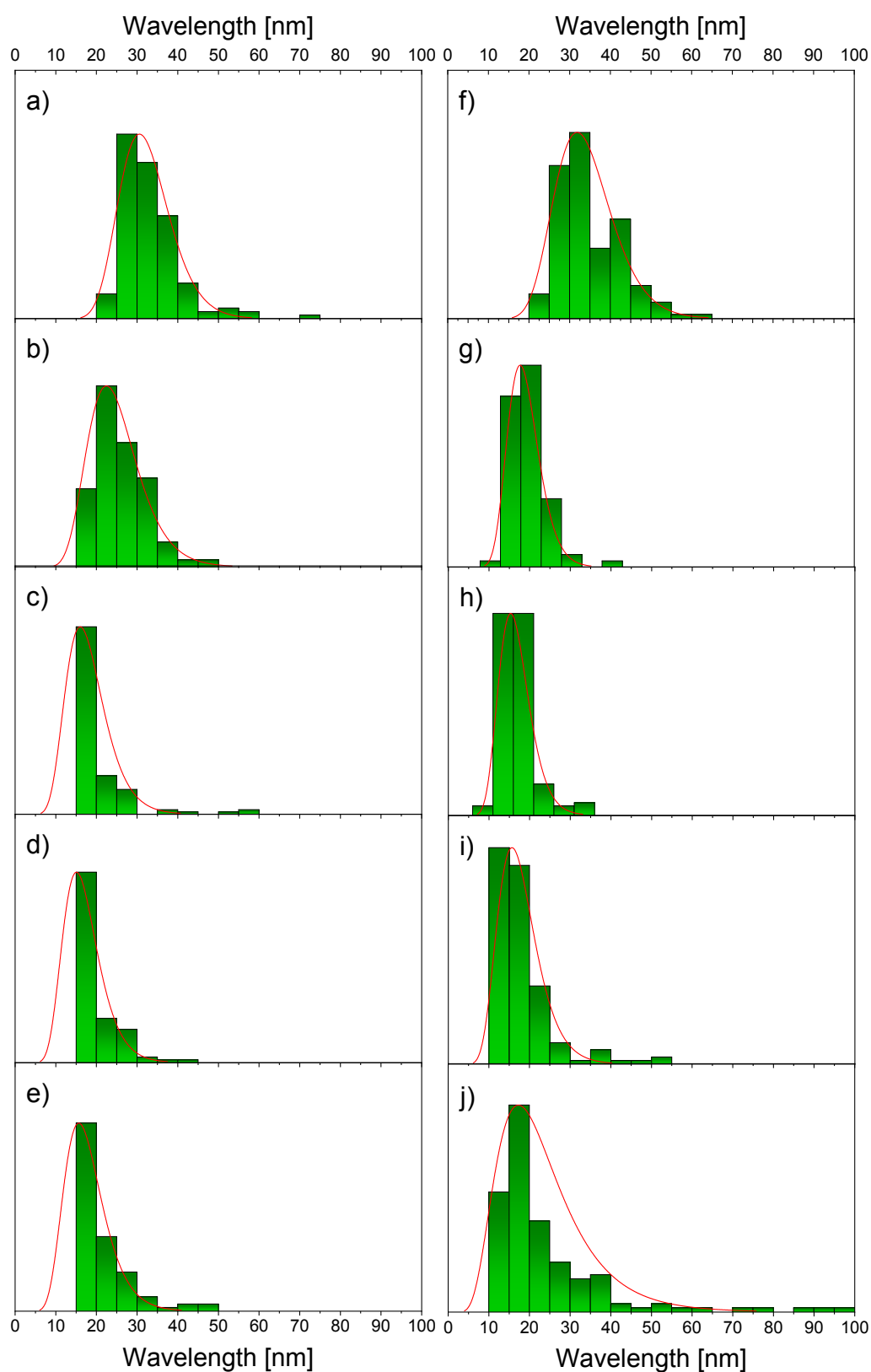


Figure 28. NP size distributions calculated for the samples placed at different distances from the target: a) – 2.0 cm, b) – 5.0 cm, c) – 7.5 cm, d) – 10.0 cm and e) – 11.5 cm, respectively, and f) – 20.0 cm behind the orifice.

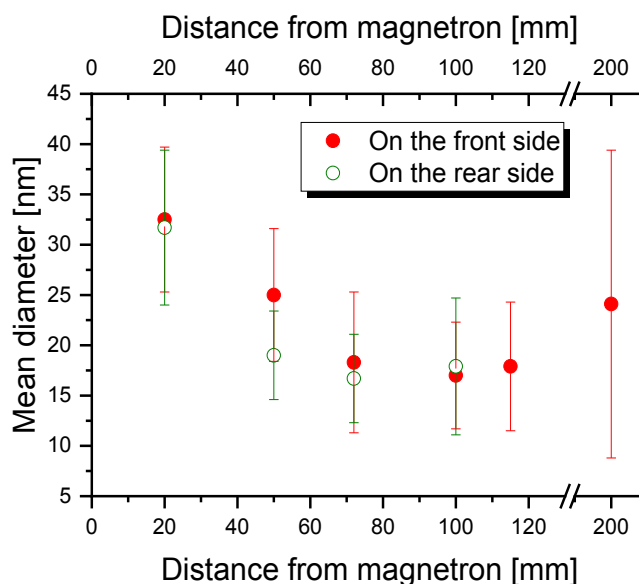


Figure 29. The dependence of the mean diameter on the distance from the magnetron.

It can be concluded that the deposition of NPs inside the aggregation chamber gives useful information about the real NP size and morphology. It was confirmed that big NPs with diameter up to 100 nm exist inside the GAS and after the discharge shutdown they are lost onto the target and walls. In its turn, small NPs are swept from the aggregation chamber by Ar stream. The falling dependency of NP average size on the distance from the target obtained by SAXS was confirmed.

3.2. Preparation of composite thin films for bio-applications

3.2.1. Deposition of Cu NPs/PEO nanocomposites

In the beginning of the previous chapter, we successfully characterized silver and copper NPs deposited under the chosen conditions. Spherical clusters with mean diameters of 22 nm and 25 nm, respectively, exhibited optical properties and chemical composition typical for metallic Ag and Cu (see Figure 13-15). Therefore, both should provide strong bactericidal effect, which arises from the Ag^+ and Cu^{2+} ion release. However, using of as-deposited NPs is limited by two main factors: poor adhesion of NPs to the surfaces and their significant toxicity in relation to the living organism. The incorporation of NPs into biocompatible polymer matrix may help to overcome these disadvantages. The polymer will keep NPs fixed on the surface to avoid their contact with the organism. Moreover, it will regulate the metal ion release. According to the

literature, PEO plasma polymer (ppPEO) thin films deposited by Plasma Assisted Vapor Phase Deposition are promising for biological applications because of biocompatibility, good stability in aqueous media and especially non-fouling activity, i.e. the resistance to biomolecule adsorption.[28, 104] The combination of PEO with antibacterial NPs will allow to obtain multi-functional coatings for medical devices, which are able to kill bacteria and to withstand the biofilm formation. It is known that the presence of the ether groups in the plasma polymer and the mobility of molecular segments are two main factors responsible for the non-fouling properties of PEO.

The nanocomposite coatings were produced by the sequential deposition of a 100 nm layer of ppPEO, a monolayer of Cu NPs and a 10 nm capping layer of ppPEO. Figure 30 shows the SEM images measured on the top side of the nanocomposite and on the cross-section. The majority of clusters are successfully incorporated into the PEO matrix. The bottom 100 nm layer of ppPEO was pre-deposited to enhance the adhesion of NPs to the substrate and to decrease the risk of film delamination during the sample splitting.

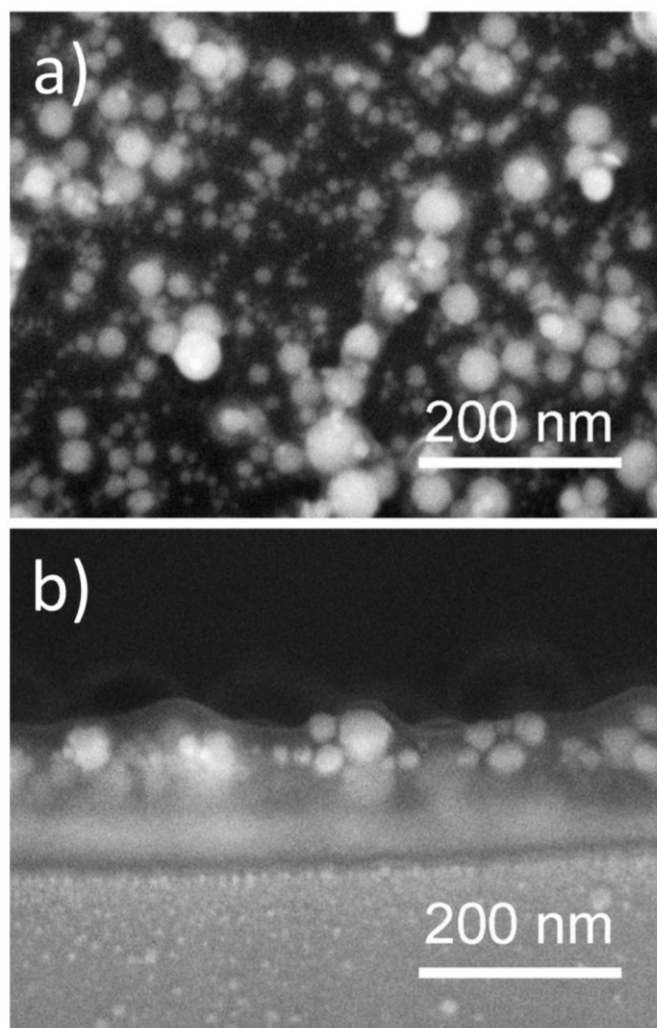


Figure 30. (a) Top side image and (b) cross-sectional SEM image of the nanocomposite film prepared by the sequential deposition of a 100 nm layer of ppPEO, a mono-layer of Cu NPs and a 10 nm capping layer of ppPEO.

The chemical composition of the nanocomposite film was studied by XPS with and without breaking vacuum. The ppPEO film 110 nm thick without NPs was measured as a control. The high resolution spectrum of C 1s peak is shown in Figure 31a. The predominant signal of the ether bonds is situated at 286.5 eV. Moreover, smaller contribution from aliphatic hydrocarbons (285.0 eV), the carbonyl- (288.0 eV) and the carboxyl-based (289 eV) functional groups was also detected. The detailed analysis of the spectrum revealed the content of the C-O-C groups of 83 at. % in the plasma polymer, which characterizes a good retention of the original PEO structure.[27, 28] The results of the evaluation of the chemical composition are presented in Table 2. The significant differences were found in the C 1s spectrum acquired for the nanocomposite consisted of a monolayer of Cu NPs covered by 10 nm

of ppPEO (see Figure 31b). The obvious increase of the peak corresponding to aliphatic hydrocarbons was detected. At the same time, a slight increase of the carboxyl and carbonyl components was also found. All these transformations led to the reduction of the C-O-C concentration almost twofold to 45 at. %. Such behaviour may be critical for the retention of the non-fouling properties of ppPEO, which hold only if the concentration of the ether groups is $> 70\%$. Additionally, the high resolution spectrum of the Cu 2p peak was acquired (Figure 31c). The presence of shake-up satellites corresponding to CuO was revealed.[105, 106]

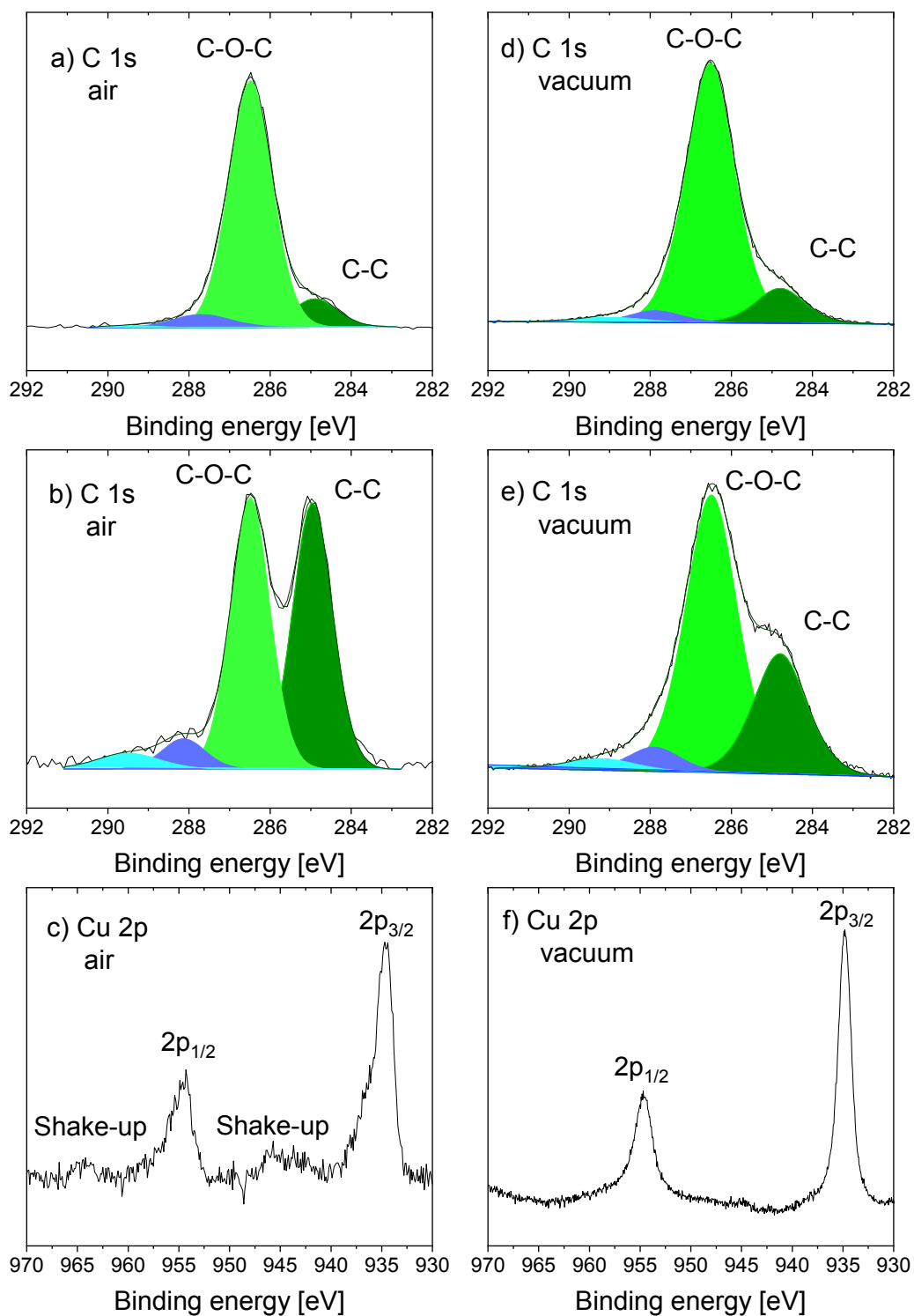


Figure 31. High-resolution XPS spectra taken after transferring the samples for the analysis in air (left column) or without breaking vacuum (right column): a) d) C1s for the ppPEO without NPs; b) e) C1s for Cu NPs overcoated by the 10 nm ppPEO capping layer; c) f) Cu2p for Cu NPs overcoated by the 10 nm ppPEO capping layer.

Table 2. Chemical composition of ppPEO as obtained from fitting of the C1s XPS spectra.

Sample	C-C/C-H, at. %	C-O-C, at. %	C=O, at. %	O-C=O, at. %
After contact with air				
ppPEO	10	83	6	1
Cu NPs/ppPEO	45	45	6	4
Without breaking vacuum				
ppPEO	11	83	4	2
Cu NPs/ppPEO	28	63	5	4

It should be noted that the spectra in Figure 31 a-c were recorded after the 2 week storage of the samples under the ambient conditions. To preserve the films from the influence of atmosphere and to avoid aging effect on chemical composition of the samples they were transferred to XPS set-up under vacuum immediately after the preparation. The spectra acquired on these films are shown in Figure 31 d-f. The C 1s spectrum of ppPEO looks almost the same as the one acquired after the 2 week storage (compare Figure 31a and d). However, the spectrum of the nanocomposite film is different. The retention of the C-O-C groups is better in comparison with the aged sample (Figure 31e). It is interesting to see the absence of the shake-up satellites in the Cu 2p spectrum (Figure 31f). Therefore, partial oxidation of Cu NPs most likely occurs after their contact with air. It can be concluded that the changes of the chemical composition of ppPEO were induced by the action of Cu NPs. They catalyze the transformation of the ethers into other chemical groups, e.g. aliphatic hydrocarbons and carboxyl groups, near the particle – polymer interface. In the literature, such modified layers in contact with rigid surfaces are named adsorbed layers. The thickness of adsorbed layer is < 10 nm (penetration depth of XPS ~ 6-8 nm). However, the chemical mechanism of this process is still not clear. The changes of the ppPEO chemical composition are critical in terms of non-fouling properties. It was earlier revealed in [28] that non-fouling action of ppPEO depends on the retention of C-O-C groups, therefore in such metal NPs – ppPEO nanocomposites biomolecule adsorption could be expected.

Another important factor that influences the non-fouling properties is the segmental dynamics. It is known that mobility of macromolecular chains in

conventional PEO is high to allow them acting as macromolecular springs. If macromolecular mobility is confined, biomolecules have higher probability to adhere to the polymer surface. Such effect was observed, for example, when thin film of ppPEO was deposited onto rigid Si substrate.[31] In that case, the segmental mobility in thin polymer films was studied by means of specific heat spectroscopy in AC-chip calorimetry mode. It is known that dynamic T_g is directly related to the segmental mobility in polymers. Therefore, a decrease of segmental mobility results in an increase of dynamic T_g . Here, Cu NPs can play the role of confinement-forming units. To investigate the influence of NPs on segmental dynamics of PEO plasma polymer the multilayered nanocomposite films with different PEO thickness were deposited directly onto AC-chips without breaking vacuum. The bi-layered nanocomposite samples were prepared step by step, as follows:

- I. Deposition of a 5 nm film of ppPEO, as an underlying layer.
- II. Deposition of the first layer of Cu NPs with a particle flux of 250 NPs/ μm^2 .
- III. Deposition of the ppPEO interlayer over the first layer of Cu NPs. The thickness of the interlayer was varied between 10 nm and 100 nm.
- IV. Deposition of the second layer of Cu NPs with a particle flux of 250 NPs/ μm^2 .
- V. Deposition of a capping 10 nm ppPEO layer.

Schematic representation of these coatings is shown in Figure 32.

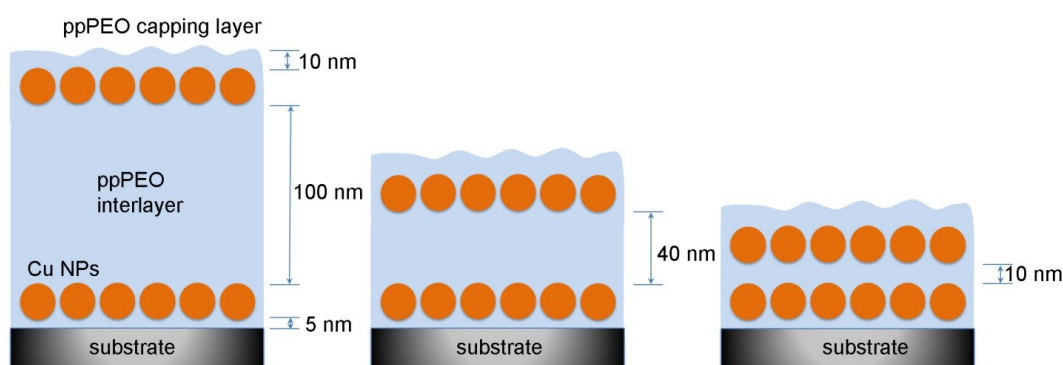


Figure 32. Cross-sectional representation of the bi-layered structure of the Cu/ppPEO nanocomposites with different thickness of the ppPEO interlayer.

TEM and SEM analysis was performed for the characterization of the multilayered samples. Two sub-monolayers of Cu NPs were separated by a ppPEO interlayer of 40 nm thickness for better resolution on TEM. The top-view image and

the corresponding NP size distribution are presented in Figure 33a. It is seen that Cu NPs are well-dispersed in the matrix. Unfortunately, it is impossible to distinguish between the individual layers of NPs when looked at from top. The average diameter determined from the corresponding histogram (see Figure 33b) fitted by lognormal distribution function was 16 ± 5 nm. This value is in good accordance with the mean diameter calculated by SEM image processing (22 ± 5 nm, see Figure 13c).

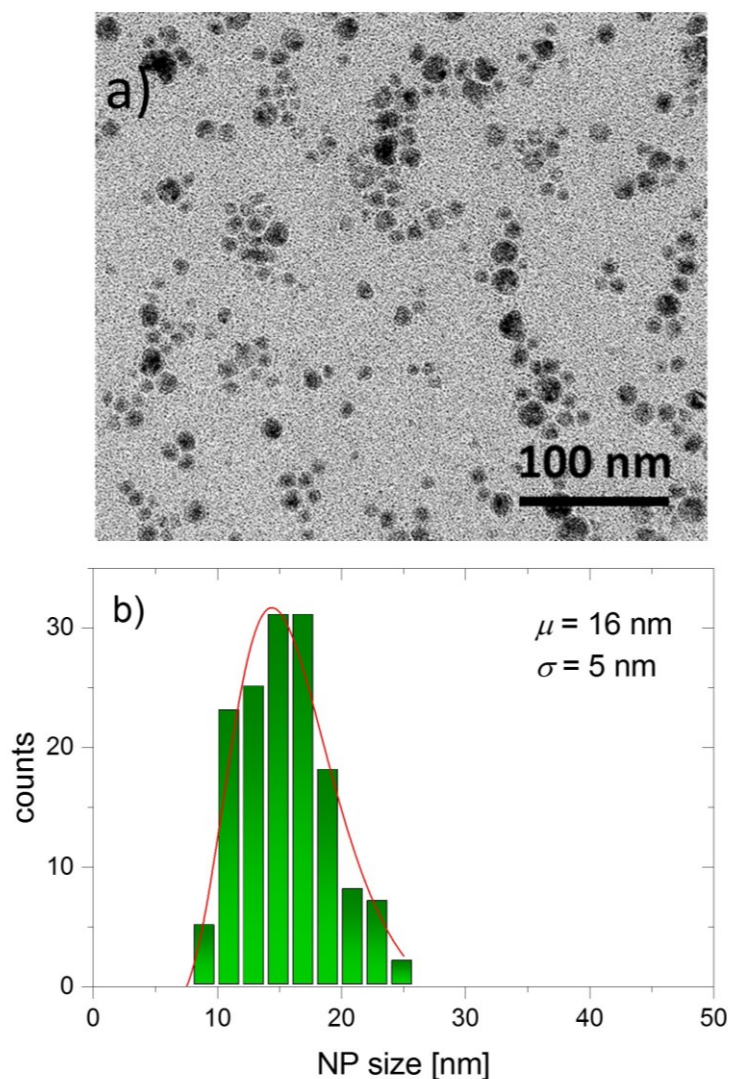


Figure 33. a) Top-view TEM image of two sub-monolayer of Cu NPs separated by the 40 nm ppPEO interlayer. b) Size distribution of the NPs.

SEM cross-sectional measurement was performed for the film with 100 nm of the ppPEO interlayer in order to characterize the internal structure of composite. The cross-section images were recorded both in the secondary electron mode (Figure 34a) and the backscattered electron mode (Figure 34b) for better imaging of NPs in bulk

polymer. Both micrographs successfully revealed the presence of 2 NP layers (bright) separated by the ppPEO interlayer (dark) as especially evident in the backscattered image. The layer thickness cannot be determined accurately from these images; however, it seems to be slightly less than 100 nm. As result, our deposition technique is applicable for the preparation of multilayered samples that can be used for the subsequent AC-chip calorimetry investigation.

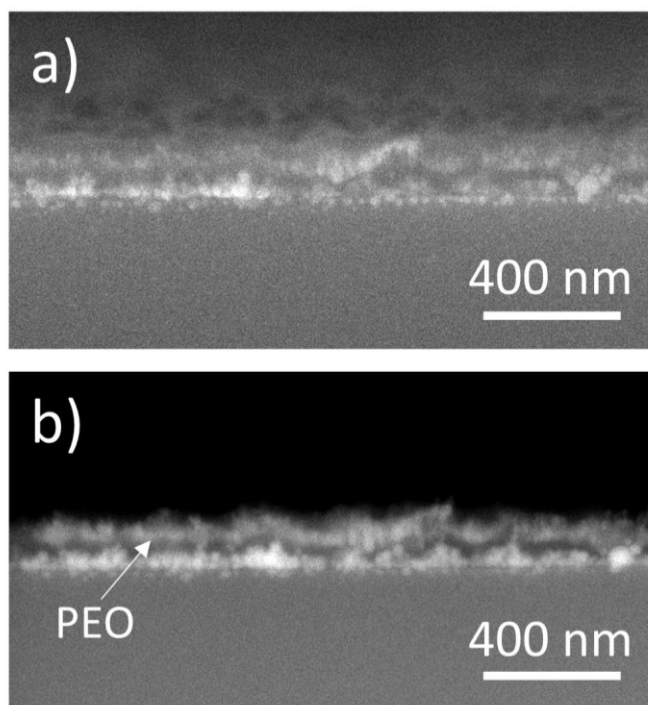


Figure 34. SEM cross-sectional images of the nanocomposite film consisting of two monolayers of Cu NPs separated by the 100 nm ppPEO interlayer acquired in (a) secondary electron and (b) backscattered electron modes.

3.2.2. The segmental dynamics of ppPEO in nanocomposites

The procedure of AC-chip calorimetry measurements was described in Chapter 2.2.2. It was utilized to determine the T_g^{dyn} from the peaks obtained by the first derivative of U_R with respect to temperature. A Gaussian was fitted to the peak and temperature of the peak maximum is taken as T_g^{dyn} . Calorimetric curves processed for bi-layered Cu NPs/ppPEO nanocomposite films of different thickness are shown in Figure 35. The thickness of ppPEO interlayer was varied from 100 to 10 nm. All the samples demonstrate the similar main peak corresponding to the dynamic glass transition temperature of ppPEO (see Figure 11). However, the less intensive shoulder appears in higher temperature region for the samples with the interlayer thickness of 70 nm

and below. Therefore, the curves were fitted by two Gaussian peaks to determine two values of T_g^{dyn} . The appearance of an additional dynamic glass transition temperature indicates the presence of the second polymer phase with significantly different properties that was earlier found by the XPS analysis. The ether-depleted layer in the vicinity of NPs exhibits different segmental dynamics in comparison with bulk ppPEO. The similar effects were recently described in the works considering the incorporation of Si particles into thin polymer films.[107, 108] It was revealed that in the case of thin polymer films with non-repulsive polymer/particle interactions an irreversibly adsorbed modified layer is expected to form close to the polymer/particle interface. Therefore, the formation of the modified ppPEO layer in the vicinity of Cu NPs can be expected during the nanocomposite deposition. The change of the segmental dynamics is indicated by the increase of T_g^{dyn} .

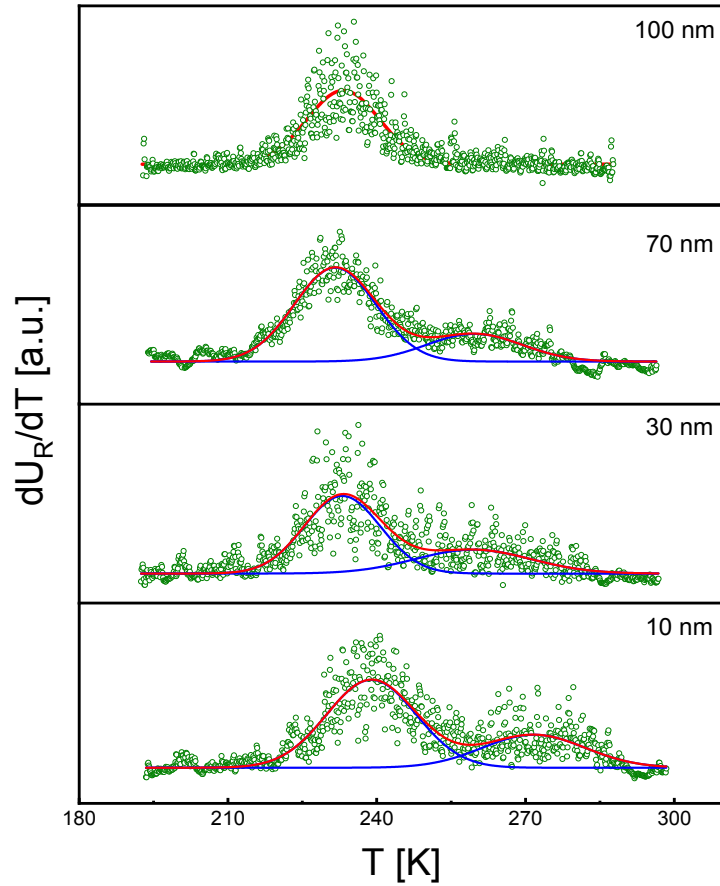


Figure 35. The first derivative of the real part of the complex differential voltage with respect to temperature for samples with interlayer thicknesses of 100, 70, 30, and 10 nm. The measuring frequency was 160 Hz.

The dependence of the relative peak area of the second component on the thickness of the interlayer is presented in Figure 36. The relative intensity demonstrates a distinct growth at thicknesses 70 nm and below, so the PEOpp/nanoparticle interactions become critical for the properties in very thin composite layers. Our observation is in good agreement with the results published previously for poly(vinyl methyl ether) PVME and PVME/polystyrene (PS) blend thin films studied by Broadband Dielectric Spectroscopy.[109, 110] These facts indicate that the second peak on the dynamic glass transition curves corresponds to the T_g^{dyn} of the modified PEOpp layer formed in the vicinity of Cu NPs. As a result, the polymer matrix consists of two phases with significantly different segmental dynamics.

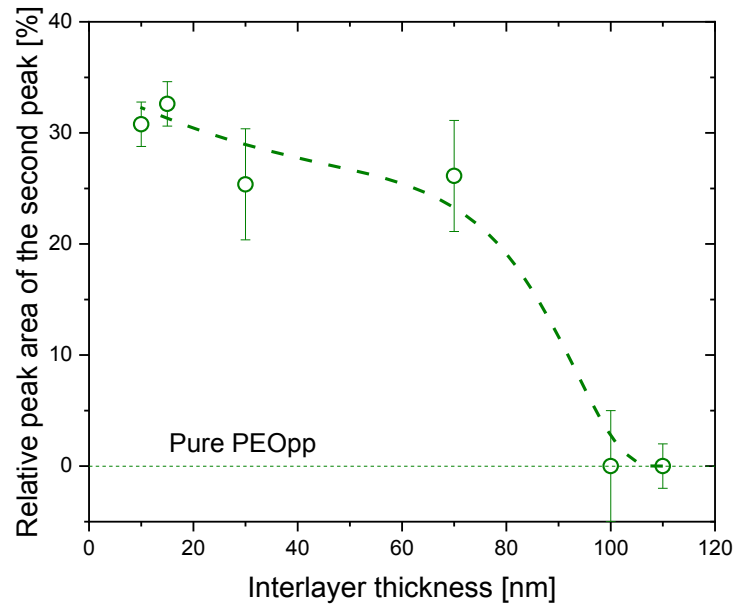


Figure 36. Relative peak intensity of the second peak given in percent versus thickness of the ppPEO interlayer. Typical error bars are given. The line is a guide to the eyes.

For more complete analysis of the segmental dynamics in the multi-layered nanocomposite films, T_g^{dyn} was determined in a full range of frequencies and the relaxation maps were constructed, which are shown in Figure 37. The temperature dependence of the relaxation rate f_p is curved when plotted versus $1/T$, as expected for a dynamic glass transition, which can be well described by the Vogel/Fulcher/Tammann- (VFT-) equation.[111–113]

$$\log f_p = \log f_\infty - (DT_0 * \ln(10))/(T - T_0) \quad (2)$$

Here, f_∞ is the relaxation rate at infinite temperature, T_0 is called the ideal glass transition or Vogel temperature, which is found to be 30-70 K below the thermal T_g . The parameter D is called the fragility parameter. It characterizes a quantity to classify glass-forming systems. Glass formers are classified as fragile when the temperature dependence of the relaxation rates is closer to the VFT dependence and strong when $f_p(T)$ is closer to the Arrhenius law. The fitting was done by keeping all parameters free.

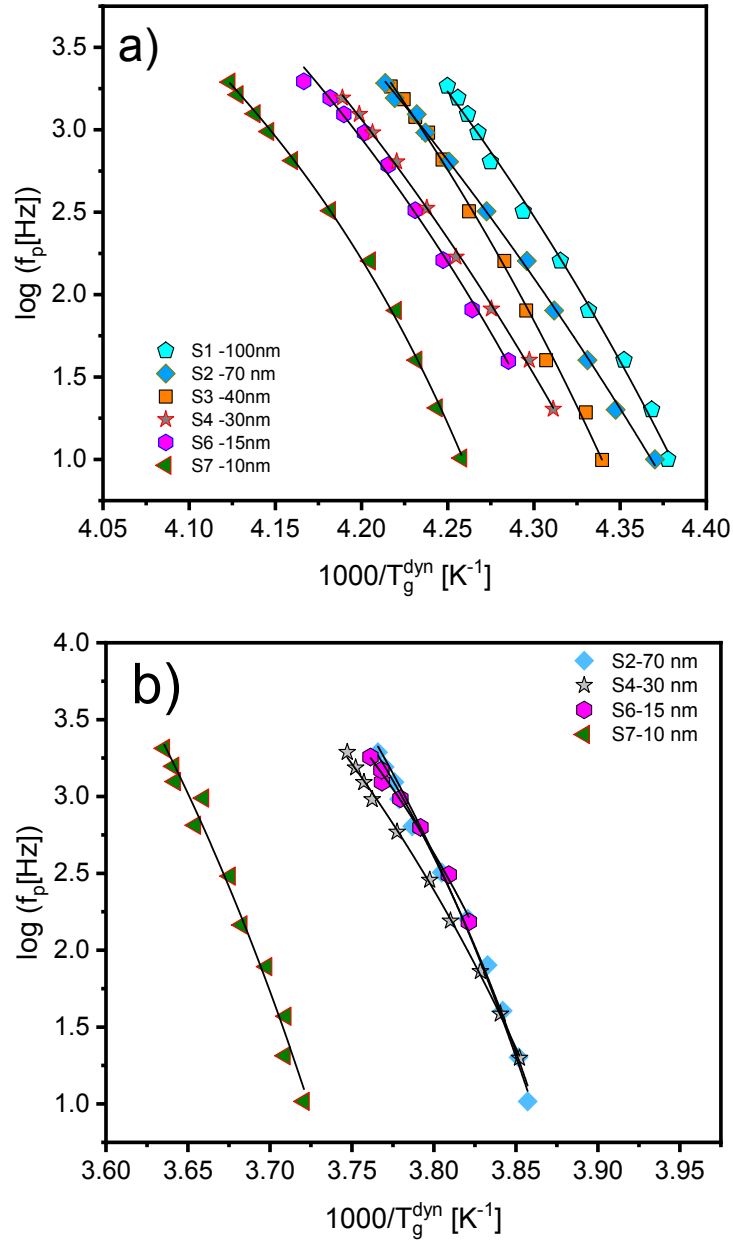


Figure 37. Relaxation rate f_p versus inverse temperature: (A) dynamic glass transition of the bulk-like ppPEO interlayer for the samples with different interlayer thickness: pentagons – 100 nm; diamonds – 70nm; squares – 40 nm; stars – 30nm; hexagons – 15nm; triangles – 10nm; (B) The second process for the modified ppPEO layer at the Cu NPs/ppPEO interface: squares – 70nm; downside triangles – 30nm, circles – 15nm, triangles – 10nm. Solid lines are fits of the VFT equation to the corresponding data.

The T_g^{dyn} of both bulk-like ppPEO and modified layer estimated from the measurements at frequency 160 Hz are shown in Figure 38a. The significant difference between these values is seen for all the samples. The T_g^{dyn} corresponding to the

modified ppPEO exceeds the T_g^{dyn} of bulk-like ppPEO by ~ 30 K that indicates the presence of constraints in the mobility of macromolecular chains in the vicinity of Cu NPs. At the same time, the gradual growth of the T_g^{dyn} of bulk-like ppPEO by ca. 8 K was found with the decrease of interlayer thickness. Noteworthy, the T_g^{dyn} of modified ppPEO remains constant until the critical thickness of interlayer is achieved. It should be noted that the observed changes are much larger than the experimental error. An abrupt increase of the T_g^{dyn} of modified PEOpp was revealed at thickness of ppPEO interlayer 10 nm which can be explained by the critical state which influenced the behavior of macromolecular segments in the adsorbed layer. Overall, it can be concluded that the thickness of modified layer is less than the average size of Cu NPs.

It was interesting to see that the additional parameters determined from the VFT-equation also depend on the interlayer thickness. Figure 38b indicates the systematical growth of the ideal glass transition temperature or Vogel temperature T_0 with the decreasing interlayer thickness. It is worth noting that this dependence is more obvious than the one obtained for the T_g^{dyn} . The temperature shifts by ca. 45 K. The same behaviour was earlier demonstrated for thin films of conventional polymers.[114, 115] Another parameter determined from VFT-equation is the fragility D . Contrary to T_g^{dyn} and T_0 , it decreases with decreasing interlayer thickness as shown in Figure 38c. This effect corresponds to the change of the glassy dynamics from a stronger to a fragile behavior. A similar behavior was observed for thin films of a homopolymer by dielectric spectroscopy.[114]

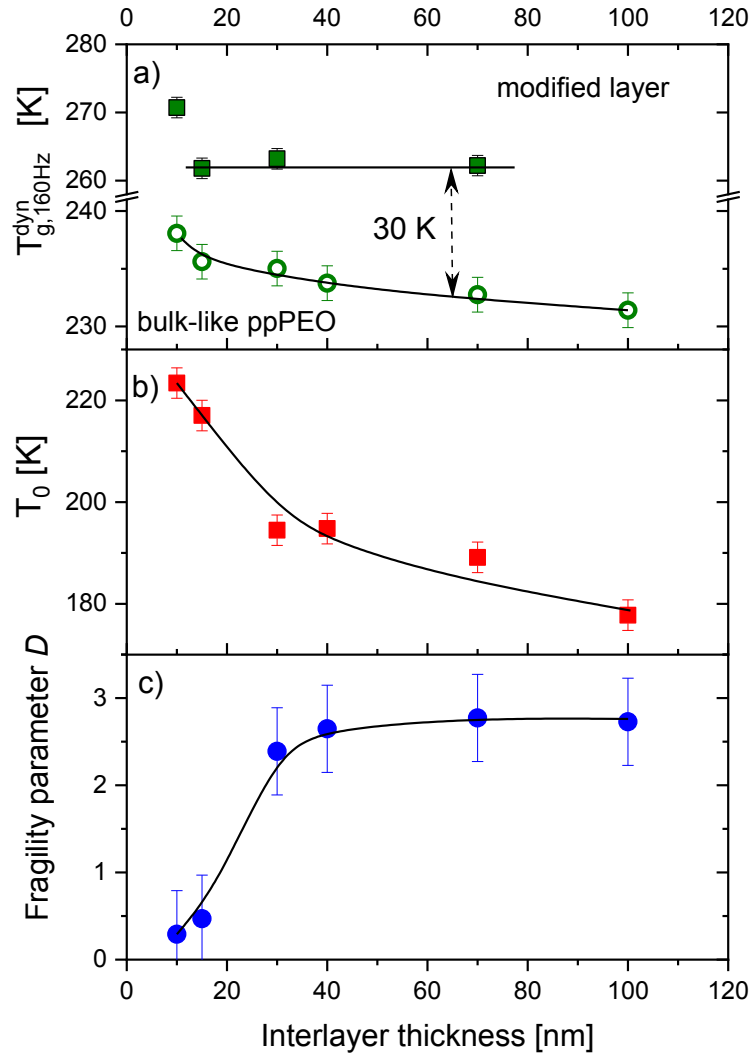


Figure 38. (a) Dynamic T_g measured for the bulk and modified ppPEO at 160 Hz versus interlayer thickness. (b) T_0 versus interlayer thickness. (c) Fragility parameter D as a function of interlayer thickness. Lines are guides to the eyes.

3.3.3. Biological activity of metal – polymer nanocomposites

As was demonstrated previously, thin films of PEO plasma polymer exhibit the resistance against the adsorption of different proteins from their solutions.[28, 104] However, it was shown that the non-fouling effectiveness depends on the cross-link density related with the segmental mobility of macromolecules in plasma polymer. The transition between fouling and non-fouling modes of ppPEO occurs at the cross-link density corresponding to $T_g^{\text{dyn}}_{160\text{Hz}} < 249\text{ K}$. [31] This value characterizes the film with the concentration of the ether groups around 65 at. %. This finding might be

significant for the production of nanocomposite materials for biomedical applications based on ppPEO matrix.

In our case, two types of nanocomposites with similar structure (5 nm of ppPEO – 2 layers of Ag or Cu NPs – 10 nm of ppPEO) were prepared and the adsorption of BSA was studied. The XPS measurement of the nitrogen content was used for the control of the protein adsorption. Neither ppPEO nor metal NPs contain nitrogen; therefore, the presence of the N 1s signal in XPS after the protein incubation and water rinsing indicates the protein binding. The concentration of nitrogen on the surface of the samples after their incubation in BSA solutions is presented in Table 3. PpPEO film of 15 nm thickness and bare metal NPs were used as positive and negative controls, respectively. As was expected, the XPS spectrum of ppPEO exhibited the absence of nitrogen and proved the non-fouling behaviour of the plasma polymer. An opposite situation was observed in the case of Ag NPs and Cu NPs where 8.7 at. % and 5.5 at. % of nitrogen was found. These values correspond to a complete coverage of the surface with a protein layer.[116, 117] The Ag NPs/ppPEO and Cu NPs/ppPEO composites showed an intermediate value of 2.1 and 1.7 at. % of nitrogen, respectively. These results demonstrate that the inclusion of metal NPs into the matrix of ppPEO deteriorates the non-fouling properties of plasma polymer, although it reduces the protein adsorption in comparison with bare NPs.

Table 3. Nitrogen content on the surface of different samples after their incubation in a 50 µg/ml BSA solution.

Sample	N, at. %
ppPEO films, 10 – 100 nm	0
Ag NPs	8.7
Ag NPs + ppPEO film, 10 nm	2.1
Cu NPs	5.5
Cu NPs + ppPEO film, 10 nm	1.7

The results of the protein adsorption tests correlate with previous finding of two different polymer phases, characterized by two different T_g^{dyn} , in the Cu NPs/ppPEO nanocomposites. We assume that the first T_g^{dyn} characterizes the bulk ppPEO and the second T_g^{dyn} corresponds to the modified layer of ppPEO with reduced mobility of macromolecular chains. For example, in the case of multilayered nanocomposite with 10 nm of the ppPEO interlayer (see Figure 38a) the glass transition temperature for the bulk phase was found to be $T_{g^{dyn}}^{160\text{ Hz}} = 238\text{ K}$. This value is lower than 249 K at which ppPEO demonstrates non-fouling behavior. At the same time, the $T_{g^{dyn}}^{160\text{ Hz}}$ of the modified layer is about 270 K and this layer constitutes about 30 % of the entire polymer phase as was shown in Figure 36. It has been determined previously that the concentration of the C-O-C groups on the surface of Cu NPs/ppPEO composite film was significantly lower than critical 65 at. % (Table 2). Thus, the deterioration of the non-fouling properties of ppPEO in metal NPs based thin composite films can be explained by the formation of the modified ppPEO layer in the vicinity of NPs, which is characterized both by the ether-deficient chemical composition and by the constrained segmental mobility.

The problems of the chemical changes and constrained macromolecular dynamics in the modified ppPEO layer can be overcome by the increase of the thickness of the ppPEO capping layer. However, such approach will influence the other functionalities of the nanocomposite, such as the antibacterial properties. Antibacterial action of Ag and Cu NPs in aqueous media is associated with the release of metal ions. Therefore, for the efficient functionality of the composite the capping ppPEO layer in the composite must allow for the inward penetration of water and outward release of metal ions. At the same time, it should prevent the NPs from escaping into the solution and exhibit the non-fouling properties. The fixation of NPs on the surface and the non-fouling action need thicker ppPEO capping layer. However, its enhancement significantly slows down the ion release. In our case, the capping layer of 10 nm thickness seems to be a compromise.

The antibacterial tests of copper-based nanocomposite were carried out against 2 dangerous multidrug resistant strains: gram-positive *Methicillin-resistant Staphylococcus aureus* (MRSA) and gram-negative *Pseudomonas aeruginosa*. In the case of MRSA, the bacterial suspension test showed a 1 log increase of the initial bacterial concentration for the control samples of glass and ppPEO (without Cu NPs, Figure 39). For the 2 layers of Cu NPs overcoated with 10 nm of the ppPEO capping

layer, a 63 % decrease of the initial bacteria concentration was detected. The fact that the capping layer introduces an additional barrier to the molecular diffusion becomes evident from the comparison of this sample with 2 layers of bare Cu NPs uncovered by ppPEO. In the latter case, a stronger 70 % decrease of the initial bacterial concentration was achieved. In both cases, the bactericidal activity falls far from the typically required several log reduction, the shortcoming evidently related with the small amount of copper present on the surface or in the coatings. Nevertheless, the detected decrease of the bacterial concentration allows designating the coatings as having at least the bacteriostatic effect. The bactericidal activity is anticipated to become stronger if a larger amount of Cu NPs is used, similar to the recent findings with other types of the nanocomposites and bacteria.[118, 119]

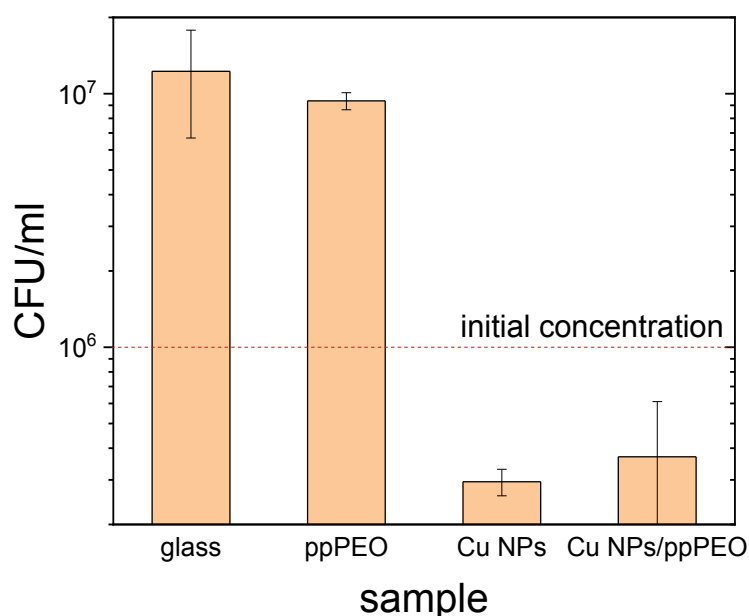


Figure 39. The concentration of *S. aureus* (MRSA) after the 3-h incubation with the Cu NPs/ppPEO composite films (2 layers of Cu NPs overcoated by 10 nm of ppPEO). Blank glass, 2 layers of Cu NPs without ppPEO and 10 nm ppPEO film without Cu NPs are used as controls.

It is well-known that bacteria rarely live as individual organisms neither in an environment, nor in a host body. Usually, bacteria form surface-attached 3D structures known as biofilms where microorganisms are embedded in extracellular protein matrix. Bacteria in biofilms are highly resistant to external stresses, including

antimicrobial treatments of any kind.[120] Development of materials with non-adhesive properties to prevent bacterial colonization or having bactericidal effect is a field of high interest. To study whether the Cu NPs/ppPEO films have a bacteriostatic effect due to the release of Cu or to the prevention of biofilm formation, we used the *P.aeruginosa* strain 21, which is characterized by a high ability to form biofilms and by multi-drug resistance. The bacteria were found alive on the surface of the control glass and ppPEO without Cu NPs (Figure 40). In contrast, almost all bacteria in biofilms formed on Cu-containing samples were found dead. These results proved the efficiency of Cu in killing multi-drug resistant bacteria even in biofilms. Nevertheless, the non-fouling properties were not achieved as significant amount of the bacteria (either dead or alive) were found present on all kinds of the surfaces. Apparently, the same reasoning can be suggested here: restrained macromolecular mobility and/or chemical changes in the capping ppPEO layer are the factors that prevent the surface from exhibiting the non-fouling properties against bacteria. Furthermore, the weak bactericidal effect of Cu NPs/ppPEO composite films, which was observed for the individual bacteria, could be also contributed by the biofilm formation that hindered the delivery of Cu ions to the liquid phase of the bacterial medium. These findings highlight the fundamental importance of unveiling the structure-chemistry-property relationship in metal/polymer nanocomposites, especially if catalytic transition metals are considered and ultra-thin coatings are to be used.

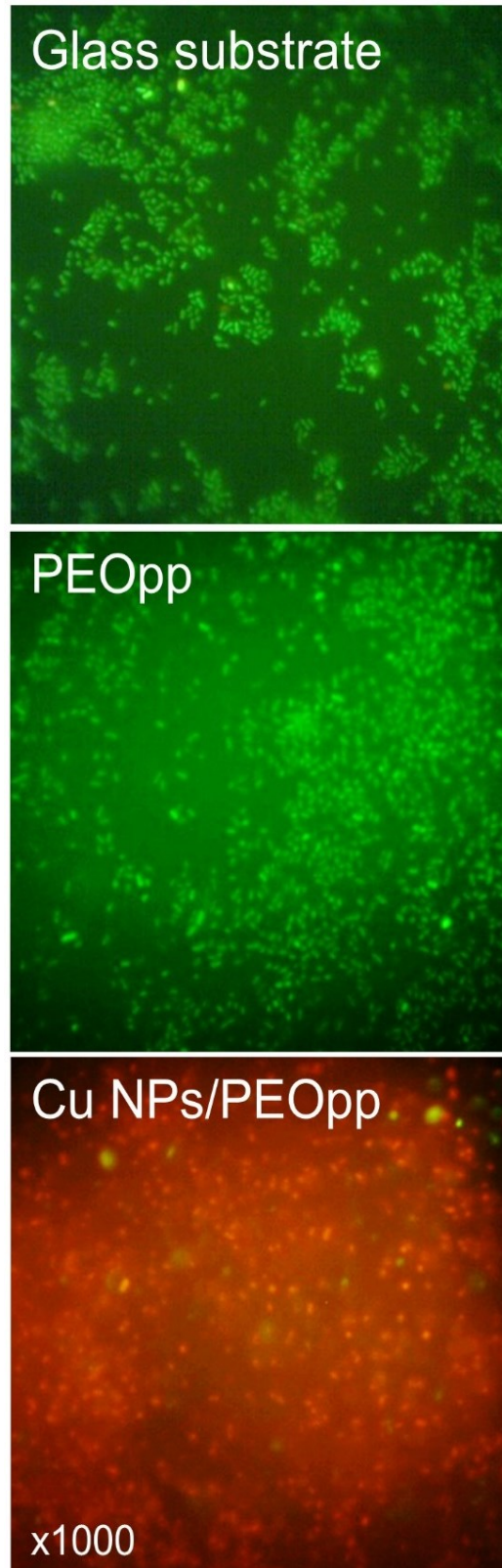


Figure 40. The fluorescent microscopy images of the control glass substrate, 10 nm ppPEO film and Cu NPs/ppPEO composite film (2 layers of Cu NPs overcoated by 10 nm of ppPEO) after 24 hours incubation with *P. aeruginosa* 21. Green – alive bacteria, red – dead bacteria.

3.3. Decoration of polymeric nanostructures by Cu NPs

3.3.1. The deposition of polystyrene nanoislands

The PS-like material was created by Vapor Phase Deposition without plasma as previously described in Section 2.1. For the investigation of chemical composition of the resulted coating, the FTIR spectroscopy was measured in the Attenuated Total Reflection mode. The final spectrum presented in Figure 41 demonstrates all the peaks typical for the conventional PS. Bands at 3082, 3059 and 3026 cm^{-1} correspond to the aromatic C–H stretching, while the bands between 2925 and 2850 cm^{-1} characterize the aliphatic stretching vibrations. The bands at 1600 and 1493 cm^{-1} can be related to the aromatic C=C vibrations, which confirms the retention of aromatic rings in the deposited material. The bands at 1451 and 1372 cm^{-1} correspond to the C–H bending vibrations in methyl groups and the bands at 757 and 697 cm^{-1} are associated with aromatic out of plane vibrations. The analysis revealed that the chemical composition of the coating produced by Vapor Phase Deposition of PS is similar to the composition of the original polymer.

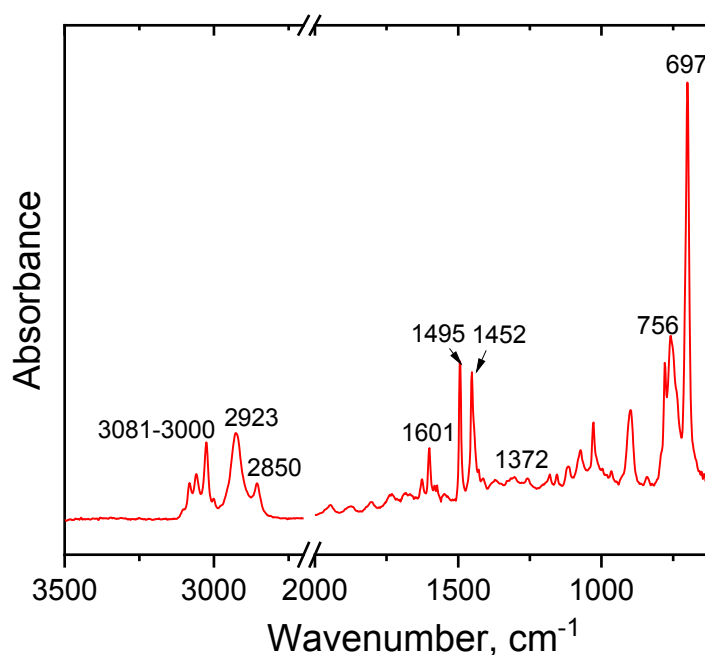


Figure 41. FTIR spectrum of the coating prepared by Vapor Phase Deposition of PS.

As was published previously, vacuum thermal degradation proceed with the cleavage of macromolecular chains. As a result, the deposited coating consists of oligomers. In this work, gel permeation chromatography (GPC) was applied to determine the molar mass distributions of the precursor and the deposited coating.

Figure 42a demonstrates the molar mass distributions of the precursor and deposited coating obtained using a column with pore size 10000 Å. An original PS demonstrates a relatively wide molar mass distribution with the maximum around 200000 g/mol, which is in good agreement with 192000 g/mol declared by the manufacturer. In contrast, the PS-like coating does not have high molar mass fragments in the structure. The distribution maximum is shifted toward the values < 20000 g/mol. Other GPC measurements were performed using the column with smaller pore size of 1000 Å (corresponding to the molar mass range 100 – 50 000 g/mol). They demonstrate the distribution with 2 evident maxima situated at 230 g/mol and 442 g/mol (see Figure 42b), and indicate the presence of low molar mass fragments in the PS-like coating.

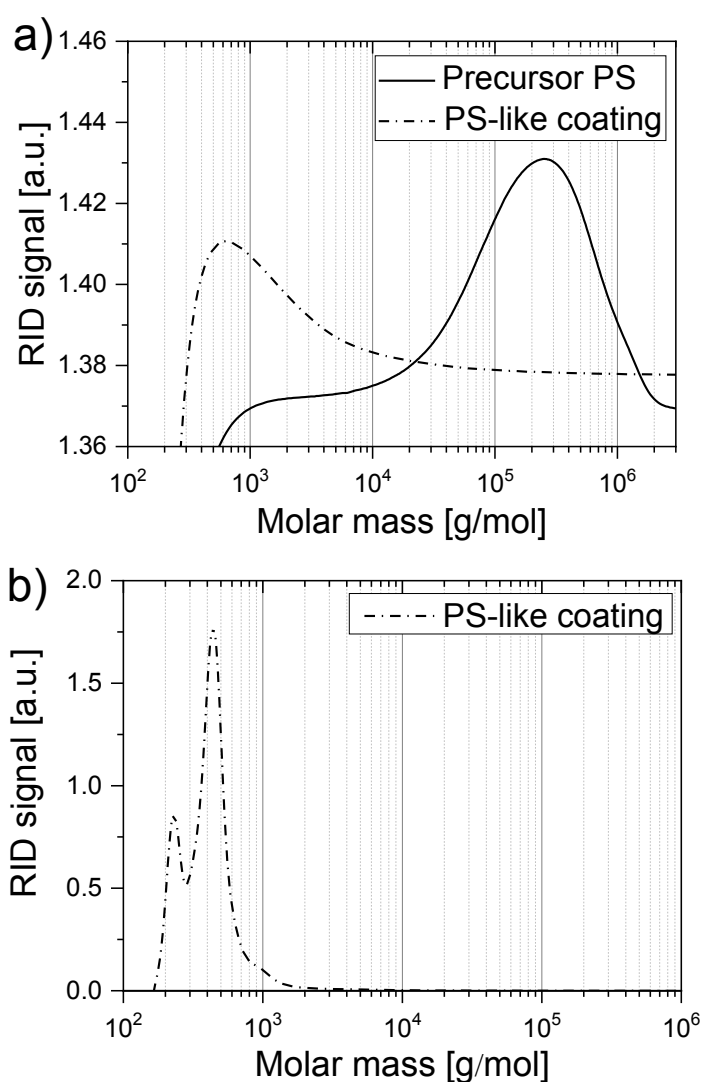


Figure 42. Distributions of molar mass of the PS precursor and the film deposited by Vapor Phase Deposition on Si as determined by GPC: (a) the column with pore size 10000 Å and (b) the column with pore size 100 Å.

The existence of low molar mass fractions in the PS-like coating was confirmed by NMR spectroscopy as well. The NMR spectrum of the precursor is shown in Figure 43a and it reveals the presence of the peaks corresponding to the CH chemical bonds in PS molecule. Many sharp and narrow peaks appear in the spectrum of the PS-like coating (Figure 43b). These peaks indicate the existence of a variety of low molecular mass fragments in the polymer structure. The peak at 0.9 ppm might correspond to the CH₃ terminal groups. Moreover, it can be explained by highly branched structure of the PS-like coating. The calculated molar ratio of conventional units vs. branched or low molecular mass units is 1:0.8. It can be concluded that Vapor Phase Deposition of the conventional PS results in the formation of PS-like coating on the substrate surface with the chemical composition being similar to the initial polystyrene; however, with smaller molar masses.

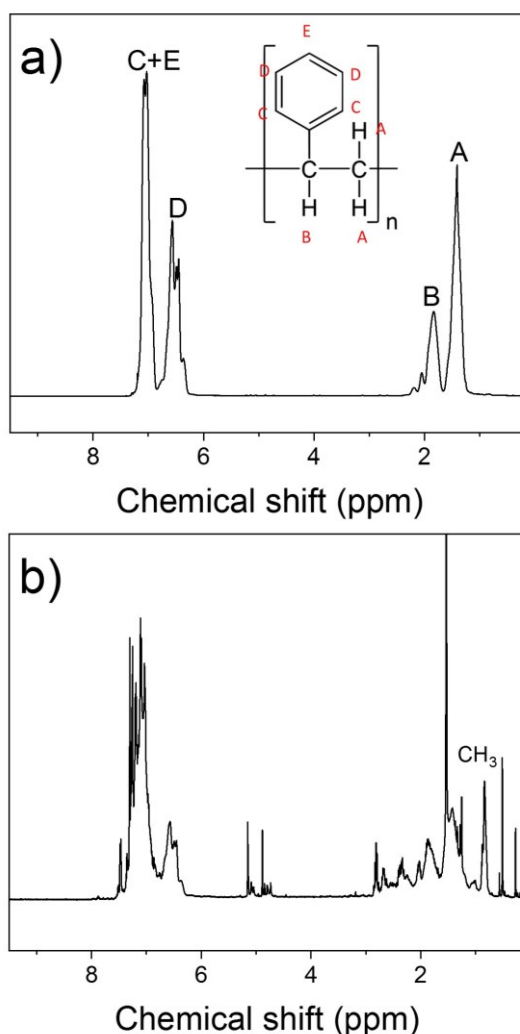


Figure 43. Liquid state ¹H NMR spectra of (a) the precursor polystyrene and (b) the film produced by Vapor Phase Deposition on Si.

The morphology of the PS-like coatings was studied by AFM. It was found that PS forms nanoislands on Si substrates. The image of the nanoislands prepared at the deposition rate of 20 Hz/min and the deposition time of 5 min is shown in Figure 44. The nanoislands have a semispherical shape. The surface of the islands is smooth and without any visible pattern. The mean island height calculated from the AFM images is 70 ± 10 nm whereas the mean island area is $0.75 \pm 0.2 \mu\text{m}^2$. It is worth noting that PS-like islands cover just $\sim 23\%$ of the substrate under chosen experimental parameters. The similar semispherical islands were previously observed as a result of plasma polymerization of PS and vacuum evaporation of poly(α -methylstyrene).[121–123] However, the mechanism of spherical nanoisland formation is still not clear.

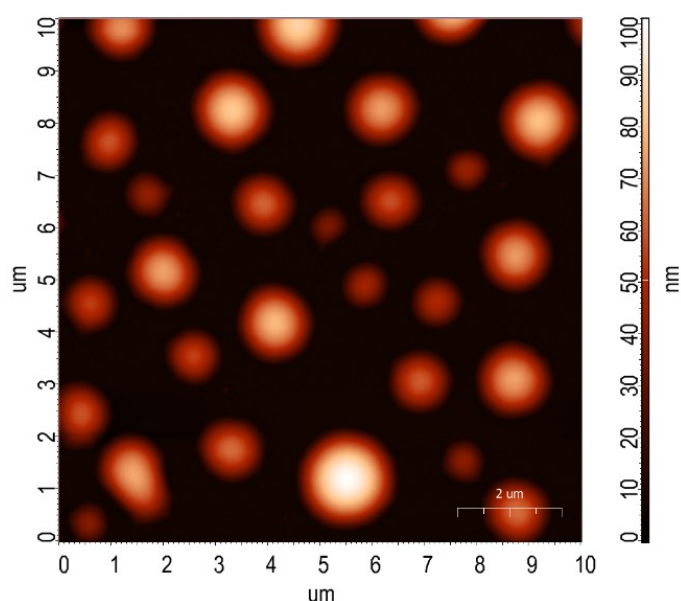


Figure 44. AFM micrograph of PS-like nanoislands. Deposition rate – 20 Hz/min.
Deposition time – 5 min.

3.3.2. The decoration of ppPEO film and PS nanoislands by Cu NPs

Bare Si substrates, Si substrates covered with 50 nm ppPEO films and with PS-like nanoislands were installed onto the substrate holder. Cu NPs were deposited in top to down configuration as was described in Chapter 2.1. The deposition time was chosen as 5 s and 30 s to obtain substantially different coverage. The resulting surfaces were first characterized by SEM. The micrographs of bare Si and Si with PEOpp presented in Figure 45a), b), d) and e), and demonstrate relatively homogeneous distribution of the NPs over the surface. Surprisingly, the NPs were found in a notably higher amount on PEOpp than on bare Si. This effect can be assigned to the different interaction of

NPs with bare Si and PEOpp. It can be assumed that NPs migrate over the surface after contact with Si or they can be repelled. On the other hand, the Cu NPs become more effectively stuck when deposited onto soft plasma polymer film. This hypothesis is supported by SEM images captured on PS-like nanoislands shown in Figure 45c), f). It is clearly seen that NPs are primarily located on the nanoislands and fewer amount of them can be observed on Si in between.

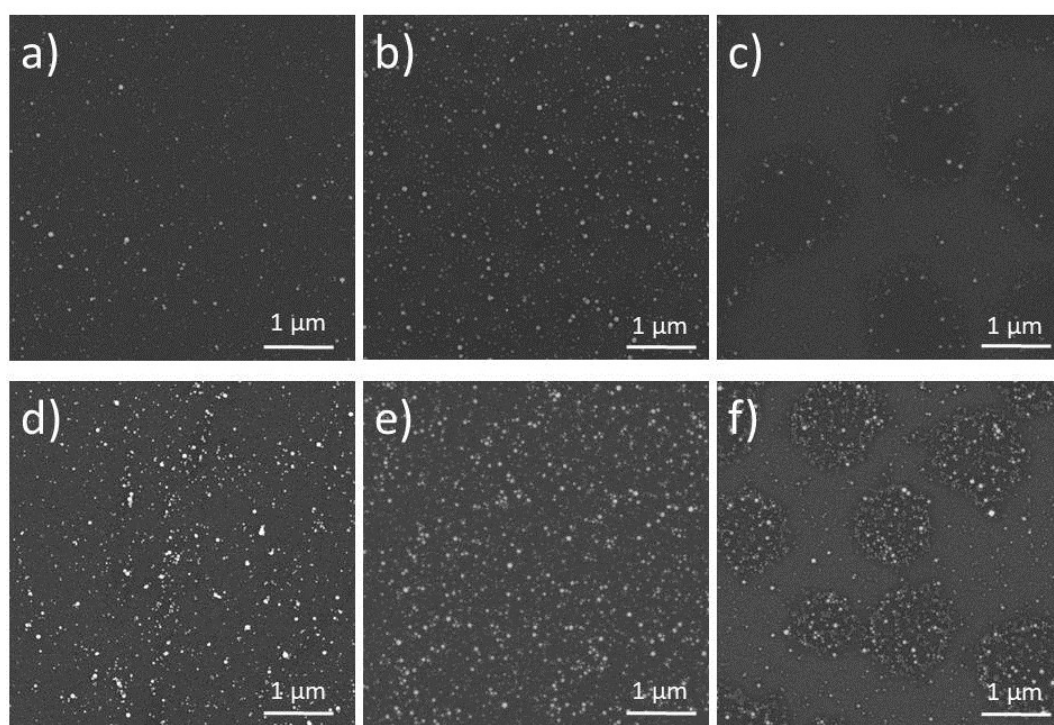


Figure 45. SEM images of (a, d) Si substrate, (b, e) PEO plasma polymer and (c, f) PS nanoislands with Cu NPs deposited for 5 s and 30 s, respectively.

Further characterization of the samples was performed using AFM. The images obtained on the samples after the 5 s decoration by Cu NPs with corresponding height profiles are shown in Figure 46. It is seen that Cu NPs become partially submerged when deposited onto ppPEO. The immersion of metal NPs into soft polymers was reported earlier [124]; however, in that case the NP implantation was driven by the heating of sample. Unfortunately, it is difficult to discuss the behavior of Cu NPs on the surface of PS-like nanoislands due to the difficulties with the background correction. Nevertheless, the topography image in Figure 46c) and shape of the cross-section in Figure 46f) do not exclude the presence of similar effect.

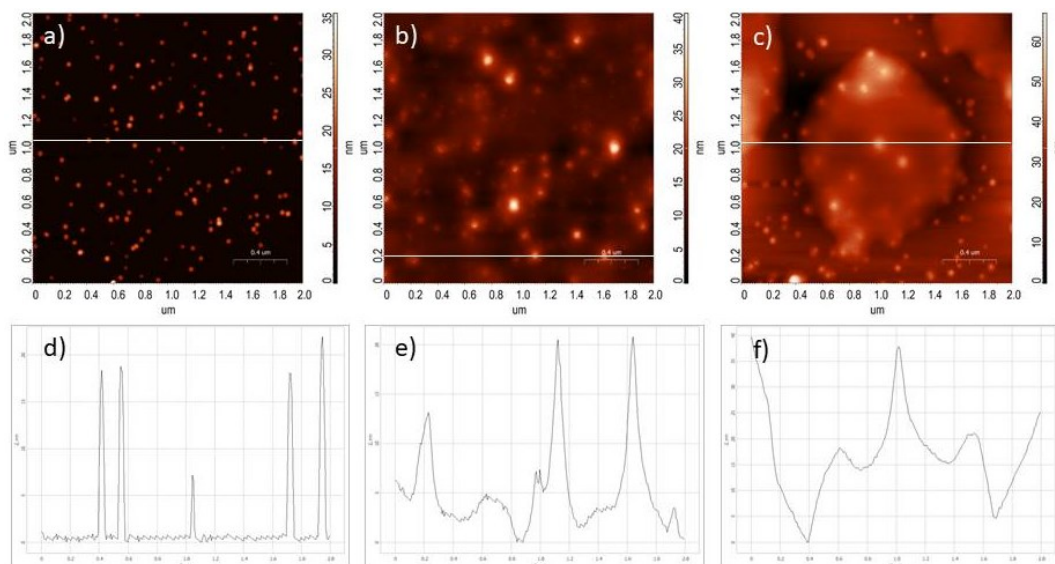


Figure 46. AFM top view images measured on (a) Si wafer, (b) PEO plasma polymer film and (c) PS nanoislands decorated by Cu NPs. Deposition time – 5 s. Corresponding height profiles are presented on the bottom images (d, e and f).

The parameter of Root Mean Square (RMS) roughness has been also determined using AFM. It is seen from Table 4 that the RMS roughness of PEOpp film decorated with Cu NPs increased with an increase of the amount of NPs. It provides the increase of WCA from 36° up to 93° . Such behavior is typical for the Cassie-Baxter wetting regime. The surface transforms from hydrophilic towards hydrophobic state. The RMS of the surface of PS-like nanoislands covered by Cu NPs is also higher compared with uncovered one. The WCA similarly increases after the decoration from 65° up to $\sim 90^{\circ}$. Therefore, the decoration of polymeric surfaces including plasma polymers by metallic NPs allow to tune the surface wettability.

Table 4. The RMS and WCA estimated for PEOpp and PS-like nanoislands decorated by Cu NPs.

Parameter	Deposition time – 0 s	Deposition time – 5 s	Deposition time – 30 s
PEO film (50 nm)			
RMS, nm	1.23 ± 0.23	3.38 ± 0.24	6.47 ± 0.35
WCA, °	36.0 ± 2.5	85.6 ± 7.6	93.0 ± 5.6
PS island			
RMS, nm	3.48 ± 0.61	4.55 ± 1.14	11.31 ± 0.83
WCA, °	65.0 ± 6.7	93.0 ± 8.5	87.1 ± 9.2

CONCLUSIONS

1. The combination of magnetron-based gas aggregation cluster source with plasma polymerization is an effective approach for the production of nanostructured thin films for the variety of potential applications.
2. Ag and Cu nanoparticles were first successfully detected *in-flight* inside the gas aggregation cluster source using synchrotron Small Angle X-ray Scattering. The distributions of particle size and relative concentration in the gas phase were determined. It was discovered that NPs are formed and grow at the distance of several mm from the magnetron target plane. Part of the nanoparticles becomes captured electrostatically in the vicinity of magnetron and therefore they grow to a bigger size of about 100 nm.
3. The UV-Vis spectroscopy can be applied for fast and simple *in-situ* detection of plasmonic NPs. The effect of NP trapping in the vicinity of magnetron was confirmed.
4. The deposition of NPs on the substrates mounted inside the aggregation chamber was performed. It was revealed that bigger NPs partially redeposit on the target and are lost on the walls. The redeposition is, most likely, due to the electrostatic force action.
5. Cu NPs/ppPEO plasma polymer nanocomposite films demonstrate bactericidal activity against multidrug resistant bacteria *MRSA* and *Pseudomonas Aureginosa*. However, the suppression of the non-fouling properties of ppPEO was established.
6. The formation of modified ppPEO layer at the Cu NPs/plasma polymer interface was discovered using AC-chip calorimetry technique. The modified layer has different chemical composition and reduced segmental dynamics compared to bulk ppPEO. Both factors can lead to the deterioration of non-fouling properties.
7. Polystyrene-like nanoislands were fabricated by Vapor Phase Deposition. The chemical composition of nanoislands is identical to the original polymer; however, molar mass distribution is shifted to smaller values.
8. The decoration of ppPEO thin film and PS-like nanoislands by Cu NPs influences the RMS and wettability of coatings.

BIBLIOGRAPHY

- [1] Y. Lu, K.W. Shah and J. Xu, "Synthesis, morphologies and building applications of nanostructured polymers". *Polymers*, vol. 9 2017.
- [2] A. Kausar, "Survey on Langmuir–Blodgett Films of Polymer and Polymeric Composite". *Polymer - Plastics Technology and Engineering*, vol. 56, pp. 932–945, 2017.
- [3] J.Y. Park and R.C. Advincula, "Nanostructuring polymers, colloids, and nanomaterials at the air-water interface through Langmuir and Langmuir-Blodgett techniques". *Soft Matter*, vol. 7, pp. 9829–9843, 2011.
- [4] H. Yasuda, "Glow discharge polymerization". *Journal of Polymer Science: Macromolecular Review*, vol. 16, pp. 199-293, 1981.
- [5] J. Goodman, "The formation of thin polymer films in the gas discharge". *Journal of Polymer Science*, vol. 44, pp. 551-552, 1960.
- [6] M. Shen, "Plasma chemistry of polymers". Marcel Dekker, New York 1976.
- [7] D.K. Lam, R.F. Baddour and A.F. Stancell, "A Mechanisms and Kinetics Study of Polymeric Thin-Film Deposition in Glow Discharge". *Journal of Macromolecular Science: Part A - Chemistry*, vol. 10, pp. 421–450, 1976.
- [8] H. Yasuda and T. Hsu, "Plasma polymerization investigated by the comparison of hydrocarbons and perfluorocarbons". *Surface Science*, vol. 76, pp. 232–241, 1978.
- [9] H. Yasuda, "Plasma Polymerization". Academic Press, New York 1985.
- [10] H. Biederman and Y. Osada, "Plasma Polymerization Processes". Elsevier, Amsterdam 1992.
- [11] H. Biederman, "Plasma Polymer Films". 2004.
- [12] H. Biederman, P. Bílková, J. Ježek, P. Hlídaek and D. Slavínská, "RF magnetron sputtering of polymers". *Journal of Non-Crystalline Solids*, vol. 218, pp. 44-49, 1997.
- [13] Y. Pihosh, H. Biederman, D. Slavinska, J. Kousal, A. Choukourov, M. Trchova, A. Mackova and A. Boldyryeva, "Composite SiOx/fluorocarbon plasma polymer films prepared by r.f. magnetron sputtering of SiO2 and PTFE". *Vacuum*, vol. 81, pp. 38-44, 2006.
- [14] M. Drábik, O. Polonskyi, O. Kylián, J. Čechvala, A. Artemenko, I. Gordeev, A. Choukourov, D. Slavínská, I. Matolínová and H. Biederman, "Super-hydrophobic coatings prepared by RF magnetron sputtering of PTFE". *Plasma*

Processes and Polymers, vol. 7, pp. 544-551, 2010.

- [15] V. Stelmashuk, H. Biederman, D. Slavínská, M. Trchová and P. Hlídaek, "Rf magnetron sputtering of polypropylene". *Vacuum*, vol. 75, pp. 207-215, 2004.
- [16] J. Hanus, J. Kousal, A. Choukourov, H. Biederman and D. Slavinska, "RF magnetron sputtering of poly(propylene) in a mixture of argon and nitrogen". *Plasma Processes and Polymers*, vol. 4, pp. S806-S811, 2007.
- [17] I. Kholodkov, H. Biederman, D. Slavínská, A. Choukourov and M. Trchova, "Plasma polymers prepared by RF sputtering of polyethylene". *Vacuum*, vol. 70, pp. 505-509, 2003.
- [18] J. Kousal, J. Hanuš, A. Choukourov, P. Hlídaek, H. Biederman, D. Slavínská and J. Zemek, "RF magnetron sputtering and evaporation of polyisobutylene and low density polyethylene". *Surface and Coatings Technology*, vol. 200, pp. 472-475, 2005.
- [19] Y. Pihosh, H. Biederman, D. Slavinska, J. Kousal, A. Choukourov, M. Trchova, A. Mackova and A. Boldyreva, "Composite SiOx/hydrocarbon plasma polymer films prepared by RF magnetron sputtering of SiO₂ and polyethylene or polypropylene". *Vacuum*, vol. 81, pp. 32-37, 2006.
- [20] A. Choukourov, J. Hanuš, J. Kousal, A. Grinevich, Y. Pihosh, D. Slavínská and H. Biederman, "Plasma polymer films from sputtered polyimide". *Vacuum*, vol. 81, pp. 517-526, 2006.
- [21] M. Drabik, J. Kousal, Y. Pihosh, A. Choukourov, H. Biederman, D. Slavinska, A. Mackova, A. Boldyreva and J. Pesicka, "Composite SiOx / hydrocarbon plasma polymer films prepared by RF magnetron sputtering of SiO₂ and polyimide". *Vacuum*, vol. 81, pp. 920-927, 2007.
- [22] Y. Wang, Y. Ye, H. Li, L. Ji, J. Chen and H. Zhou, "A magnetron sputtering technique to prepare a-C:H films: Effect of substrate bias". *Applied Surface Science*, vol. 257, pp. 1990-1995, 2011.
- [23] N. Menegazzo, D. Boyne, H. Bui, T.P. Beebe and K.S. Booksh, "DC magnetron sputtered polyaniline-HCl thin films for chemical sensing applications". *Analytical Chemistry*, vol. 84, pp. 5770-5777, 2012.
- [24] O. Kylián, J. Kousal, A. Artemenko, A. Choukourov, M. Petr, O. Polonskyi, D. Slavinska and H. Biederman, "Deposition of amino-rich coatings by RF magnetron sputtering of Nylon: In-situ characterization of the deposition process". *Surface and Coatings Technology*, vol. 205, pp. S558-S561, 2011.

- [25] O. Kylián, A. Choukourov and H. Biederman, "Nanostructured plasma polymers". *Thin Solid Films*, vol. 548, pp. 1–17, 2013.
- [26] A. Choukourov, J. Hanuš, J. Kousal, A. Grinevich, Y. Pihosh, D. Slavínská and H. Biederman, "Thin polymer films from polyimide vacuum thermal degradation with and without a glow discharge". *Vacuum*, vol. 80, pp. 923–929, 2006.
- [27] A. Choukourov, A. Grinevich, O. Polonskyi, J. Kousal, D. Slavinska, H. Biederman, A. Choukourov, A. Grinevich, O. Polonskyi, J. Hanus, J. Kousal, D. Slavinska and H. Biederman, "Vacuum Thermal Degradation of Poly (ethylene oxide)". *The Journal of Physical Chemistry B*, vol. 113, pp. 2984–2989, 2009.
- [28] A. Choukourov, I. Gordeev, O. Polonskyi, A. Artemenko, L. Hanyková, I. Krakovský, O. Kylián, D. Slavínská and H. Biederman, "Poly(ethylene oxide)-like Plasma Polymers Produced by Plasma-Assisted Vacuum Evaporation". *Plasma Processes and Polymers*, vol. 7, pp. 445–458, 2010.
- [29] J.H. Lee, H.B. Lee and J.D. Andrade, "Blood compatibility of polyethylene oxide surfaces". *Progress in Polymer Science*, vol. 20, pp. 1043–1079, 1995.
- [30] S. Madkour, H. Yin, M. Füllbrandt and A. Schönhals, "Calorimetric evidence for a mobile surface layer in ultrathin polymeric films: poly(2-vinyl pyridine)". *Soft Matter*, vol. 11, pp. 7942–7952, 2015.
- [31] S. Madkou, I. Melnichu, A. Choukourov, I. Krakovsky, H. Biederman and A. Schönhals, "In Situ Nanocalorimetric Investigations of Plasma Assisted Deposited Poly(ethylene oxide)-like Films by Specific Heat Spectroscopy". *The Journal of Physical Chemistry B*, vol. 120, pp. 3954–3962, 2016.
- [32] A. Zaitsev, F. Poncin-Epaillard, A. Lacoste and D. Debarnot, "A Bottom-Up and Templateless Process for the Elaboration of Plasma-Polymer Nanostructures". *Plasma Processes and Polymers*, vol. 13, pp. 227–235, 2016.
- [33] A. Zaitsev, A. Lacoste, F. Poncin-Epaillard, A. Bès and D. Debarnot, "Nanotexturing of plasma-polymer thin films using argon plasma treatment". *Surface and Coatings Technology*, vol. 330, pp. 196–203, 2017.
- [34] K. Du, Y. Jiang, Y. Liu, I. Wathuthanthri and C.H. Choi, "Manipulation of the superhydrophobicity of plasma-etched polymer nanostructures". *Micromachines*, vol. 9, 2018.
- [35] F. Henry, F. Renaux, S. Coppée, R. Lazzaroni, N. Vandencastele, F. Reniers

- and R. Snyders, "Synthesis of superhydrophobic PTFE-like thin films by self-nanostructuration in a hybrid plasma process". *Surface Science*, vol. 606, pp. 1825-1829, 2012.
- [36] A. Milella, R. Di Mundo, F. Palumbo, P. Favia, F. Fracassi and R. d'Agostino, "Plasma nanostructuring of polymers: Different routes to superhydrophobicity". *Plasma Processes and Polymers*, vol. 6, pp. 460-466, 2009.
- [37] G.D. Fu, E.T. Kang and K.G. Neoh, "Deposition of Nanostructured Fluoropolymer Films on Silicon Substrates via Plasma Polymerization of Allylpentafluorobenzene". *Journal of Physical Chemistry B*, vol. 107, pp. 13902-13910, 2003.
- [38] J. Feng and W. Huang, "Nanostructured ultra-low- κ porous fluoropolymer composite films via plasma co-polymerization of hydrophobic and hydrophilic monomers and subsequent hydrolysis treatment". *European Polymer Journal*, vol. 43, 3773-3779, 2007.
- [39] A. Choukourov, I. Gordeev, J. Ponti, C. Uboldi, I. Melnichuk, M. Vaidulych, J. Kousal, D. Nikitin, L. Hanyková, I. Krakovský, D. Slavínská and H. Biederman, "Microphase-Separated PE/PEO Thin Films Prepared by Plasma-Assisted Vapor Phase Deposition". *ACS Applied Materials and Interfaces*, vol. 8, pp. 8201-8212, 2016.
- [40] A. Choukourov, P. Pleskunov, D. Nikitin, R. Tafiichuk, A. Shelemin, J. Hanuš, J. Májek, M. Unger, A. Roy and A. Ryabov, "Plasma-assisted growth of polyethylene fractal nano-islands on polyethylene oxide films: Impact of film confinement and glassy dynamics on fractal morphologies". *Applied Surface Science*, vol. 489, pp. 55-65, 2019.
- [41] J. Berndt, H. Acid, E. Kovacevic, C. Cachoncinlle, T. Strunskus and L. Boufendi, "Deposition and tuning of nanostructured hydrocarbon deposits: From superhydrophobic to superhydrophilic and back". *Journal of Applied Physics*, vol. 113, pp. 063302, 2013.
- [42] A. Serov, A. Choukourov, I. Melnichuk, A. Shelemin, A. Kuzminova, O. Kylián, J. Hanuš, J. Kousal, M. Drábik, D. Slavínská and H. Biederman, "Poly(tetrafluoroethylene) sputtering in a gas aggregation source for fabrication of nano-structured deposits". *Surface and Coatings Technology*, vol. 254, pp. 319-326, 2014.

- [43] A. Shelemin, D. Nikitin, A. Choukourov, O. Kylián, J. Kousal, I. Khalakhan, I. Melnichuk, D. Slavínská and H. Biederman, "Preparation of biomimetic nano-structured films with multi-scale roughness". *Journal of Physics D: Applied Physics*, vol. 49, pp. 254001, 2016.
- [44] M.M. Hawkeye and M.J. Brett, "Glancing angle deposition: Fabrication, properties, and applications of micro-and nanostructured thin films". *Journal of Vacuum Science & Technology A*, vol. 25, pp. 1317, 2007.
- [45] O. Kylian, A. Shelemin, P. Solar, A. Choukourov, J. Hanus, M. Vaidulych, A. Kuzminova and H. Biederman, "Plasma polymers: From thin films to nanocolumnar coatings". *Thin Solid Films*, vol. 630, pp. 86-91, 2017.
- [46] A. Choukourov, P. Solar, O. Polonskyi, J. Hanus, M. Drabik, O. Kylian, E. Pavlova, D. Slavinska and H. Biederman, "Structured Ti/Hydrocarbon plasma polymer nanocomposites produced by magnetron sputtering with glancing angle deposition". *Plasma Processes and Polymers*, vol. 7, pp. 25-32, 2010.
- [47] A. Grinevich, L. Bacakova, A. Choukourov, H. Boldyryeva, Y. Pihosh, D. Slavinska, L. Noskova, M. Skuciova, V. Lisa and H. Biederman, "Nanocomposite Ti/hydrocarbon plasma polymer films from reactive magnetron sputtering as growth support for osteoblast-like and endothelial cells.". *Journal of biomedical materials research Part A*, vol. 88, pp. 952–66, 2009.
- [48] K. Vasilev, "Nanoengineered plasma polymer films for biomaterial applications". *Plasma Chemistry and Plasma Processing*, vol. 34, pp. 545-558, 2014.
- [49] S. Seino, S. Sasaki, T. Owashi, K. Oya and S. Iwamori, "Effects of copper interfacial layer on surface characteristics, adhesion and wear durability of fluorocarbon thin film sputtered onto polyimide film substrate". *Vacuum*, vol. 111, pp. 160-165, 2015.
- [50] I. Sondi and B. Salopek-Sondi, "Silver nanoparticles as antimicrobial agent: A case study on E. coli as a model for Gram-negative bacteria". *Journal of Colloid and Interface Science*, vol. 275, pp. 177–182, 2004.
- [51] F. Paladini, M. Pollini, A. Sannino and L. Ambrosio, "Metal-based antibacterial substrates for biomedical applications". *Biomacromolecules*, vol. 16, pp. 1873–1885, 2015.
- [52] A. Kuzminova, J. Kratochvíl, A. Shelemin, O. Kylián, H. Biederman and J.

- Beranová, "Preparation of Antibacterial Silver Containing Nanocomposites". *WDS 2013. Book of abstracts*, pp. 102–107, 2014.
- [53] H. Palza, "Antimicrobial polymers with metal nanoparticles". *International Journal of Molecular Sciences*, vol. 16, pp. 2099–2116, 2015.
- [54] P. Lalueza, M. Monzon, M. Arruebo and J. Santamaría, "Bactericidal effects of different silver-containing materials". *Materials Research Bulletin*, vol. 46, pp. 2070–2076, 2011.
- [55] B. Le Ouay and F. Stellacci, "Antibacterial activity of silver nanoparticles: A surface science insight". *Nano Today*, vol. 10, pp. 339–354, 2015.
- [56] K.C. Anyaogu, A. V. Fedorov and D.C. Neckers, "Synthesis, characterization, and antifouling potential of functionalized copper nanoparticles". *Langmuir*, vol. 24, pp. 4340–4346, 2008.
- [57] L. Tamayo, M. Azócar, M. Kogan, A. Riveros and M. Páez, "Copper-polymer nanocomposites: An excellent and cost-effective biocide for use on antibacterial surfaces". *Materials Science and Engineering: C*, vol. 69, pp. 1391–1409, 2016.
- [58] K. Sunada, M. Minoshima and K. Hashimoto, "Highly efficient antiviral and antibacterial activities of solid-state cuprous compounds". *Journal of Hazardous Materials*, vol. 235–236, pp. 265–270, 2012.
- [59] H.L. Karlsson, P. Cronholm, Y. Hedberg, M. Tornberg, L. De Battice, S. Svedhem and I.O. Wallinder, "Cell membrane damage and protein interaction induced by copper containing nanoparticles-Importance of the metal release process". *Toxicology*, vol. 313, pp. 59–69, 2013.
- [60] V. Zaporojchenko, R. Podschun, U. Schürmann, A. Kulkarni and F. Faupel, "Physico-chemical and antimicrobial properties of co-sputtered Ag-Au/PTFE nanocomposite coatings". *Nanotechnology*, vol. 17, pp. 4904–4908, 2006.
- [61] E. Körner, M.H. Aguirre, G. Fortunato, A. Ritter, J. Rühle and D. Hegemann, "Formation and distribution of silver nanoparticles in a functional plasma polymer matrix and related Ag⁺ release properties". *Plasma Processes and Polymers*, vol. 7, pp. 619–625, 2010.
- [62] S. Lischer, E. Körner, D.J. Balazs, D. Shen, P. Wick, K. Grieder, D. Haas, M. Heuberger and D. Hegemann, "Antibacterial burst-release from minimal Ag-containing plasma polymer coatings". *Journal of the Royal Society Interface*, vol. 8, pp. 1019–1030, 2011.

- [63] L. Ploux, M. Mateescu, K. Anselme and K. Vasilev, "Antibacterial Properties of Silver-Loaded Plasma Polymer Coatings". *Journal of Nanomaterials*, vol. 2012, 2012.
- [64] N. Alissawi, T. Peter, T. Strunskus, C. Ebbert, G. Grundmeier and F. Faupel, "Plasma-polymerized HMDSO coatings to adjust the silver ion release properties of Ag/polymer nanocomposites". *Journal of Nanoparticle Research*, vol. 15, 2013.
- [65] N. De Vietro, A. Conte, A.L. Incoronato, M.A. Del Nobile and F. Fracassi, "Aerosol-assisted low pressure plasma deposition of antimicrobial hybrid organic-inorganic Cu-composite thin films for food packaging applications". *Innovative Food Science and Emerging Technologies*, vol. 41, pp. 130-134, 2017.
- [66] A.H. Pfund, "BISMUTH BLACK AND ITS APPLICATIONS.". *Review of Scientific Instruments Journal of Applied Physics*, vol. 1, pp. 397, 1930.
- [67] C.J. Duthler, S.E. Johnson and H.P. Broida, "Plasma-Resonance Scattering from Small Sodium Particles Formed in a Flowing Gas Stream". *Physical Review Letters*, vol. 26, pp. 1236–1239, 1971.
- [68] F. Frank, W. Schulze, B. Tesche, J. Urban and B. Winter, "Formation of metal clusters and molecules by means of the gas aggregation technique and characterisation of size distribution". *Surface Science*, vol. 156, pp. 90–99, 1985.
- [69] C.G. Granqvist and R.A. Buhrman, "Ultrafine metal particles". *Journal of Applied Physics*, vol. 47, pp. 2200–2219, 1976.
- [70] H. Haberland, M. Karrais and M. Mall, "Atoms, Molecules and Clusters A new type of cluster and cluster ion source", *Zeitschrift für Physik D Atoms, Molecules and Clusters*, vol. 20, pp. 413-415, 1991.
- [71] D. Datta, S.R. Bhattacharyya, I. Shyjumon, D. Ghose and R. Hippler, "Production and deposition of energetic metal nanocluster ions of silver on Si substrates". *Surface and Coatings Technology*, vol. 203, pp. 2452-2457, 2009.
- [72] V. Straňák, S. Block, S. Drache, Z. Hubička, C.A. Helm, L. Jastrabík, M. Tichý and R. Hippler, "Size-controlled formation of Cu nanoclusters in pulsed magnetron sputtering system". *Surface and Coatings Technology*, vol. 205, pp. 2755-2762, 2011.
- [73] A. Marek, J. Valter, S. Kadlec and J. Vyskočil, "Gas aggregation nanocluster

- source - Reactive sputter deposition of copper and titanium nanoclusters". *Surface and Coatings Technology*, vol. 205, pp. S573-S576, 2011.
- [74] M. Gracia-Pinilla, • E Martínez, • G Silva Vidaurri and E. Pérez-Tijerina, "Deposition of Size-Selected Cu Nanoparticles by Inert Gas Condensation". *Nanoscale Research Letters*, vol. 5, pp. 180–188, 2010.
- [75] M. Ganeva, T. Peter, S. Bornholdt, H. Kersten, T. Strunskus, V. Zaporojtchenko, F. Faupel and R. Hippler, "Mass Spectrometric Investigations of Nano-Size Cluster Ions Produced by High Pressure Magnetron Sputtering". *Contributions to Plasma Physics*, vol 52, pp. 881–889, 2012.
- [76] N.K. Manninen, N.M. Figueiredo, S. Carvalho and A. Cavaleiro, "Production and characterization of Ag nanoclusters produced by plasma gas condensation". *Plasma Processes and Polymers*, vol. 11, pp. 629–638, 2014.
- [77] Y. Yan, T. Santaniello, L.G. Bettini, C. Minnai, A. Bellacicca, R. Porotti, I. Denti, G. Faraone, M. Merlini, C. Lenardi and P. Milani, "Electroactive Ionic Soft Actuators with Monolithically Integrated Gold Nanocomposite Electrodes". *Advanced Materials*, vol. 29, pp. 1606109, 2017.
- [78] T. Kretková, J. Hanuš, O. Kylián, P. Solař, M. Dopita, M. Cieslar, I. Khalakhan, A. Choukourov and H. Biederman, "In-flight modification of Ni nanoparticles by tubular magnetron sputtering". *Journal of Physics D: Applied Physics*, vol. 52, pp. 205302, 2019.
- [79] O. Kylián, V. Valeš, O. Polonskyi, J. Pešička, J. Čechvala, P. Solař, A. Choukourov, D. Slavínská and H. Biederman, "Deposition of Pt nanoclusters by means of gas aggregation cluster source". *Materials Letters*, vol. 79, pp. 229–231, 2012.
- [80] A. Shelemin, O. Kylián, J. Hanuš, A. Choukourov, I. Melnichuk, H. Biederman, A. Serov and D. Slavínsk, "Preparation of metal oxide nanoparticles by gas aggregation cluster source". vol. 120, pp. 162–169, 2015.
- [81] R. Rudd, A. Obrušník, P. Zikán, R. Pratt, C. Hall, P. Murphy, D. Evans and E. Charrault, "Manipulation of cluster formation through gas-wall boundary conditions in large area cluster sources". *Surface and Coatings Technology*, vol. 314, pp. 125–130, 2017.
- [82] M. Drábik, A. Serov, O. Kylián, A. Choukourov, A. Artemenko, J. Kousal, O. Polonskyi and H. Biederman, "Deposition of fluorocarbon nanoclusters by gas aggregation cluster source". *Plasma Processes and Polymers*, vol. 9, pp. 390–

397, 2012.

- [83] O. Polonskyi, O. Kylián, P. Solař, A. Artemenko, J. Kousal, D. Slavínská, A. Choukourov and H. Biederman, "Nylon-sputtered nanoparticles: Fabrication and basic properties". *Journal of Physics D: Applied Physics*, vol. 45, pp. 495301, 2012.
- [84] Y. Huttel, L. Martínez, A. Mayoral and I. Fernández, "Gas-phase synthesis of nanoparticles: present status and perspectives". *MRS Communications*, vol. 8, pp. 947–954, 2018.
- [85] A. Choukourov, P. Solař, F. Faupel, H. Biederman, O. Polonskyi, A. Olbricht, A. Hinz, A. Shelemin and O. Kylián, "Single-step generation of metal-plasma polymer multicore@shell nanoparticles from the gas phase". *Scientific Reports*, vol. 7, pp. 6–11, 2017.
- [86] Y. Huttel, "Gas-Phase Synthesis of Nanoparticles". 2017.
- [87] O. Kylián, J. Kratochvíl, J. Hanuš, O. Polonskyi, P. Solař and H. Biederman, "Fabrication of Cu nanoclusters and their use for production of Cu/plasma polymer nanocomposite thin films". *Thin Solid Films*, vol. 550, pp. 46–52, 2014.
- [88] A. Choukourov, O. Kylián, M. Petr, M. Vaidulych, D. Nikitin, J. Hanuš, A. Artemenko, A. Shelemin, I. Gordeev, Z. Kolská, P. Solař, I. Khalakhan, A. Ryabov, J. Májek, D. Slavínská and H. Biederman, "RMS roughness-independent tuning of surface wettability by tailoring silver nanoparticles with a fluorocarbon plasma polymer". *Nanoscale*, vol. 9, pp. 2616–2625, 2017.
- [89] A. Kuzminova, J. Beranová, O. Polonskyi, A. Shelemin, O. Kylián, A. Choukourov, D. Slavínská and H. Biederman, "Antibacterial nanocomposite coatings produced by means of gas aggregation source of silver nanoparticles". *Surface and Coatings Technology*, vol. 294, pp. 225–230, 2016.
- [90] M. Vaidulych, J. Hanuš, T. Steinhartová, O. Kylián, A. Choukourov, J. Beranová, I. Khalakhan and H. Biederman, "Deposition of Ag/a-C:H nanocomposite films with Ag surface enrichment". *Plasma Processes and Polymers*, vol. 14, pp. 1600256, 2017.
- [91] M. Vaidulych, A. Shelemin, J. Hanuš, I. Khalakhan, I. Krakovsky, P. Kočová, H. Mašková, J. Kratochvíl, P. Pleskunov, J. Štěrbá, O. Kylián, A. Choukourov and H. Biederman, "Superwetable antibacterial textiles for versatile oil/water

- separation". *Plasma Processes and Polymers*, vol. 16, pp. 1900003, 2019.
- [92] J. Kousal, D. Slavínská, H. Biederman, J. Pešička, O. Polonskyi, A. Artemenko, A. Choukourov and O. Kylián, "Characterization of nanoparticle flow produced by gas aggregation source". *Vacuum*, vol. 96, pp. 32–38, 2013.
- [93] L. Zhang, J. Shao and X. Chen, "Numerical simulation of nanocluster motion through a DC magnetron nanocluster source". *Vacuum*, vol. 128, pp. 137–145, 2016.
- [94] J. Kousal, A. Kolpaková, A. Shelemin, P. Kudrna, M. Tichý, O. Kylián, J. Hanuš, A. Choukourov and H. Biederman, "Monitoring of conditions inside gas aggregation cluster source during production of Ti/TiO_x nanoparticles". *Plasma Sources Science and Technology*, vol. 26, pp. 105003, 2017.
- [95] S. Gauter, F. Haase, P. Solař, O. Kylián, P. Kúš, A. Choukourov, H. Biederman and H. Kersten, "Calorimetric investigations in a gas aggregation source". *Journal of Applied Physics*, vol. 124, pp. 037301, 2018.
- [96] G. Benecke, W. Wagermaier, C. Li, M. Schwartzkopf, G. Flucke, R. Hoerth, I. Zizak, M. Burghammer, E. Metwalli, P. Müller-Buschbaum, M. Trebbin, S. Förster, O. Paris, S. V. Roth and P. Fratzl, "A customizable software for fast reduction and analysis of large X-ray scattering data sets: applications of the new DPDAK package to small-angle X-ray scattering and grazing-incidence small-angle X-ray scattering". *Journal of Applied Crystallography*, vol. 47, pp. 1797–1803, 2014.
- [97] "<https://www.sasview.org>."
- [98] O. Polonskyi, P. Solař, O. Kylián, M. Drábik, A. Artemenko, J. Kousal, J. Hanuš, J. Pešička, I. Matolínová, E. Kolíbalová, D. Slavínská and H. Biederman, "Nanocomposite metal/plasma polymer films prepared by means of gas aggregation cluster source". *Thin Solid Films*, vol. 520, pp. 4155–4162, 2012.
- [99] O. Kylian, J. Kratochvil, J. Hanus, O. Polonskyi, P. Solar and H. Biederman, "Fabrication of Cu nanoclusters and their use for production of Cu/plasma polymer nanocomposite thin films". *Thin Solid Films*, vol. 550, pp. 46–52, 2014.
- [100] J. Blažek, J. Kousal, H. Biederman, O. Kylián, J. Hanuš and D. Slavínská, "Charging of nanoparticles in stationary plasma in a gas aggregation cluster source". *Journal of Physics D: Applied Physics*, vol. 48, pp. 415202, 2015.

- [101] O. Polonskyi, J.W. Abraham, T. Strunskus, M. Bonitz and F. Faupel, "In-situ investigation of early stages of Ag nanoparticle growth in a low temperature plasma". *Book of Extended Abstracts ISPC 23*, pp. 590–592, 2017.
- [102] J. Kratochvil, A. Kuzminova, O. Kylian and H. Biederman, "Comparison of magnetron sputtering and gas aggregation nanoparticle source used for fabrication of silver nanoparticle films". *Surface and Coatings Technology*, vol. 275, pp. 296–302, 2014.
- [103] J. Kousal, A. Shelemin, M. Schwartzkopf, O. Polonskyi, J. Hanuš, P. Solař, M. Vaidulych, D. Nikitin, P. Pleskunov, Z. Krtouš, T. Strunskus, F. Faupel, S. V. Roth, H. Biederman and A. Choukourov, "Magnetron-sputtered copper nanoparticles: lost in gas aggregation and found by in situ X-ray scattering". *Nanoscale*, vol. 10, pp. 18275–18281, 2018.
- [104] A. Choukourov, I. Gordeev, D. Arzhakov, A. Artemenko, J. Kousal, O. Kylián, D. Slavínská and H. Biederman, "Does Cross-Link Density of PEO-Like Plasma Polymers Influence their Resistance to Adsorption of Fibrinogen?". *Plasma Processes and Polymers*, vol. 9, pp. 48–58, 2012.
- [105] J. Moulder, "Handbook of X-ray photoelectron spectroscopy: a reference book of standard spectra for identification and interpretation of XPS data," 1992.
- [106] C.C. Chusuei, M.A. Brookshier and D.W. Goodman, "Correlation of relative X-ray photoelectron spectroscopy shake-up intensity with CuO particle size". *Langmuir*. <https://doi.org/10.1021/la9815446> 1999.
- [107] M. Füllbrandt, P.J. Purohit and A. Schönhals, "Combined FTIR and Dielectric Investigation of Poly(vinyl acetate) Adsorbed on Silica Particles". *Macromolecules*, vol. 46, pp. 4626–4632, 2013.
- [108] A.P. Holt, P.J. Griffin, V. Bocharova, A.L. Agapov, A.E. Imel, M.D. Dadmun, J.R. Sangoro and A.P. Sokolov, "Dynamics at the Polymer/Nanoparticle Interface in Poly(2-vinylpyridine)/Silica Nanocomposites". *Macromolecules*, vol. 47, pp. 1837–1843, 2014.
- [109] S. Madkour, P. Szymoniak, M. Heidari, R. von Klitzing and A. Schönhals, "Unveiling the Dynamics of Self-Assembled Layers of Thin Films of Poly(vinyl methyl ether) (PVME) by Nanosized Relaxation Spectroscopy". *ACS Applied Materials & Interfaces*, vol. 9, pp. 7535–7546, 2017.
- [110] S. Madkour, P. Szymoniak, J. Radnik and A. Schönhals, "Unraveling the Dynamics of Nanoscopically Confined PVME in Thin Films of a Miscible

- PVME/PS Blend". *ACS Applied Materials & Interfaces*, vol. 9, pp. 37289–37299, 2017.
- [111] H. Vogel, "Das Temperaturabhaengigkeitsgesetz der Viskosität von Flüssigkeiten". *Physikalische Zeitschrift*, vol. 22, pp. 645.
- [112] G.S. Fulcher, "Analysis of Recent Measurements of the Viscosity of Glasses". *Journal of the American Ceramic Society*, vol. 8, pp. 339–355, 1925.
- [113] G. Tammann and W. Hesse, "Die Abhängigkeit der Viskosität von der Temperatur bei unterkühlten Flüssigkeiten". *Zeitschrift für anorganische und allgemeine Chemie*, vol. 156, pp. 245–257, 1926.
- [114] D. Labahn, R. Mix and A. Schönhals, "Dielectric relaxation of ultrathin films of supported polysulfone". *Physical Review E*, vol. 79, pp. 011801, 2009.
- [115] H. Yin, S. Napolitano and A. Schönhals, "Molecular Mobility and Glass Transition of Thin Films of Poly(bisphenol A carbonate)". *Macromolecules*, vol. 45, pp. 1652–1662, 2012.
- [116] Z. Zhao, H. Ni, Z. Han, T. Jiang, Y. Xu, X. Lu and P. Ye, "Effect of Surface Compositional Heterogeneities and Microphase Segregation of Fluorinated Amphiphilic Copolymers on Antifouling Performance". *ACS Applied Materials & Interfaces*, vol. 5, pp. 7808–7818, 2013.
- [117] I. Melnichuk, A. Choukourov, M. Bilek, A. Weiss, M. Vandrovcová, L. Bačaková, J. Hanuš, P. Solař, D. Slavínská and H. Biederman, "Direct covalent coupling of proteins to nanostructured plasma polymers: a route to tunable cell adhesion". vol. 351, pp. 537–545, 2015.
- [118] A. Kuzminova, J. Beranová, O. Polonskyi, A. Shelemin, O. Kylián, A. Choukourov, D. Slavínská and H. Biederman, "Antibacterial nanocomposite coatings produced by means of gas aggregation source of silver nanoparticles". *Surface and Coatings Technology*, vol. 294, pp. 225–230, 2016.
- [119] O. Kylián, J. Kratochvíl, M. Petr, A. Kuzminova, D. Slavínská, H. Biederman and J. Beranová, "Ag/C:F Antibacterial and hydrophobic nanocomposite coatings". *Functional Materials Letters*, vol. 10, pp. 1750029, 2017.
- [120] L. Vaccari, M. Molaei, T.H.R. Niepa, D. Lee, R.L. Leheny and K.J. Stebe, "Films of bacteria at interfaces". *Advances in Colloid and Interface Science*, vol. 247, pp. 561–572, 2017.
- [121] N.M. Mackie, D.G. Castner and E.R. Fisher, "Characterization of Pulsed-

- Plasma-Polymerized Aromatic Films". *Langmuir*, vol. 14, pp. 1227–1235, 2002.
- [122] M. Haïdopoulos, F. Mirabella, M. Horgnies, C. Volcke, P.A. Thiry, P. Rouxhet and J.J. Pireaux, "Morphology of polystyrene films deposited by RF plasma". *Journal of Microscopy*, vol. 228, pp. 227–239, 2007.
- [123] Y.-L. Lee, C.-H. Chen and Y.-M. Yang, "Surface Morphology and Wetting Behavior of Poly(α -methylstyrene) Thin Films Prepared by Vacuum Deposition". *Langmuir*, vol. 14, pp. 6980–6986, 2002.
- [124] M. Hanif, R.R. Juluri, M. Chirumamilla and V.N. Popok, "Poly(methyl methacrylate) composites with size-selected silver nanoparticles fabricated using cluster beam technique". *Journal of Polymer Science Part B: Polymer Physics*, vol. 54, pp. 1152–1159, 2016.

LIST OF TABLES

Table 1. The main characteristics of the bacterial strains used in the research.....26

Table 2. Chemical composition of ppPEO as obtained from fitting of the C1s XPS spectra.....54

Table 3. Nitrogen content on the surface of different samples after their incubation in a 50 µg/ml BSA solution.....64

Table 4. The RMS and WCA estimated for PEOpp and PS-like nanoislands decorated by Cu NPs.....75

LIST OF ABBREVIATIONS

AFM	atomic force microscopy
BSA	bovine serum albumin
CFU	colony forming unit
FTIR	Fourier-transform infrared spectroscopy
GAS	gas aggregation cluster source
GPC	gel permeation chromatography
HMDSO	hexamethyldisiloxane
LSPR	Localized Surface Plasmon Resonance
MRSA	<i>Methicillin-resistant staphylococcus aureus</i>
NMR	nuclear magnetic resonance
NPs	nanoparticles
PBS	phosphate buffered saline
PEO	poly(ethylene oxide)
ppPEO	PEO plasma polymer
PS	polystyrene
PTFE	polytetrafluoroethylene
QCM	quartz crystal microbalance
RF	radio frequency
ROS	reactive oxygen species
SAXS	small angle X-ray scattering
SEM	scanning electron microscopy
SHS	specific heat spectroscopy
TEM	Transmission Electron Microscopy
VFT	Vogel/Fulcher/Tammann
WCA	water contact angle
XPS	X-ray photoelectron spectroscopy

LIST OF PUBLICATIONS

Reviewed international journals

1. I. Gordeev, M. Šimek, V. Prukner, A. Artemenko, J. Kousal, **D. Nikitin**, A. Choukourov, H. Biederman, “Deposition of Poly(Ethylene Oxide) – Like Plasma Polymers on Inner Surfaces of Cavities by Means of Atmospheric Pressure SDBD – Based Jet,” *Plasma Process. Polym.*, vol. 13, no. 8, pp. 823–833, 2016.
2. A. Choukourov, I. Gordeev, J. Ponti, C. Uboldi, I. Melnichuk, M. Vaidulych, J. Kousal, **D. Nikitin**, L. Hanyková, I. Krakovský, D. Slavínská, H. Biederman, “Microphase-Separated PE/PEO Thin Films Prepared by Plasma-Assisted Vapor Phase Deposition,” *ACS Appl. Mater. Interfaces*, vol. 8, no. 12, pp. 8201–8212, 2016.
3. A. Shelemin, **D. Nikitin**, A. Choukourov, O. Kylián, J. Kousal, I. Khalakhan, I. Melnichuk, D. Slavínská, H. Biederman, “Preparation of biomimetic nano-structured films with multi-scale roughness,” *Journal of Physics D: Applied Physics*, vol. 49, no. 25, 2016.
4. **D. Nikitin**, A. Choukourov, V. Titov, L. Kuzmicheva, I. Lipatova, E. Mezina, V. Aleksandriiskii, A. Shelemin, I. Khalakhan, D. Slavinska, H. Biederman, “In situ coupling of chitosan onto polypropylene foils by an Atmospheric Pressure Air Glow Discharge with a liquid cathode”, *Carbohydrate Polymers*, vol. 154, pp. 30–39, 2016.
5. A. Choukourov, O. Kylián, M. Petr, M. Vaidulych, **D. Nikitin**, J. Hanuš, A. Artemenko, A. Shelemin, I. Gordeev, Z. Kolská, P. Solař, I. Khalakhan, A. Ryabov, J. Májek, D. Slavínská, H. Biederman, “RMS roughness-independent tuning of surface wettability by tailoring silver nanoparticles with a fluorocarbon plasma polymer,” *Nanoscale*, vol. 9, no. 7, pp. 2616–2625, 2017.
6. A. Choukourov, P. Pleskunov, **D. Nikitin**, V. Titov, A. Shelemin, M. Vaidulych, A. Kuzminova, P. Solař, J. Hanuš, J. Kousal, O. Kylián, D. Slavínská, H. Biederman, “Advances and challenges in the field of plasma polymer nanoparticles,” *Beilstein Journal of Nanotechnology*, vol. 8, pp. 2002–2014, 2017.
7. P. Pleskunov, **D. Nikitin**, R. Tafiichuk, A. Shelemin, J. Hanuš, I. Khalakhan, A. Choukourov, “Carboxyl-Functionalized Nanoparticles Produced by Pulsed Plasma Polymerization of Acrylic Acid,” *J. Phys. Chem. B*, vol. 122, no. 14, pp. 4187–4194, 2018.

8. A. Choukourov, A. Shelemin, P. Pleskunov, **D. Nikitin**, I. Khalakhan, J. Hanuš, “Nanoscale morphogenesis of nylon-sputtered plasma polymer particles,” *Journal of Physics D: Applied Physics*, vol. 51, no. 21, 2018.
9. O. Surov, M. Voronova, N. Rubleva, L. Kuzmicheva, **D. Nikitin**, A. Choukourov, V. Titov, A. Zakharov, “A novel effective approach of nanocrystalline cellulose production: oxidation–hydrolysis strategy,” *Cellulose*, vol. 25, no. 9, pp. 5035–5048, 2018.
10. J. Kousal, A. Shelemin, M. Schwartzkopf, O. Polonskyi, J. Hanuš, P. Solař, M. Vaidulych, **D. Nikitin**, P. Pleskunov, Z. Krtouš, T. Strunskus, F. Faupel, S.V. Roth, H. Biederman, A. Choukourov, “Magnetron-sputtered copper nanoparticles: lost in gas aggregation and found by in situ X-ray scattering,” *Nanoscale*, vol. 10, no. 38, pp. 18275–18281, 2018.
11. A. Shelemin, **D. Nikitin**, P. Pleskunov, M. Vaidulych, R. Tafiichuk, A. Choukourov, P. Kúš, P. Solař, A. Kuzminova, O. Kylián, H. Biederman, “Wetting on a-C:H coatings decorated with sub-micron structures,” *Surf. Coatings Technol.*, vol. 367, pp. 165–172, 2019.
12. **D. Nikitin**, S. Madkour, P. Pleskunov, R. Tafiichuk, A. Shelemin, J. Hanuš, I. Gordeev, E. Sysolyatina, A. Lavrikova, S. Ermolaeva, V. Titov, A. Schönhals. A. Choukourov, “Cu nanoparticles constrain segmental dynamics of cross-linked polyethers: a trade-off between non-fouling and antibacterial properties,” *Soft Matter*, vol. 15, no. 13, 2884–2896, 2019.
13. I. Velichko, I. Gordeev, A. Shelemin, **D. Nikitin**, J. Brinar, P. Pleskunov, A. Choukourov, K. Pazderů, J. Pulkrábek, “Plasma Jet and Dielectric Barrier Discharge Treatment of Wheat Seeds,” *Plasma Chemistry and Plasma Processing*, vol. 39, no. 4, pp. 913–928, 2019.
14. A. Choukourov, P. Pleskunov, **D. Nikitin**, R. Tafiichuk, A. Shelemin, J. Hanuš, J. Májek, M. Unger, A. Roy, A. Ryabov, “Plasma-assisted growth of polyethylene fractal nano-islands on polyethylene oxide films: Impact of film confinement and glassy dynamics on fractal morphologies,” *Applied Surface Science*, vol. 489, pp. 55–65, 2019.
15. **D. Nikitin**, J. Hanuš, S. Ali-Ogly, O. Polonskyi, J. Drewes, F. Faupel, H. Biederman, A. Choukourov, “The evolution of Ag nanoparticles inside a gas aggregation cluster source,” *Plasma Process. Polym.*, vol. 16, no. 10, 2019.

16. O. Kylián, A. Shelemin, P. Solař, P. Pleskunov, **D. Nikitin**, A. Kuzminova, R. Štefaníková, P. Kúš, M. Cieslar, J. Hanuš, A. Choukourov, H. Biederman, “Magnetron Sputtering of Polymeric Targets: From Thin Films to Heterogeneous Metal/Plasma Polymer Nanoparticles,” *Materials*, vol. 12, no. 15, 2019.
17. **D. Nikitin**, I. Lipatova, I. Naumova, N. Sirotkin, P. Pleskunov, I. Krakovský, I. Khalakhan, A. Choukourov, V. Titov, A. Agafonov, “Immobilization of Chitosan Onto Polypropylene Foil via Air/Solution Atmospheric Pressure Plasma Afterglow Treatment,” *Plasma Chemistry and Plasma Processing*, 2019.

List of conference contributions presented by author

1. **D. Nikitin**, M. Vaidulych, I. Gordeev, J. Hanuš, A. Choukourov, D. Slavínská, H. Biederman, “Silver Oxide and Copper Oxide Nanoparticles as Perspective Antibacterial Agents in Plasma Polymer-Based Nanocomposites,” 25th Annual Conference of Doctoral Students – WDS 2016, Prague, Czech Republic, 7.06.2016 – 9.06.2016, *oral presentation*.
2. **D. Nikitin**, A. Choukourov, V. Titov, L. Kuzmicheva, I. Lipatova, E. Mezina, V. Aleksandriiskii, A. Shelemin, I. Khalahan, D. Slavínská, H. Biederman, “Plasma-solution System as a Novel Method for Chitosan Immobilization on Polymers,” 27th Symposium on Plasma Physics and Technology, Prague, Czech Republic, 20.06.2016 – 23.06.2016, *oral presentation*.
3. **D. Nikitin**, I. Melnichuk, T. Steinhartová, M. Vaidulych, A. Shukurov, D. Slavinska, H. Biederman, “Ag nanoparticle-based nanocomposites with non-fouling and antibacterial properties,” 15th International Conference on Plasma Surface Engineering, Garmisch-Partenkirchen, Germany, 12.09.2016 – 16.09.2016, *poster*.
4. **D. Nikitin**, P. Pleskunov, A. Choukourov, V. Titov, L. Kuzmicheva, I. Lipatova, E. Mezina, H. Biederman, “Atmospheric pressure discharges for solution-based immobilization of chitosan on polymeric foils,” International Conference on Plasmas with Liquids (ICPL 2017), Prague, Czech Republic, 5.03.2017 – 9.03.2017, *poster*.
5. V.A. Titov, L.A. Kuzmicheva, A.N. Ganin, **D. Nikitin**, A. Choukourov, “Formation rate and energy yield of hydroxyl radicals in water at the action of

- discharge in gas-vapour bubbles,” International Conference on Plasmas with Liquids (ICPL 2017), Prague, Czech Republic, 5.03.2017 – 9.03.2017, *poster*.
6. **D. Nikitin**, A. Choukourov, P. Pleskunov, V. Titov, E. Sysolyatina, S. Ermolayeva, J. Hanus, A. Shelemin, D. Slavínská, H. Biederman, “Copper nanoparticle-based composites for the production of antibacterial and non-fouling surfaces,” 21th International Colloquium on Plasma processes, Nice, France, 26.06.2017 – 30.06.2017,
 7. **D. Nikitin**, A. Choukourov, S. Madkour, P. Pleskunov, A. Schönhals, H. Biederman, “Specific Heat Spectroscopy for Characterization of Copper NPs – PEO Nanocomposite Films,” 8th International Workshop on Polymer Metal Nanocomposites, Prague, Czech Republic, 12.09.2017 – 15.09.2017, *poster*.
 8. **D. Nikitin**, A. Choukourov, M. Vaidulych, P. Pleskunov, A. Shelemin, I. Khalakhan, D. Slavinska, H. Biederman, “Formation of hydrocarbon-based nanoparticles by a gas aggregation cluster source,” Baltic polymer symposium 2017, Tallinn, Estonia, 20.09.2017 – 22.09.2017, *poster*.
 9. A. Shelemin, **D. Nikitin**, J. Kousal, M. Vaidulych, P. Pleskunov, A. Choukourov, D. Slavínská, H. Biederman, “Cycling Instabilities in a Gas Aggregation Cluster Source used for Plasma Polymer Nanoparticle Formation,” NANOCON 2017, Brno, Czech Republic, 18.10.2017 – 20.10.2017, *oral presentation*.
 10. **D. Nikitin**, S. Madkour, P. Pleskunov, R. Tafiichuk, A. Schönhals, A. Choukourov, “Cu Nanoparticles Tune Segmental Dynamics in PEO Plasma Polymers,” Czech – German Workshop on Nanomaterials, České-Budějovice, Czech Republic, 10.05.2018 – 11.05.2018, *oral presentation*.
 11. **D. Nikitin**, P. Pleskunov, R. Tafiichuk, A. Shelemin, J. Hanus, E. Sysolyatina, S. Ermolayeva, V. Titov, A. Choukourov, “Hybrid Cu/Poly(ethylene oxide) Plasma Polymer Coatings for Biomedical Applications,” 7th International Symposium on Theoretical and Applied Plasma Chemistry, Ivanovo, Russia, 10.09.2018 – 15.09.2018, *oral presentation*.
 12. **D. Nikitin**, P. Pleskunov, A. Shelemin, M. Cieslar, R. Tafiichuk, V. Titov, A. Choukourov, “Synthesis of Copper Oxide Nanoparticles by Reactive Magnetron Sputtering,” 16th International Conference on Plasma Surface Engineering, Garmisch-Partenkirchen, Germany, 17.09.2019 – 21.09.2019, *poster*.
 13. **D. Nikitin**, O. Polonskyi, J. Drewes, J. Hanus, F. Faupel, A. Choukourov, H. Biederman, “In-situ monitoring of nanoparticle formation in cluster source by

UV-Vis spectroscopy,” 24th International Symposium on Plasma Chemistry, Naples, Italy, 9.06.2019 – 14.06.2019, *poster*.

AUTHOR'S CONTRIBUTION

The author carried out the construction and the modification of the experimental set-up for the deposition of NPs and composite films. The author performed the in situ UV-Vis measurements and depositions inside the GAS and took part in the SAXS measurements at DESY synchrotron, Hamburg. The author performed the deposition of plasma polymer and composite films and their characterization by ellipsometry, UV-Vis, XPS, FTIR and AFM. The author performed the wettability characterization of nanostructured coatings by WCA measurements. Moreover, the author carried out the protein adsorption tests. The author would like to thank Dr. Olexandr Polonskiy and Dr. Ivan Khalakhan for SEM measurements; Doc. Miroslav Cieslar for TEM measurement; Prof. Andreas Schonhals and Dr. Sherif Madkour for AC-chip calorimetry measurements; Prof. Svetlana Ermolaeva, Dr. Elena Sysolyatina and Alexandra Lavrikova for the antibacterial tests.

